Design, Fabrication and Characterization of Optical Biosensors based on (Bloch) Long Range Surface Plasmon Waveguides

by

Maryam Khodami

A thesis submitted to the Faculty of Graduate and Postdoctoral Studies

in partial fulfillment of the requirements for the degree of

Doctor of Philosophy
in
Electrical and Computer Engineering

Ottawa-Carleton Institute for Electrical and Computer Engineering

Department of Electrical Engineering and Computer Science
Faculty of Engineering
University of Ottawa

Abstract

In this thesis by articles, I propose and demonstrate the full design, fabrication and characterization of optical biosensors based on (Bloch) Long Range Surface Plasmon Polaritons (LRSPPs). Gold waveguides embedded in CYTOP with an etched microfluidic channel supporting LRSPPs and gold waveguides on a one-dimensional photonic crystal (1DPC) supporting Bloch LRSPPs are exploited for biosensing applications.

Straight gold waveguides embedded in CYTOP supporting LRSPPs as a biosensor, are initially used to measure the kinetics constants of protein-protein interactions. The kinetics constants are extracted from binding curves using the integrated rate equation. Linear and non-linear least squares analysis are employed to obtain the kinetics constants and the results are compared. The device is also used to demonstrate enhanced assay formats (sandwich and inhibition assays) and protein concentrations as low as 10 pg/ml in solution are detected with a signal-to-noise ratio of 20 using this new optical biosensor technology.

CYTOP which has a refractive index close to water is the fluoropolymer of choice in current state of the art waveguide biosensors. CYTOP has a low glass transition temperature which introduces limitations in fabrication processes. A truncated 1D photonic crystal can replace a low-index polymer cladding such as CYTOP, to support Bloch LRSPPs within the bandgap of the 1DPC over a limited ranges of wavenumber and wavelength.

Motivated by quality issues with end facets, we seek to use grating couplers in a broadside coupling scheme where a laser beam emerging from an optical fiber excites Bloch LRSPPs on a Au stripe on a truncated 1D photonic crystal. Adiabatic and non-adiabatic flared stripes accommodating wide gratings size-matched to an incident Gaussian beam are designed and compared to maximise the coupling efficiency to LRSPPs. The gratings are optimized, initially, through 2D modelling using the vectorial finite element method (FEM). Different 3D grating designs were then investigated via 3D modelling using the vectorial finite difference time domain (FDTD) method.

Given their compatibility with planar technologies, gratings and waveguides can be integrated into arrays of biosensors enabling multi-channel biosensing. A multi-channel platform can provide, *e.g.*, additional measurements to improve the reliability in a disease detection problem. Thus, a novel optical biosensor based on Bloch LRSPPs on waveguide arrays integrated with electrochemical biosensors is presented. The structures were fabricated on truncated 1D photonic crystals comprised of 15 period stack of alternating layers of SiO_2/Ta_2O_5. The optical biosensors consist of Au stripes supporting Bloch LRSPPs and integrate grating couplers as input/output means.

The Au stripes also operate as a working electrode in conjunction with a neighboring Pt counter electrode to form an electrochemical sensor. The structures were fabricated using bilayer lift-off photolithography and the gratings were fabricated using overlaid e-beam lithography. The planar waveguides are integrated into arrays capable of multichannel biosensing. The wafer is covered with CYTOP as the upper cladding with etched microfluidic channels, and wafer-bonded to a borofloat silica wafer to seal the fluidic channels and enable side fluidic interfaces. The proposed device is capable in principle of simultaneous optical and electrochemical sensing and could be used to address disease detection problems using a multimodal strategy.

Acknowledgments

First and foremost, I would like to express my deepest gratitude and appreciation to my thesis supervisor, Professor Pierre Berini for his support and encouragement during my PhD studies. This work would have not been possible without his guidance and help. I am grateful to him for giving me the opportunity to contribute to an exciting interdisciplinary project combining engineering, optics and photonics, biochemistry and nanofabrication. I am also grateful to him for countless hours of scientific discussion and for providing financial support which made this work possible.

I would like to acknowledge all the members and staff of the Center for Research in Photonics, at the University of Ottawa for their constant help and support during my Ph.D. studies. I would also like to thank all the members of Berini's Lab for their constant scientific help and support.

I would like to acknowledge Mr. Nagui Mikhail and Professor Niall Tait of Carleton University, Department of Electronics, who provided access to Lumerical FDTD which made the design and modeling work, presented in this thesis, possible. I would also like to acknowledge the Center for advanced computing at Queen's University and the Canadian Microelectronics Corporation (CMC) who provided help and support with computational servers and COMSOL licences.

I would like to thank my comprehensive exam, thesis proposal and thesis defence committee members, Professors Henry Schriemer, Robert Gauthier, Ksenia Dolgaleva, Hanan Anis and my external examiner Professor Mo Mojahedi, for their time and constructive feedback.

Last, but not least, I offer my deepest gratitude to my family, for their constant love, support and patience. I dedicate this work to my parents and Mehdi.

Maryam Khodami,

Ottawa, January 2020

List of publications

Papers accepted and published in refereed journals (included in the thesis):

M. Khodami, H. Northfield, E. Lisicka-Skrzek, R. N. Tait, P. Berini, "Reactive ion etching of Cytop and investigation of residual microstructure", IEEE Journal of Microelectromechanical Systems, 29, 228-235 (2020).
M. Khodami, P.Berini, "Grating couplers for (Bloch) long range surface plasmons on metal stripe waveguides", Journal of the Optical Society of America B, 36, 1921-1930 (2019).
M. Khodami, P. Berini, "Low detection limits using Sandwich and inhibition assays on long range surface plasmon waveguide biosensors", Sensors and Actuators B, 273, 1156-1161 (2018).
M. Khodami, P. Berini, "Biomolecular kinetics analysis using long-range surface plasmon waveguides", Sensors and Actuators B, 243, 114-120 (2017).

Manuscript in preparation (included in the thesis):

M. Khodami, Z. Hirbodvash, O. Krupin, W. R. Wong, E. Lisicka-Skrzek, H. Northfield, C. Hahn, P. Berini "Bloch long range surface plasmons on Au waveguide integrated with Pt counter electrodes as multimodal biosensors" to be submitted.

Collaborative Papers accepted and published in refereed journals (not included in thesis):

Z. Hirbodvash, **M. Khodami**, N. R. Fong, E. Lisicka-Skrzek, A. Olivieri, H. Northfield, R. N. Tait, P. Berini "Grating couplers fabricated by e-beam lithography for long range surface plasmon waveguides embedded in a fluoropolymer" Applied Optics, 58, 2994-3002 (2019).
S. Hassan, **M. Khodami**, R. N. Tait, R. N., P. Berini, "Fabrication of Long-Range Surface Plasmon-Polariton Bragg Gratings with Microfluidic Channels in Cytop Claddings," Microelectronics Engineering, 135, 38-44 (2015).

Papers accepted and published in refereed conferences (based on thesis work):

M. Khodami, Z. Hirbodvash, O. Krupin, P. Berini, “Bloch long range surface plasmons on waveguide arrays as multichannel biosensors”, Plasmonics in Biology and Medicine XVII 11257 (2020).

M. Khodami, Z. Hirbodvash, O. Krupin, E. Lisicka-Skrzek, H. Northfield, A. Olivieri, P. Berini, “Fabrication of Bloch long range surface plasmons biosensors”, Integrated Optics: Devices, Materials, and Technologies XXIV 11283 (2020).

M. Khodami, P. Berini, “Determination of Biomolecular Interaction Kinetics Using Surface Plasmon Waveguides”, Photonics North, IEEE (2017).

M. Khodami, P. Berini, " Characterization of long-range surface plasmon Bragg gratings with microfluidic channels", Photonics North, IEEE (2015).

Acronyms

16-MHA	16-Mercaptohexadecanoic acid
ATR	Attenuated total reflection
AFM	Atomic force microscopy
BSA	Bovine serum albumin
DDI	Distilled/Deionized
DFB	Distributed feedback
EDC	1 - ethyl - 3 - (3 - dimethylaminopropyl) carbodiimide hydrochloride
ELISA	Enzyme-linked immunosorbent assay
FDTD	Finite difference time domain
FEM	Finite element method
Gly	Glycerol
HMDS	Hexa-methyl-disilazane
IgG	Immunoglobin G
IL	Insertion loss
IPA	isopropanol Alcohol
IR	Infrared
LRSPP	Long range surface plasmon polariton
MPA	Mode power attenuation
MZI	Mach-Zender interferometers
MIBK	Methyl isobutyl ketone
NHS	N-Hydroxysuccinimide sodium salt

PC	Photonics crystal
PMMA	Poly (methyl methacrylate)
PM	Polarization maintaining
QCR	Quartz crystal microbalance
RIE	Reactive ion etching
SPP	Surface plasmon polariton
SPR	Surface plasmon resonance
SEM	Scanning electron microscopy
SAM	Self-assembled monolayer
SMF	Single mode fiber
sccm	Standard cubic centimeters per minute
TE	Transverse electric
TM	Transverse magnetic
TMAH	Tetramethylammonium hydroxide

List of Symbols

γ	Damping coefficient
ω	Angular frequency
ω_0	Angular frequency
ω_p	Plasma frequency
c	Light velocity in vacuum
E	Electric field vector
H	Magnetic field vector
k	Wave vector
n	Refractive index
t	Time
ε_0	Vacuum permittivity
ε	Relative permittivity
ε_∞	Polarization correction factor
μ_0	Vacuum permeability
λ	Wavelength
μ	Relative permeability
β	Propagation constant

Table of Contents

List of Figures

List of Tables

Chapter 1

Introduction

1.1 Biosensors and biosensing

Immunoassay-based detection methods currently used in routine laboratory tests were first introduced in 1950s. Since then the methods have been developed and became more popular by introducing chemically-linked enzymes to antibodies [1]. An immunoassay is an analytical method performed in solution in order to detect the presence of a biomolecule. Immunoassays are based on variety of labelling methods such as enzymes (enzyme linked immunosorbent assay or ELISA) [1], radioactive isotopes (radio-immunoassays) [2] and fluorescence [3] to name a few. Label-based immunoassays require sample processing and thus are expensive and time-consuming. Also, the label can block a binding site or cause background binding which leads to false positives and false negatives respectively [4]. On the other hand, there are other types of assays that do not require labeling and thus are called label-free immunoassays. Surface plasmon resonance (SPR) biosensing is an example of a label-free technique that could be used in the detection of biological species.

A biosensor is an integrated analytical device that can be used in the detection and quantification of biochemical or biological elements. Biosensors are comprised of a biochemical recognition element, such as a tissue sample, enzymes, whole cells or antibodies, a signal transduction mechanism, and fluidic channels. Based on the type of physical transducer, biosensor

technologies can be classified into a few main categories, namely: piezoelectric (quartz crystal micro balance) [5, 6], electrochemical (potentiometric and amperometric) [7, 8], and optical sensors such as surface plasmon resonance and fluorescence [9-12]. Biosensors could also be classified as catalytic biosensors or affinity biosensors. The latter make use of the analyte-ligand binding interactions (antibody-antigen, for example) which is the focus of this study.

Electrochemical Biosensors are the most common type of biosensors. In this type of biosensor the electrochemical cell consists of a reference electrode (which provides a stable voltage against which other potentials are measured), a working electrode (on which the electrochemical reaction occurs) and a counter electrode (which provides a path for the flow of electric current). A voltage or a current is produced as a result of an oxidation-reduction (redox) reaction taking place on the working electrode. Redox enzymes are required to catalyze the electron transfer by reduction or oxidation of the substrate. [13].

Piezoelectric quartz crystal based sensors, known as Quartz Crystal Microbalance (QCM), is another type of biosensor. They measure changes in the surface mass concentration by measuring changes in the resonant frequency of a quartz crystal. Initially, the QCM was used in vacuum and gas [14], but recently it has been shown that the method can be used in liquid environments as well [15].

Optical biosensors can provide rapid, direct, real-time detection and characterization of biomolecular interactions. Optical detection is generally based on the measurement of fluorescence, absorbance or refractive index changes [16]. In fluorescence, the target molecule is labeled with a fluorescent dye. The concentration of target molecule can be determined by detecting the fluorescence emission. The measurement of refractive index changes is based on the difference in the refractive indices of water ($n \sim 1.3$) and biological molecules ($n \sim 1.5$). SPR is

the most common method to determine the absorbance/refractive index changes in an aqueous medium. SPR biosensors employ excitation of surface plasmon polaritons (SPPs) as described in the following subsection. The change in the refractive index of the solution is referred to as bulk sensing while the changes due to the formation of an adlayer are referred to as surface sensing. Optical biosensors do not require any enzymatic reactions; hence they broaden the range of biochemical reactions that can be monitored using these devices.

Commercially available label-free optical biosensors make use of SPR technology (BIAcore), photonic crystals (SRU Biosystems), resonant waveguide gratings (Corning) and interferometry (Fortebio) [4]. Currently, the most common optical sensor is the SPR sensor. In this work we focus on optical biosensors using *long-range surface plasmon polaritons (LRSPPs)* as described in detail in the following chapters.

1.2 Thesis scope and outline

The aim and scope of this dissertation is to demonstrate the full design, fabrication and characterization of optical biosensors based on (Bloch) LRSPPs. Gold waveguides embedded in CYTOP with an etched microfluidic channel supporting LRSPPs and gold waveguides on a one-dimensional photonic crystal (1DPC) supporting Bloch LRSPPs are exploited for biosensing applications. A multi-channel multi-modal biosensing platform, capable of simultaneous optical and electrochemical sensing, is designed and fabricated using wafer scale processing techniques. The multi-channel multi-modal platform provides additional measurements to improve reliability in a disease detection problem. Each chapter is presented as a scientific article with an introductory section. The dissertation is organized as follows:

Chapter 2 presents a comprehensive review of the topics related to design, fabrication and characterization of optical biosensors based on surface plasmon polaritons. First, the theory of surface plasmons is described. Surface plasmon resonance biosensors are discussed in detail and the review of previous works is provided. LRSPP based waveguide devices, currently used in biosensing applications, are also discussed along with design considerations for biosensing application. A review of surface functionalization methods is provided, and the chapter is closed with a brief description and review of Nano-fabrication techniques.

Chapter 3 presents the extraction of kinetics constants for protein-protein interactions using LRSPP waveguide biosensors. The binding curves are obtained by monitoring the output power of the system continuously over time and converting the raw data to surface mass concentration. The affinity and kinetics constants obtained are within the range expected for this interaction.

Chapter 4 presents enhanced assay formats using LRSPP waveguide biosensors capable of very low detection limits. Specifically, sandwich and inhibition (competitive) assays were developed and demonstrated using Bovine Serum Albumin (BSA) and anti-BSA produced in rabbit as a model bio-specific pair. Titration curves were extracted for both immunoassays. We demonstrate that protein concentrations in solution of 10 pg/ml can be detected with a signal-to-noise ratio of 20 using this new optical biosensor technology.

Chapter 5 presents the optimization of grating couplers for (Bloch) LRSPPs on metal stripe waveguides for biosensing applications. LRSPP waveguide biosensors used to demonstrate binding kinetics and enhanced assay formats in previous chapters are fabricated on CYTOP as the lower cladding material. Although CYTOP has a refractive index close to water, its use introduces limitations in fabrication processes due to its low glass transition temperature. A truncated 1D photonic crystal (1DPC) is designed to replace CYTOP cladding to support Bloch LRSPPs within

the bandgap of the 1DPC over limited ranges of wavenumber and wavelength. 2D cross sectional model of the structure, incorporating the Au waveguide and grating couplers on a 1DPC or CYTOP, was employed to optimize the structural parameters of the grating couplers via finite element method (FEM) electromagnetic modelling. Wide gratings on adiabatic and non-adiabatic flared stripes are then investigated using a full 3D model of the structure via finite-difference time-domain (FDTD) electromagnetic simulations. Input coupling efficiencies of up to 25% at λ_0 = 1310 nm are predicted for an optimal grating design. The structures realized include straight waveguides with narrow gratings and with wide gratings on (non-) adiabatic flared stripes, fabricated using photolithography and electron beam lithography. The wavelength response of the fabricated structures was acquired to verify the design concepts.

Chapter 6 presents fabrication details of the structure proposed and modeled in Chapter 4. This novel optical biosensor operates with Bloch LRSPPS on waveguide arrays integrated with electrochemical biosensors and thus is capable of simultaneous optical and electrochemical sensing (multimodal biosensing). The structures are fabricated on a truncated 1D photonic crystal composed of alternating layers of SiO_2 and Ta_2O_5. Au waveguides, Pt stripes and contact pads are fabricated using a bilayer lift-off photolithography process. Grating couplers as input-output means are fabricated using overlaid electron-beam lithography. The wafer is covered with Cytop as the upper cladding and etched to form the microfluidic channels. Channel etching was performed using both photoresist and metal masks and grass like structure was observed post Cytop etching which is discussed in the subsequent chapter. The wafer is covered with borofloat silica using a wafer bonding process. The planar waveguides are integrated into arrays capable of multichannel biosensing. The optical and electrochemical characterization of the biosensor chip

including bulk and surface sensing and cyclic voltammetery measurements are presented as a proof of concept.

Chapter 7 presents reactive ion etching of Cytop as the host material for microfluidic channels. Different grades of Cytop on different substrates along with different mask materials and using different RIE parameters are investigated, initially to address the formation of "grass" post Cytop etching that was consistently observed during the biosensor fabrication process. A comprehensive acid clean procedure was proposed to remove the grass post Cytop etching.

Chapter 8 presents the concluding remarks and suggestions for future work.

1.3 Copyright permissions

1.3.1 Chapter 3

M. Khodami, P. Berini "Bimolecular kinetics analysis using long range surface plasmon waveguide" *Sensors and Actuators B: Chemical* 243, 2017.

1.3.2 Chapter 4

M. Khodami, P. Berini "Low detection limits using sandwich and inhibition assays on long range surface plasmon waveguide biosensors" *Sensors and Actuators B: Chemical* 273, 2018.

1.3.3 Chapter 5

The article in this chapter is presented in full and is reprinted with the permission of Optical Society of America.

M. Khodami, P. Berini "Grating couplers for (Bloch) long range surface plasmons on metal stripe waveguides" *Journal of Optical Society of America B*, 36 (7), 2019.

1.3.4 Chapter 6

This article is to be submitted for publication.

1.3.5 Chapter 7

The article in this chapter is presented in full and is reprinted with the permission of IEEE.

© [2020] IEEE. Reprinted, with permission from M. Khodami, H. Northfield, E. Lisicka-Skrzek, R. N. Tiat, P.Berini, "Reactive ion etching of Cytop and investigation of residual microstructure", *IEEE Journal of Microelectromechanical Systems*, Volume 29, Issue 2, April 2020.

In reference to IEEE copyrighted material, which is used with permission in this thesis, the IEEE does not endorse any of University of Ottawa's products or services. Internal or personal use of this material is permitted.

Chapter 2

Background and literature review

2.1 Surface Plasmon Polaritons (SPPs)

Surface Plasmons (SPs) are quanta of surface charge density oscillations. The coupling of lattice excitations to quanta of electromagnetic waves (or photons) is referred to as "polaritons". By definition, Surface Plasmon Polaritons (SPPs) are transverse magnetic optical surface waves, propagating along a metal dielectric interface. The relative permittivity of the lossless dielectric medium is described using a real number, while the metal region is characterized by a frequency dependent dielectric function $\varepsilon_r(\omega)$, which could be described using Drude-Sommerfeld model [17]:

$$\varepsilon_r(\omega) = 1 - \frac{\omega_p^2}{\omega^2 + i\gamma\omega} \quad \textbf{(1)}$$

where ω_p is the plasma frequency and γ is the damping coefficient, often expressed as $\gamma=1/\tau$ in where τ is the relaxation time of electrons in the metal [18]. Considering the time harmonic form of Maxwell's equation ($e^{-j\omega t}$) and the mode filed variation along +z direction ($e^{-\alpha z}$), the real and imaginary part of this expression can be written:

$$\varepsilon_r(\omega) = 1 - \frac{\omega_p^2}{\omega^2 + \gamma^2} + i\,\frac{\gamma\omega_p^2}{\omega(\omega^2 + \gamma^2)} \quad \textbf{(2)}$$

Using $\omega_p = 13.8 \times 10^{15}/s$ and $\gamma = 1.075 \times 10^{14}/s$ for gold [17], the real and imaginary parts of this function are plotted in Fig. 1. As is evident from Fig. 1, a negative value for the real part of the dielectric constant is obtained, implying that an SPP mode can be supported at metal-dielectric interfaces. This is the case for many metals at optical frequencies.

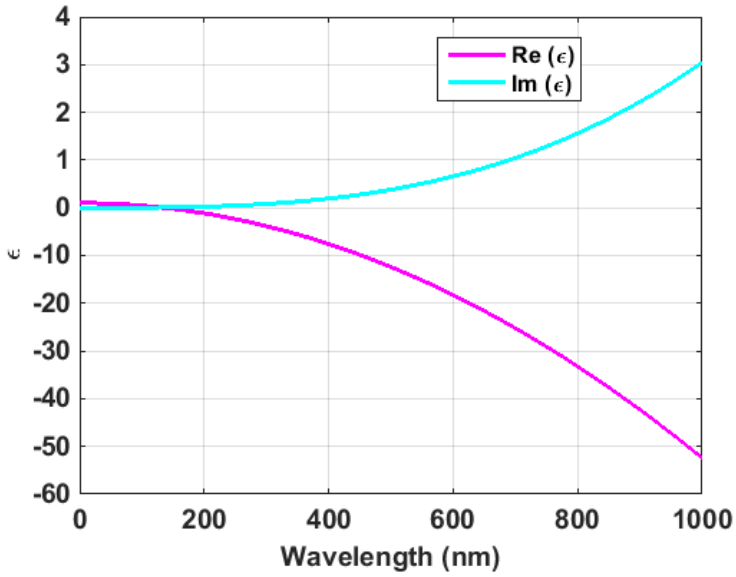

Fig. 1: Real and imaginary part of the dielectric constant for gold according to Drude-Sommerfeld model (reproduced from [17]).

While the Drude-Sommerfeld model provides accurate results in the infra-red region of the spectrum, it needs to be modified for the visible and near ultraviolet region, due to the presence of bound electrons in the metal. In this case Drude-Lorentz model is a more accurate description of the dielectric function, expressed as follows:

$$\varepsilon_r(\omega) = \varepsilon_\infty - \frac{\omega_p^2}{\omega^2 + i\gamma\omega} + \varepsilon_{int}(\omega) \quad \textbf{(3)}$$

where ε_∞ is the material polarization correction factor and $\varepsilon_{int}(\omega)$ is the inter-band transition correction factor, described as:

$$\varepsilon_{\text{int}}(\omega) = 1 - \frac{\widetilde{\omega_p}^2}{({\omega_0}^2 - \omega^2) - i\gamma\omega}$$

(4)

where $\widetilde{\omega}_p$ is analogous to ω_p in the Drude-Sommerfeld model. This expression could be re-written to obtain the real and imaginary parts of the dielectric function:

$$\varepsilon_{\text{int}}(\omega) = 1 - \frac{\widetilde{\omega_p}^2({\omega_0}^2 - \omega^2)}{({\omega_0}^2 - \omega^2)^2 + \gamma^2\omega^2} + i\frac{\gamma\,\widetilde{\omega_p}^2\omega}{({\omega_0}^2 - \omega^2)^2 + \gamma^2\omega^2}$$

(5)

Using $\widetilde{\omega_p} = 45 \times 10^{14}/s$, $\gamma = 8.35 \times 10^{14}/s$, $\omega_0 = {}^{2\pi c}/_{\lambda}$ and λ=450 nm, the real and imaginary part of the function are plotted in Fig. 2, from which a resonant behaviour is observed for the imaginary part and a dispersion-like behaviour is observed for the real part.

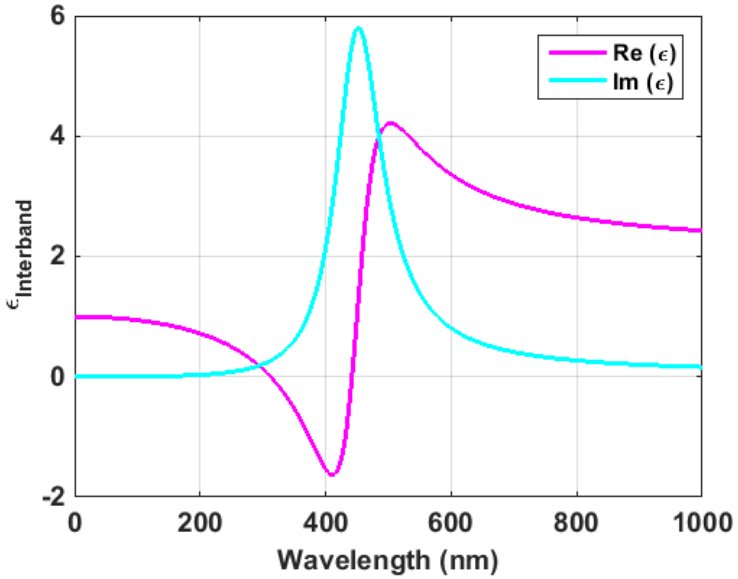

Fig. 2: Contribution of bound electrons to the dielectric function of gold (reproduced from [17]).

Due to the inaccuracy of the theoretical models (especially around the resonance), the optical constant of the noble metals have been measured since the time of Drude. The optical constants *n*

and *k* are obtained for gold from reflection and transmission measurement on vacuum evaporated thin films at room temperature [19]. Measured values of dielectric constant vs. wavelength for gold are shown in Fig. 3.

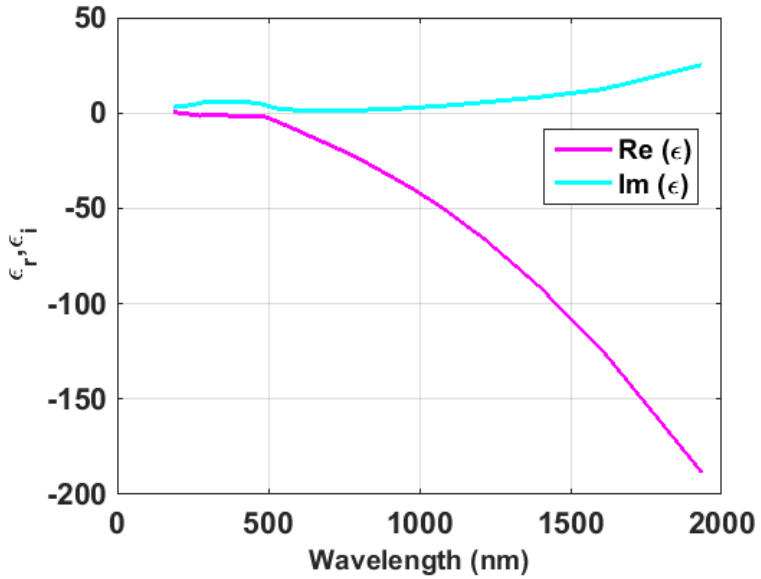

Fig. 3 Measured values of dielectric constants for gold according to Johnson and Christy [19]

SPPs only exist for the TM polarization. The propagation constant of the SPP can be described as:

$$\beta = \frac{\omega}{c}\sqrt{\frac{\varepsilon_m \varepsilon_d}{\varepsilon_m + \varepsilon_d}} \quad \textbf{(6)}$$

Where ε_m and ε_d are the relative permittivity of the metal and dielectric.

Energy and momentum conservation must be fulfilled in order to excite SPPs. The most common technique to excite SPPs is via prism coupling where the attenuated total reflection (ATR) condition is indicative of SPP excitation at metal dielectric interface. A prism-coupled system, based on the Otto or Kretschmann configurations, is commonly used to excite SPPs [20, 21, 22]. In the Otto configuration, there is a low index gap (air gap) between the prism and metal film,

whereas in the Kretschmann configuration a thin metal film is directly deposited on top of the glass prism (Fig. 4).

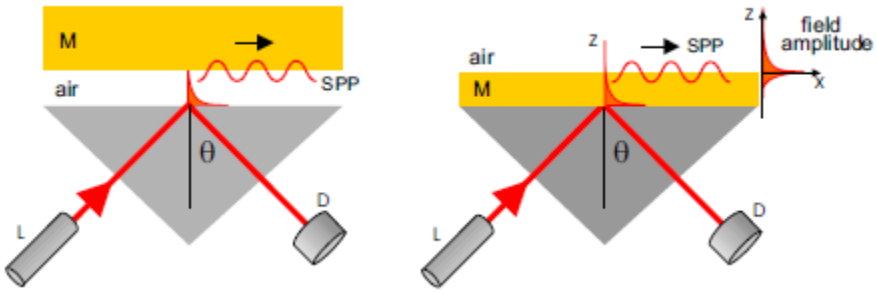

Fig. 4: Excitation of surface plasmon using Otto (left) and Kretschmann (right) configurations (adapted from [17]).

In the Kretschmann geometry, the momentum matching condition for the excitation of SPPs on the metal film is described as:

$$k_x = \left(2\pi/\lambda\right) n_p \sin\theta = Re\{\beta\} \tag{7}$$

where k_x is the wave vector of the incident light beam, n_p is the refractive index of the prism and β is the propagation constant of the SPP.

In conventional SPR biosensors (based on the Kretschmann configuration) an immobilized bio-recognition element (such as an antibody) is coated on the metal surface and p-polarized laser light is incident at the prism base from which the reflection of the beam is monitored, as shown in Fig. 5. At a certain angle, the incident light is coupled to SPPs. As a result, the intensity of the reflected beam is decreased. A change in the refractive index of the dielectric medium on the other side of the metal film, or the formation of an adlayer thereon, will result in significant changes in

the SPP coupling angle (Eq. (7), as β is altered). A plot of the intensity *vs*. incident angle produces the sensorgram. The association and disassociation parts of such a curve are used for the extraction of binding kinetics as will be discussed in the following chapters.

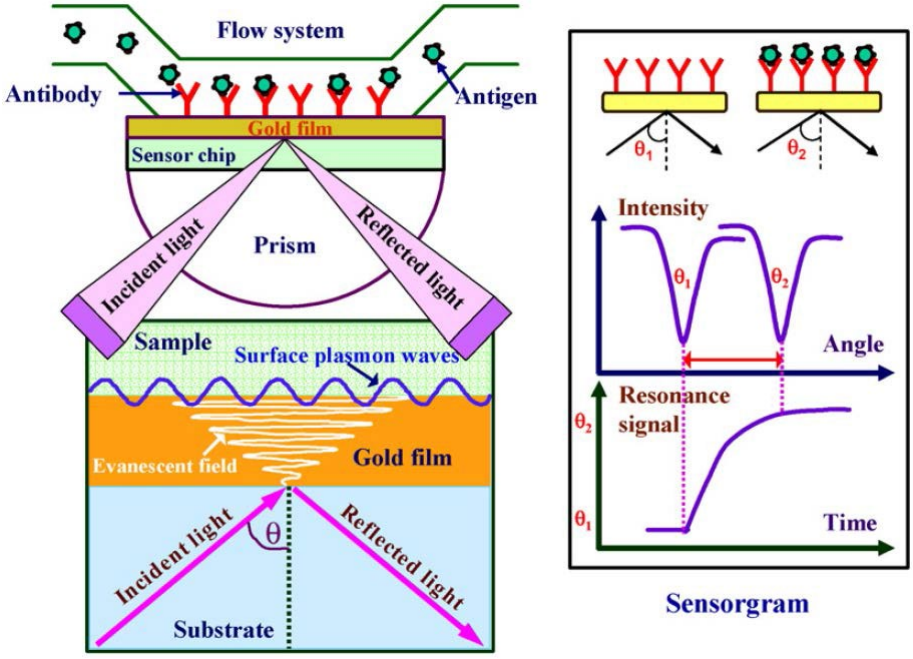

Fig. 5: Kretschmann configuration of ATR (left) and sensorgram (right) demonstrating the change of intensity of the output light as a function of SPR angle (adopted from [16]).

Good confinement and high surface and bulk sensitivities as well as high attenuation are the most dominant properties of single interface SPPs. The high attenuation can be addressed using double-interface SPPs that can propagate over an appreciable length, the so-called long range surface plasmon polariton, as will be discussed in the following subsection.

As described above, SPR biosensors employ excitation of SPPs. A brief review of the previous biosensing works based on commercial SPR systems is provided in the introduction section of the manuscript presented in Chapter 4 of this thesis work, which follows here for

completeness. “Using SPR technology, the direct detection of Bovine Serum Albumin (BSA) has been studied and a detection limit of 100 pM was reported [23]. In this study a protein A film was formed on a self-assembled monolayer to realize the immuno-sensor. The detection of staphylococcal enterotoxin B (SEB) in milk to a detection limit of 5 ng/ml in a direct assay format, and to 0.5 ng/ml in a sandwich assay format in buffer and milk was reported in [24]. Cardiac troponin was detected using a sandwich assay to a detection limit of 25 µg/ml [25]. Domoic acid was detected using an inhibition (competitive) assay to a detection limit of 0.1 ng/ml [26]. Benzo[*a*]pyrene (BaP) detection has been reported in [27] and a detection limit of 50 pg/ml was achieved using an inhibition assay. The detection of pituitary hormones using an inhibition assay was reported in [28], where detection limits of 6 ng/ml for human growth hormone (hGh) in serum, and of 1 ng/ml for human follicle stimulating hormone (hFSH) and human luteinizing hormone (hLH) in urine were reported. The detection of BSA in milk using various immunoassay formats including sandwich and inhibition assay was reported in [29], where a detection limit of 1 ng/ml was achieved using an inhibition assay. Multi-analyte detection of environmentally relevant pesticides was performed by using a two-channel SPR biosensor. Using inhibition immunoassay format a detection limit of 18 ng/ml for DDT, 50 ng/ml for chlorpyrifos and 52 ng/ml for carbaryl is reported [30]. Selective detection of methamphetamine was realized using inhibition assay format. The SPR sensor was capable of detecting concentrations in the range of 0.1-1000 ng/ml [31]. A chip-based digital SPR platform was used for BSA detection yielding a detection limit of 1 pg/ml [32]. So according to this (limited) subset of the literature on enhanced assays with SPR, detection limits in the broad range from 1 pg/ml to 25 µg/ml have been achieved, with a few ng/ml being typical. The detection limit depends on the target analyte, the sensing medium, the interrogation apparatus, sensor chip and the experimental conditions”.

SPR technology was also used to determine the rate and equilibrium binding constants of biomolecular interactions. Interaction kinetics of recombinant human sCD4 and immobilized antibody (MoAb L71) was described using the integrated rate equation [33]. Matrix bound monoclonal antibodies interacting with HIV-1 core protein p24 was used as a biomolecular pair to determine the association and disassociation rate constants [34], where the affinity and reaction rates of the interaction were compared with immobilized amino-theophylline reacting with monoclonal antibodies (MAbs). Kinetic analysis of biomolecular interactions and protein detection using enhanced assay formats are discussed in detail in Chapter 3 and 4 of this thesis.

ATR monitoring based on a prism coupler is an efficient and straightforward method, but the prism adds bulk and is incompatible with integration and miniaturization. Hence, surface plasmon excitation from the guided mode of an optical fiber or waveguide has attracted a lot of attention in recent years. Planar optical waveguides can be integrated with other planar structures or can be integrated into arrays of biosensors. The coupling of a waveguide mode to a surface plasmon in an aqueous environment in a waveguide coupled SPR sensor was reported in [35], where strong coupling between surface plasmon waves and the mode of the waveguide was observed at visible wavelengths. A fiber-optic chemical sensor based on surface plasmon resonance was presented in [36]. A section of fiber cladding was removed and a 55 nm thick silver film was deposited on the fiber core. Changes in the bulk refractive index (also known as bulk sensing) were determined by measuring the transmitted spectrum. A waveguide surface plasmon resonance device was used for the determination of simazine in water samples [37]. The sensor was incubated in antibody samples and the sensing solution was injected over the immobilized antibody. Sensing occurred on the surface of the modified gold film while the rest of the chip was isolated from the reaction. A fibre optic surface plasmon resonance device based on spectral

interrogation of SPR in a fiber optic sensing element was described in [38]. The sensor was able to measure refractive index changes as small as 5×10^{-7}. IgG and anti-IgG were used to demonstrate the ability of the sensor for biosensing applications.

SPR biosensors based on the excitation of SPPs using diffraction gratings are also reported in the literature. In this configuration, the metal film is periodically corrugated in order to satisfy the momentum matching condition for the excitation of SPP on the metal film as described by Equation. 7. A sensitivity comparison has been made between a diffraction grating and a prism coupler based SPR biosensor [39]. It was demonstrated that the sensitivity of the grating based structure using a wavelength interrogation method was much less than that of prism coupled structure, while a comparable sensitivity was observed for both systems using an angular interrogation method. A diffraction grating was used to excite surface plasmon at the gold/solution interface, and the interaction of immobilized human IgG and purified goat anti-human IgG was observed using an angular interrogation method [40]. A surface plasmon resonance gas sensor comprised of diffraction gratings was used in a wavelength integration mode where the SPR deep was observed at an off-normal angle of incidence [41].

2.2 Long Range Surface Plasmon Polaritons (LRSPP)

As described in previous section, single interface SPPs suffer from high attenuation losses which limits their application. If a thin metal film is embedded in a dielectric medium, such that the top and bottom cladding have similar (or close) refractive indices, the structure operates in the so called long range SPP mode. LRSPPs can be excited in a prism coupled system based on attenuated total reflection (ATR) [42, 43], or in an end-fire coupling scheme using a TM polarized laser beam. The schematic of Prism coupled system is shown in Fig. 6. The angle of incidence varies beyond

the critical angle and the reflected power is monitored using a photodetector. At a certain angle, the wavenumber of the incident beam equals the wavenumber of the propagating LRSPP mode. As a result, a drop in the reflected power is observed.

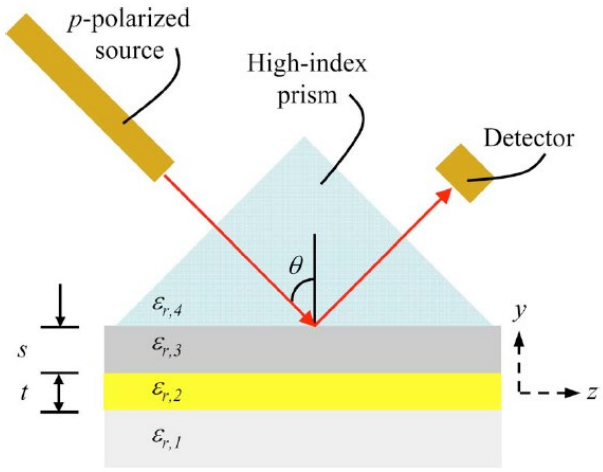

Fig. 6: Prism coupling technique for exciting SPPs (adopted from [44]).

A metal slab of infinite width bounded by two dielectric layers, as shown in Fig. 7, can support LRSPP mode. In such a structure, SPPs supported by individual metal dielectric interfaces coupled to form super-modes. The modes are confined at the metal-dielectric interfaces in the vertical and longitudinal directions. The symmetric and asymmetric bound modes of the slab waveguide (denoted as s_b and a_b) are referred to as the long range surface plasmon polariton and short range surface plasmon polariton respectively [44]. By decreasing the thickness of the metal film, the effective index and attenuation of the asymmetric mode increases, whereas those of the symmetric mode decrease. The symmetric mode exhibits a much lower attenuation than the asymmetric mode in thin films (and thus is termed the long range mode). LRSPPs have been excited in prism-coupled sensors in order to explore the sensitivity of the device, and used in the detection of *e.coli* bacteria [45] and for studying the effects of toxins on HEK-293 cells [46].

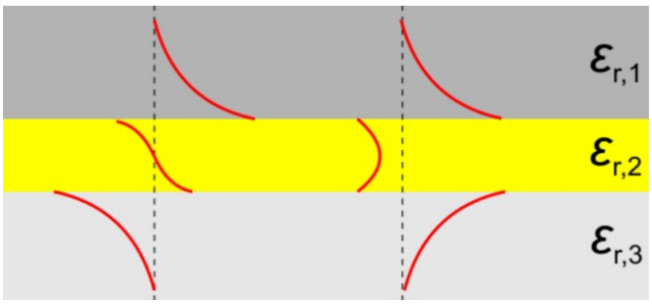

Fig. 7: A dielectric-metal-dielectric structure consists of a thin metal layer ($\varepsilon_{r,2}$) bounded by two dielectric cladding layers ($\varepsilon_{r,1}$, $\varepsilon_{r,3}$). The distributions of the E_y component of the two bound SPP modes, s_b (right) and a_b (left) are shown as red curves (adapted from [44]). A coordinate system similar to the one shown in Fig. 6 is assumed.

The mode spectrum is enriched by limiting the width of the metal slab. The fundamental $ss^0{}_b$ mode supported by a thin metal stripe evolves in a similar manner as the s_b mode of the infinite slab waveguide and is referred to as a LRSPP as well.

For a waveguide structure embedded in fluoropolymer (*i.e.* CYTOP, $\varepsilon_{r,1} = \varepsilon_{r,3}$) similar to the one shown in Fig. 7, the mode propagates in the z direction with a complex propagation constant: $\gamma = \alpha + j\beta$, where α is the attenuation constant and β is the phase constant. The mode of the structure is calculated using Lumerical (Mode), for a 5 μm wide 35 nm thick Au stripe embedded in CYTOP where $\varepsilon_{r,cytop}$ =1.3348^2 and $\varepsilon_{r,Au}$ = -86.8 +i8.322, and is shown in Fig. 8. The effective index of the mode is equal to 1.340821+i0.00021 with 8 dB/mm loss at λ_0=1310 nm.

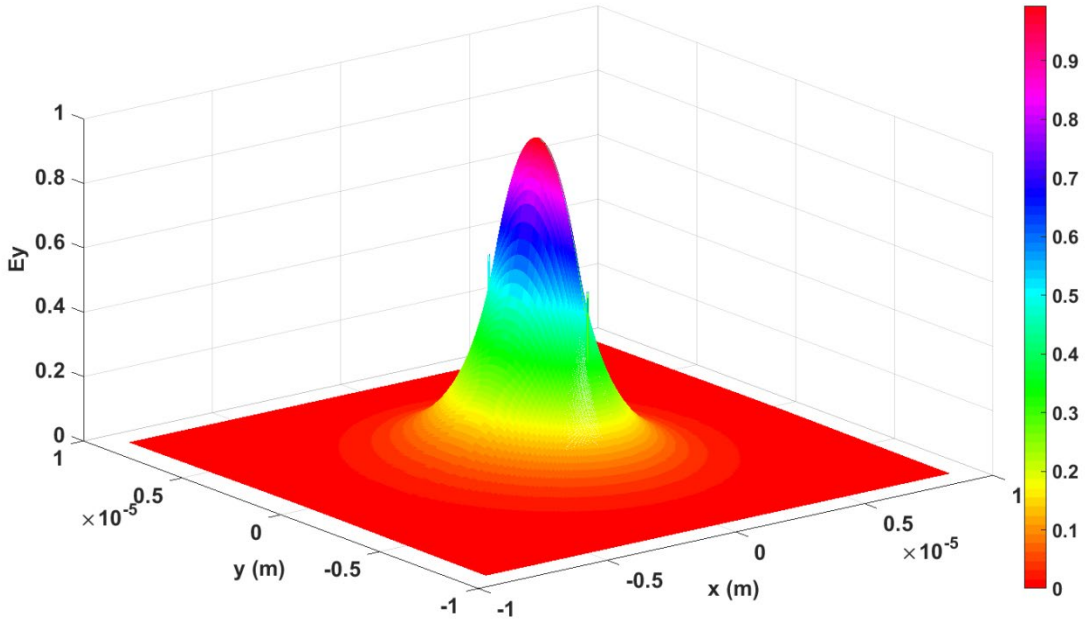

Fig. 8: Mode output of a 5 μm wide, 35 nm thick Au stripe embedded in CYTOP obtained using Eigen-mode solver

The mode power attenuation (MPA) in dB/mm is computed from attenuation constant α as:

$$MPA = 0.02\alpha \log_{10}^{e} \quad \textbf{(8)}$$

The propagation length L of the mode is the distance from the launch point where its mode power is reduced by a factor of 1/e and is given by

$$L = {}^{1}/_{2\alpha} \quad \textbf{(9)}$$

The attenuation and coupling efficiency to an incident Gaussian beam are two important specifications of LRSPP waveguides [47]. The coupling efficiency of the ssb^0 mode to single mode fiber can be estimated using:

$$C = \frac{\iint E_{y1}.E_{y2}^{*}dA}{\sqrt{\left(\iint E_{y1}.E_{y1}^{*}dA\right)\left(\iint E_{y2}.E_{y2}^{*}dA\right)}}$$

(10)

where E_{y1} corresponds to the transverse electric field component of the ssb^0 mode and E_{y2} corresponds to electric field of a single mode fiber which can be defined as a corresponding Gaussian distribution aligned to the center of LRSPP waveguide.

LRSPPs on metal stripes can be excited by butt coupling a single mode fiber to the waveguide. The optimum condition for LRSPP propagation is achieved by using a symmetric top and bottom dielectric cladding. A low index cladding that matches the refractive index of biological compatible fluids (such as phosphate buffer saline with a refractive index (RI) close to that of water n~1.330) is required to maintain the RI symmetry of the structure. In this case the choice of the cladding material is limited to fluoropolymers with a low index, such as Teflon or CYTOP. The fabrication of LRSPP straight waveguides composed of gold stripes embedded in CYTOP with a microfluidic channel etched into the top cladding is described in [48]. It consists of an optical lithography step to define Au features on a bottom cladding of CYTOP. A fluidic channel of length L = 1.65 mm was formed by etching the top CYTOP cladding down to the gold surface. LRSPP biosensors based on metal stripe waveguides offer advantages over prism-coupled sensors, in the form of increased sensitivity, compactness, and ease of manufacturing [49]. Dengue virus detection [50,51], bacteria detection in urine [52] and the detection of leukemia markers [53] has been performed using LRSPP waveguide biosensors. They have also been used for the extraction of binding kinetics [54] as well as sandwich and inhibition immunoassay demonstration [55]. Various other configurations such as Y-junctions were also used for attenuation-based

sensing [56]. Bragg gratings and single and multiple outputs Mach-Zender interferometers (MZI) were used for phased based detection [57, 58, 59].

An optical setup comprised of a DFB laser, optical fiber, collimating objective, aperture, beam splitter, infrared (IR) camera and power sensor, as shown in Fig. 9, was used to excite and capture the output of a straight waveguide biosensor. The buffer solution is injected through the fluidic channel using a syringe pump at a constant flow rate of 20 µl/min. The output power is measured using a power sensor and recorded using Labview. The sensor die along with a custom made fluidic jig is shown in Fig. 10. The custom-made fluidic jig, consisting of a metal base and a PMMA slide has been designed to hold the device under test. The fluidic tubing passes through the holes that are drilled at each end of the PMMA slide. The O-Ring (Apple Rubber Product Inc.) seals the etched channel. The metal base is machined to hold the device and integrate the fluidic PMMA slide into the optical setup [60].

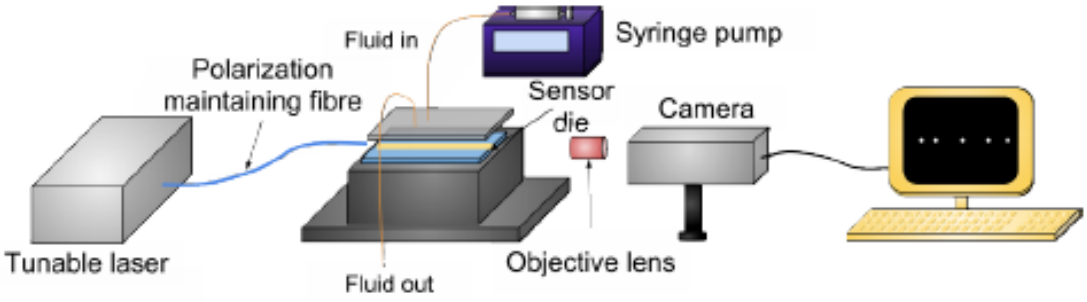

Fig. 9: Optical setup used to measure the output power throughout Chapter 3 and 4 of this thesis (adapted from [56])

Most recently, Bloch LRSPPs, supported by thin metal stripes on a 1D photonic crystal, have attracted a lot of attention for biosensing application [61, 62, 63, 64, 65]. In these structures, a truncated 1D photonic crystal (1DPC) can replace a low-index polymer cladding to support Bloch

LRSPPs within the bandgap of the 1DPC over prescribed ranges of wavenumber and wavelength [66-68]. Low index polymers such as CYTOP have a low glass transition temperature which introduces limitations in fabrication processes. This topic will be discussed in detail in Chapter 5 and 6 of this thesis.

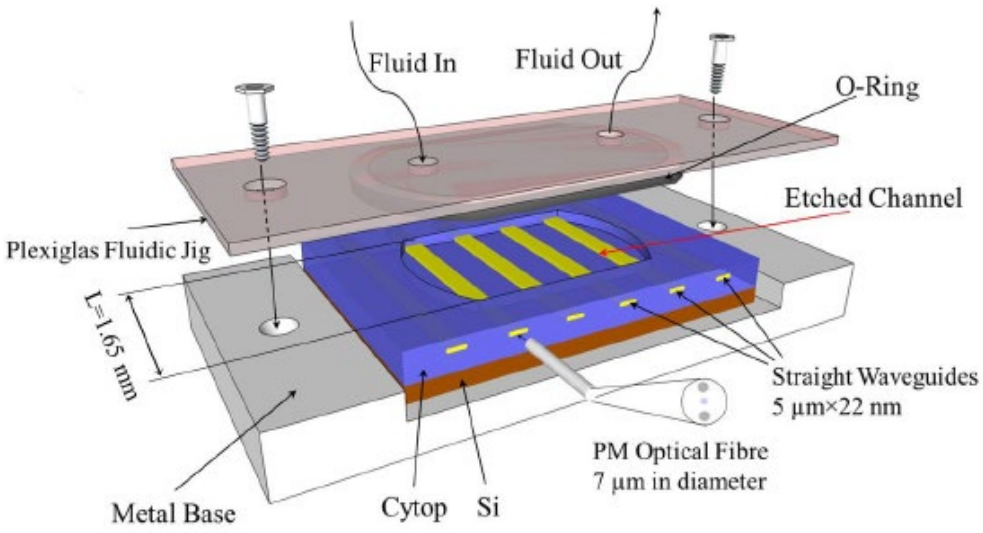

Fig. 10: Sensor die incorporating straight gold waveguides along with custom made fluidic jig with PMMA slide on top and the metal base at the bottom (adapted from [60])

2.3 Surface functionalization strategies

Different surface functionalization strategies are based on physical adsorption, covalent bonding through the formation of a thiol-based self-assembled monolayer (SAM), and affinity interactions (*e.g.*, Protein G-IgG) [69]. Physical adsorption is the simplest method and is based on intermolecular forces and is not used frequently due to limitations, including random orientation, less stability, loss of bioactivity and limited immobilization on hydrophilic surfaces [70]. The explanation of the other two methods is provided here, although we focus on self-assembled monolayers in this study.

2.3.1 Self-assembled monolayer (SAM)

A gold surface is a standard sensing surface in biosensing for several reasons: Gold is a relatively inert metal that doesn't react with most chemicals, and surface chemistry approaches based on an alkanethiol self-assembled monolayer (SAM) on Au surfaces are very well established [71-80]. SAMs of sufficient chain length form a close-packed structure oriented perpendicularly to the metal surface. A SAM can form on Au waveguides through incubation of the device into a dilute ethanolic solution of thiols for about 12-18 hours at room temperature [81]. The thiols saturate the surface quickly, but the re-organization process to obtain a tightly packed SAM takes place slowly over time. Formation of the SAM occurs through a covalent coupling of the thiol groups (R-SH) of alkanethiol, which could be described by equation 11 [78], and schematically using Fig. 6.

$$Au + HS - R \xrightarrow{yields} Au - S - R + {}^{1}/_{2}\, H_2 + e^- \qquad \textbf{(11)}$$

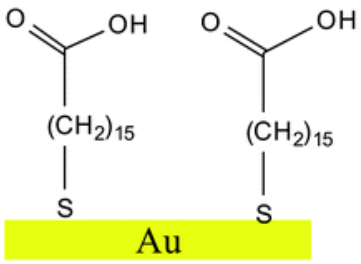

Fig. 11: Formation of a SAM on Au waveguide.

Covalent bonds are formed between the functional group of amino acids of proteins and the electrophilic group on the sensor surface. Amino (–NH2) groups, thiol (–SH) groups, and carboxyl (–COOH) groups are examples of functional groups of amino acids.

Immobilization of an amino group is commonly performed through the reaction of N-Hydroxysuccinimide sodium salt (NHS) and 1 - ethyl - 3 - (3 - dimethylaminopropyl) carbodiimide hydrochloride (EDC), in aqueous solvents as shown in Fig. 7. EDC in aqueous solution is used to transform the carboxylic group into reactive o-acylisourea intermediate. O-acylisourea then reacts with primary amines to form amide bonds. N-hydroxysuccinimide sodium salt (NHS) is usually added to the EDC solution to prevent the reverse transformation of the reactive groups to the carboxylic groups [82, 83].

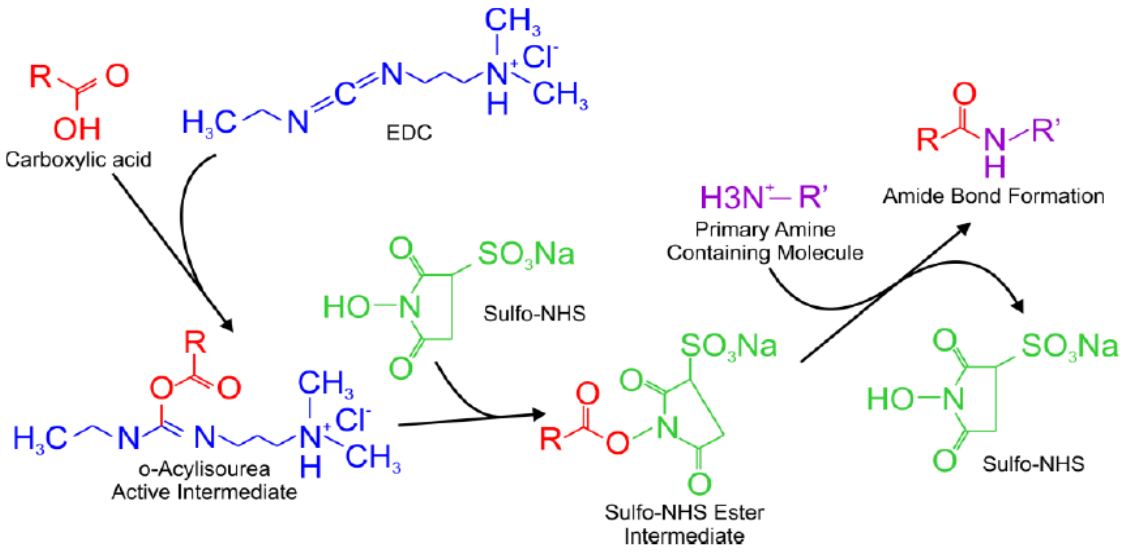

Fig. 12: Two-step process of Amin-Carboxylic acid coupling (adapted from [82]).

2.3.2 Protein G-IgG approach

Another surface functionalization approach is based on a biochemical affinity reaction. Protein G is used as the specific antibody binding protein in this approach. The Fc fragment of antibodies binds selectively to protein G immobilized on the sensor surface. The antibody binding sites located on Fab variable region (antigen binding fragment) are available for antigen binding [83]. The advantage of using Protein-G functionalization approach is that, Ig-G molecules orient

themselves in an upward manner, allowing Fabs to be fully exposed to capture analyte in solution. The disadvantage of this method is mostly associated with longer interaction time in comparison with the fast formation of covalent bonds in the SAM approach. The diagram in Fig. 8 describes different immobilization technique according to the orientation of antibodies on the sensor surface.

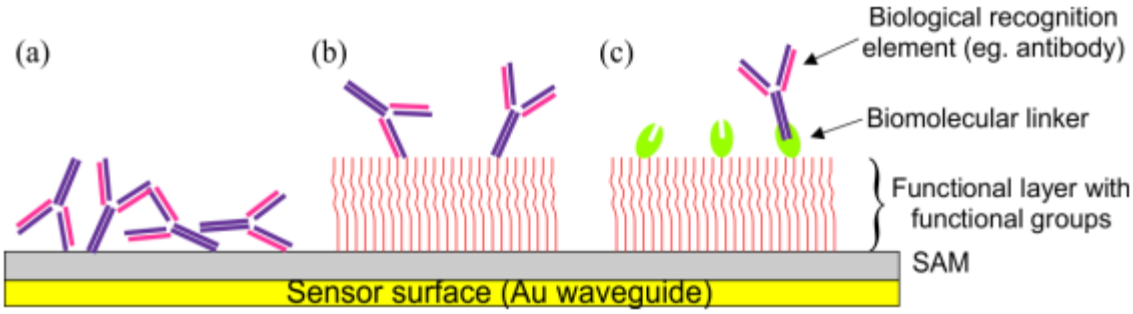

Fig. 13: From left to right: Physical adsorption, covalent coupling and Site-specific bio-affinity surface immobilization approach (adopted from [69]).

2.4 Micro/Nano fabrication techniques

Microfabrication techniques originate from the semiconductor manufacturing industry [84]. Many different Micro/Nano fabrication techniques are employed in this thesis work to realize a compact and planar waveguide that can be integrated into arrays enabling multi-channel multi-modal biosensing. Contact photolithography, electron-beam lithography, thin film metallization, wet and dry etching and wafer bonding are amongst the most important techniques that are used to fabricate our biosensor chips. Besides that, numerous polymers and metals are employed in this work to realize the device fabrication and integration. Among all, photoresists and amorphous polymers such as CYTOP played a vital role in this research work. Standard clean-room metrology methods such as scanning electron microscopy (SEM), atomic force microscopy (AFM) and profilometry

are also employed for device characterization. In this section we describe the material and the techniques used to realize this goal.

2.4.1 Spin coated polymers

Polymers play an essential role in microfabrication processes due to their flexibility and chemical selectivity. Polymers are typically applied through spin coating, where they are diluted with solvents to facilitate the coating of the surface. The viscosity of the polymer along with angular rotation speed of the spinner will determine the thickness of the film. Among all, poly methyl methacrylate (PMMA), photoresists (such as S1805 and SPR 955), lift-off resists (such as LOR 1A and LOR 10B), and CYTOP are widely used in this fabrication work.

Curing the polymer, where it is heated above Glass transition temperature (T_g), is essential in most microfabrication techniques. Solvent evaporation makes the polymer hard and suitable for post processing.

2.4.2 CYTOP

CYTOP™ is an amorphous fluoropolymer commercialized by AGC chemicals [85]. It's a highly transparent polymer with a refractive index close to water and a glass transition temperature of T_g= 108 °C, meaning that significant reflow can occur if the polymer is heated above T_g. Glass transition temperature is a temperature over which an amorphous material transitions from a hard glassy state to a soft rubbery state. CYTOP can be dissolved with a special fluorinated solvent (CT-solve) and is resistant to most acids and bases. Compared to other common fluoropolymers such as PDFE (or Teflon) [86], CYTOP has a non-crystalline structure with extremely high optical transmission. Three types of CYTOP products are available: Type A, Type M and Type S, based

on the additives incorporated therein as described in Fig. 14. CYTOP M grade provides adhesion to the surface through an amino silane coupling agent and is normally used as an adhesion promotor for other CYTOP grades. CYTOP A grade is highly transparent in visible region of the spectrum while CYTOP S grade is referred to as optical grade and is transparent from the deep UV to the near IR range. CYTOP is used as the cladding material for plasmonic waveguides and microfluidic channels in this study, as will be described in detail in Chapter 7 [87].

Type	End functional group	Characteristics	Example of application
Type A	— COOH	• Metal and glass can be coated by using a silane coupling agent together with this type of CYTOP • Plastic can be coated by using a special primer together with this type of CYTOP • Transparent to visible light	Anti-reflection film Optical membrane Protective layer Water and oil repellent Electric insulator
Type M	— CONH ~ Si(OR)n	• One-step coating of metals and glass can be done.	Protective layer Water and oil repellent Electric insulator
Type S	— CF_3	• High transparency for wide range of light from visible light to UV • Tough UV resistance • Non-adhesion	Pellicle Optical materials Mold release material

Fig. 14: CYTOP functional groups: characterizations and applications (adopted from [85]).

2.4.3 Photolithography and metallization technique

Bilayer lift off photolithography is the most common technique that is used in microfabrication processes to define sharp features [88]. This technique is well suited to mass manufacturing, where a large number of identical devices can be produced [89]. In this technique a lift off resist is applied to the substrate followed by a photoresist. The wafer is then subjected to UV light, passing through a patterned hard mask. Once developed using TMAH based developers (wet etching), the exposed

photoresist is selectively removed (positive tone resist), or selectively remained (negative tone resist) [90], creating a re-entrant profile through which the metal is deposited on the wafer surface. The bilayer profile helps to avoid the accumulation of metal on the side walls of the features hence improving the quality of the sharp edges. The process flow is described schematically in Fig. 15.

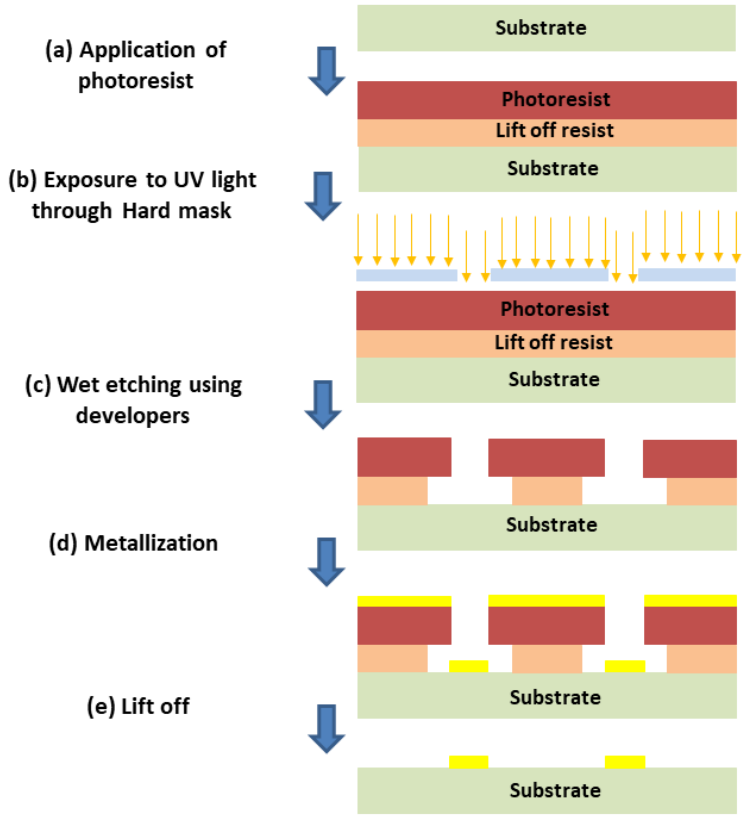

Fig. 15: Process flow describing photolithography and metallization technique

The minimum feature size that can be resolved using photolithography depends on the wavelength of the exposure source. The conventional sources for photolithography are ultraviolet and deep ultraviolet, as listed in Table 1 [90].

Exposure Source	Minimum Feature Size (nm)
Ultra Violet (UV)	456
Deep Ultra Violet (DUV)	196
Extreme Ultra Violet (EUV)	16.8

Table 2.1. Summary of minimum feature size for different exposure sources [90]

2.4.4 Electron beam lithography

Electron beam lithography is capable of creating custom patterns with sub 20 nm resolution [91]. In this technique, the substrate is covered with an electron beam sensitive resist (i.e PMMA) and is exposed to the electron beam. The exposure is performed by direct writing using a focused electron beam, and thus doesn't require a physical mask. The exposure changes the solubility of the resist compared to non-exposed areas (for positive resists) which yields to selective removal of the resist profile in the photoresist developer. MIBK (methyl-isobutyl-ketone) is a common developer which is used for the selective removal of positive e-beam resists such as PMMA.

The schematic of an electron beam system is shown in Fig. 16. The system is mainly composed of an electron gun, an aperture (with variable sizes), a stigmator, a deflecting system (comprised of magnetic coils and electrostatic elements, called electron optics) and a translation stage [90].

Proximity effects and stich field errors are the main drawbacks of electron beam lithography technique. In addition to that, the serial nature of this process and its high cost is a limiting factor. A "write-field" alignment procedure is used to align the e-beam deflection system to the high precision laser-controlled translation stage. The electron beam covers the area within a

write-field size, without moving the stage. If the pattern is larger than the write-field size, it will be divided into several write fields, which results into stich errors due to misalignment between adjacent write fields. This error can be minimized by an accurate write-filed alignment. Various types of electronic signals are produced in an electron beam system including secondary electrons and back-scattered electrons. Back-scattered electrons are reflected from the sample by elastic scattering, and cause beam size broadening and proximity effects [92]. Proximity effects can be reduced by correcting the e-beam exposure dose in densely patterned areas, or by adding corrective features to the layout.

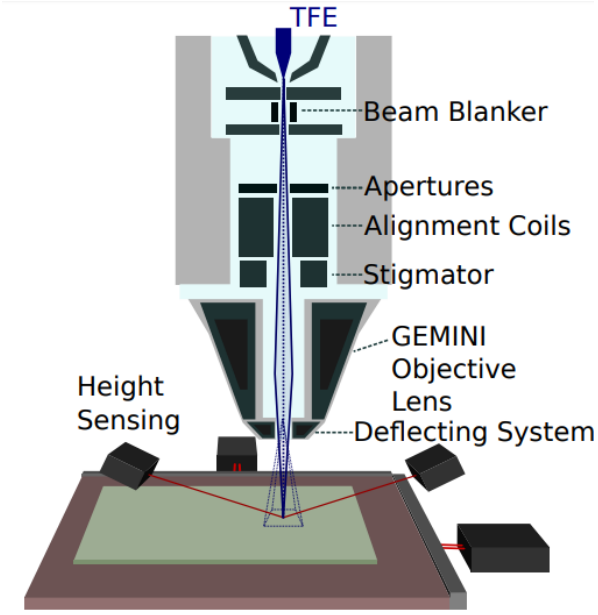

Fig. 16: A typical electron-beam lithography system (adapted from [93])

2.4.5 Dry etching

Etching is the process of selective removal of material from a wafer using chemicals. Wet etching and dry etching are the most common etching techniques. In wet etching, a solvent (called

developer) or an acid or a base, is used to selectively remove the material from the wafer. Dry etching is achieved by exposing the material to ionized gases (plasma) in a vacuum chamber that removes a portion of material from the surface. Dry etching processes could be isotropic or anisotropic. The schematic of a reactive ion etching (RIE) system is shown in Fig. 17.

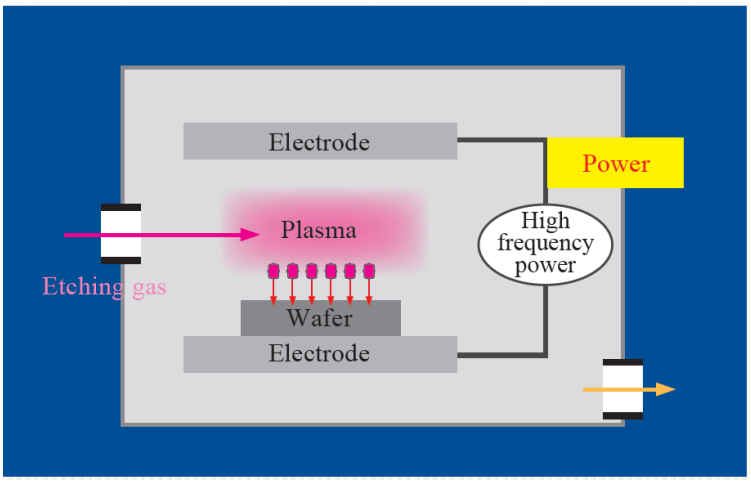

Fig. 17: Typical reactive ion etching system (adapted from [85])

The system is constructed on a vacuum chamber. The gas enters through inlets and exits through the vacuum pump. A strong electromagnetic field is induced between the electrodes, creating a plasma cloud by removing electrons from the gas molecules. O_2, Ar, CF_4 and SF_6 are common gases that are used in reactive ion etching systems. The amount of power, the flow rate and the type of the gas (or combination of gases) are among the parameters to be optimized to achieve a high selectivity etching process [94].

2.4.6 Wafer bonding

Wafer bonding is a packaging technique on wafer level for the fabrication of microelectronic devices and microelectromechanical systems (MEMS). Direct bonding, surface activated bonding,

plasma activated bonding, anodic bonding and adhesive bonding are among the most common bonding techniques. In direct bonding, no additional intermediate layer is introduced into the wafers and chemical bonds form the basis of the bonding process [95]. In surface activated bonding the wafer surfaces are activated using a vacuum process such as ion beam etching or fast atom bombardment prior to bonding [96]. In plasma activated bonding the wafers are exposed to a low pressure plasma prior to the bonding [97]. In this technique, reactive ion etching (RIE), inductively coupled plasma (ICP), and ultraviolet radiation plasma are performed using different gases environments [98]. Anodic bonding consists of bonding glass to either silicon or metal without introducing any intermediate layer [99]. The most common glass materials used in this technique are Pyrex and Borofloat. Adhesive bonding consists of applying an intermediate layer to connect substrates of different material. Fluoropolymers such as CYTOP can be used as an intermediate layer in adhesive bonding. CYTOP exhibit softening behaviour above its glass transition temperature (T_g), which will result in the formation of new polymer bonds. CYTOP adhesive bonding require much lower temperature (150 -200 °C) compared to other bonding technique such as anodic bonding (~350 °C) [100-102]. High bonding temperature is a major draw-back of such techniques which will increase the risk of damage to thermally sensitive devices during the bonding process. In this work an adhesive bonding process using CYTOP is employed to bond the substrate to borofloat silica cap as will be described in full detail Chapter 6. The wafer is covered with CYTOP as the upper cladding with etched microfluidic channels, and wafer-bonded to a borofloat silica wafer (also covered with CYTOP) to encapsulate the fluidic channels and enable side fluidic interfaces.

Chapter 3

Biomolecular kinetics analysis using long range surface plasmon waveguides

3.1 Summary

Biomolecular kinetics analysis of protein-protein interactions using LRSPP waveguides is presented in this chapter. Biomolecular interaction analysis (BIA) is used in drug discovery applications within the pharmaceutical fields, as well as for studying antibody-antigen interactions and assay development as will be described in Chapter 4. Binding kinetics are defined as the rates that molecules such as ligands and receptors bind to and disassociate from each other. The goal of ligand-receptor kinetics analysis is to determine the association and disassociation rate constants of the interaction from experimental kinetics or equilibrium data. In this chapter we investigate the feasibility of extracting the binding kinetics of protein-protein interaction using our LRSPP waveguide biosensors. Our biosensor technology is capable of rapid, direct and real time detection and characterization of biomolecular interactions. In addition to that, our biosensor technology provides higher sensitivity, more compact footprint and mass manufacturing advantages. We use BSA and anti-BSA as the bio-pair to carry out the experiments. Antibodies in the form of lyophilized powder is mixed with the buffer solution to avoid bulk steps in the experimental cycle. In these series of experiments BSA is immobilized on the sensor surface using thiol chemistry while anti-BSA is injected on top of the immobilized protein. The output power of the system is

monitored continuously over time using an optical setup consisting of DFB laser, PM fiber, objective lens, aperture, beam splitter and power sensor. Two different approaches namely linear and non-linear least square analysis are employed to extract the binding kinetics of the interaction. An exponential fit in the form of $f(x) = a \times \exp(1 - bx)$ is used (following the general form of the integrated rate equation) where *a* and *b* are coefficients that are extracted from the fit with 95% confidence bound. The results that are obtained using linear and non-linear least square analysis are in a very good agreement with each other and with the values reported in literature for protein-protein interactions.

3.2 Contributions

The results provided in this chapter are published in ***Sensors and Actuators B: Chemical***, Volume 243, 2017. Maryam Khodami established the kinetics model and carried out the experimental work. Maryam Khodami extracted the binding kinetics from raw experimental data using curve fitting algorithms in MATLAB. Biosensor chips used in these series of experiments were fabricated by Saad Hassan, former member of Berini's group. Maryam Khodami interpreted the results and wrote the manuscript. Pierre Berini contributed to the interpretation of the results and revised the manuscript.

3.3 Article

The article follows here verbatim.

Sensors and Actuators B 243 (2017) 114–120

Contents lists available at ScienceDirect

Sensors and Actuators B: Chemical

journal homepage: www.elsevier.com/locate/snb

Biomolecular kinetics analysis using long-range surface plasmon waveguides

Maryam Khodami[a,b], Pierre Berini[a,b,c,*]

[a] School of Electrical Engineering and Computer Science, University of Ottawa, 800 King Edward Ave., Ottawa, Ontario, K1N 6N5, Canada
[b] Centre for Research in Photonics, University of Ottawa, 25 Templeton Ave., Ottawa, Ontario K1N 6N5, Canada
[c] Department of Physics, University of Ottawa, 150 Louis Pasteur Ave., Ottawa, Ontario K1N 6N5, Canada

ARTICLE INFO

Article history:
Received 29 June 2016
Received in revised form 1 November 2016
Accepted 23 November 2016
Available online 24 November 2016

Keywords:
Kinetics
Biosensors
LRSPP
SPR
BSA
Antibody

ABSTRACT

A novel, cost effective, label free and real time biosensor based on straight gold waveguides supporting long range surface plasmon polaritons (LRSPPs) is used to measure the kinetics constants of protein–protein interactions. Bovine serum albumin (BSA) and anti-bovine albumin antibody (anti-BSA) produced in rabbit are used as the bio-pair for the purposes of demonstrating and investigating the extraction of binding kinetics. BSA protein is immobilized on the surface using thiol coupling. The output power of the system is recorded continuously over time, and then converted into surface mass concentration. The kinetics constants are extracted from binding curves using the integrated rate equation. Linear least squares and non-linear least squares analysis are employed to obtain the constants and the results are compared.

1. Introduction

The characterization of biomolecular affinity and interaction kinetics is important to understand antibody-antigen or generally protein–protein interaction for the selection of appropriate biomaterials for immunoassays, or for drug discovery within the pharmaceutical fields [1]. Methods that detect changes in refractive index based on changes in surface mass concentration (*e.g.*, optical biosensors) [2,3] or changes in fluorescence [4–6] can be employed for kinetics analysis. Optical biosensors are capable of providing rapid, direct and real-time detection and characterization of biomolecular interactions. Among all of the technologies, surface plasmon resonance (SPR) has demonstrated strong potential as an optical biosensor technology for label-free and real-time detection of reagents. SPR biosensors utilize the Kretschmann-Raether configuration which is based on total internal reflection from a metal-coated prism [7–9].

Long-range surface plasmon polaritons (LRSPPs) are transverse magnetic (TM) polarized optical surface waves propagating along a thin metal film or stripe. LRSPPs on stripes can be excited by butt-coupling to a polarisation-maintaining single-mode optical fiber (PM-SMF) [10,11]. LRSPPs can propagate over appreciable lengths, allowing a long optical interaction with the sensing medium, and thus high-sensitivity, real-time, label-free biosensors. LRSPPs have been excited in prism-coupled sensors in order to increase the sensitivity of the device, and used in the detection of *E. coli* bacteria [12] and for studying the effects of toxins on HEK-293 cells [13]. LRSPP biosensors based on metal stripe waveguides offer advantages over prism-coupled sensors, in the form of increased sensitivity, compactness, and ease of manufacturing. Dengue virus detection [14,15], bacteria detection in urine [16] and the detection of leukemia markers [17] has been performed using LRSPP biosensors. In the case of Dengue detection, the surface was activated using EDC/NHS, patient blood samples were immobilized on the surface and the results show similar or better detection than ELISA [14]. In the case of Leukemia detection, the surface was activated using protein G and antibodies from patient samples were immobilized selectively on the surface [17].

In this paper, we demonstrate LRSPPs biosensors based on metal stripe waveguides for the analysis of the affinity and kinetics rate constants of biomolecular interactions. We work with bovine serum albumin (BSA) and antibodies against BSA (anti-BSA) produced in rabbit. BSA is a protein of molecular weight ~66 KDa used extensively in routine biosensor work and it is inexpensive. The analysis technique employed here is based on the immobilisation

* Corresponding author at: School of Electrical Engineering and Computer Science, University of Ottawa, 800 King Edward Ave., Ottawa, Ontario, K1N 6N5, Canada.
E-mail addresses: [redacted] (M. Khodami), berini@eecs.uottawa.ca (P. Berini).

http://dx.doi.org/10.1016/j.snb.2016.11.120
0925-4005/

of BSA on the gold stripe surface, while anti-BSA is injected over the surface and its reaction with BSA is observed. Changes in the output power are recorded continuously over time, which are then translated to changes in surface mass density [18]. On this basis, the kinetics rate constants can be extracted, *e.g.*, by fitting responses to the rate or integrated rate equations. Compared to conventional SPR systems, LRSPP biosensors based on metal stripes are more compact and cost-effective [19,20].

This paper is organised as follows: First we summarise our theoretical model for the system and interaction kinetics, then the materials and methods. We then present our results along with a discussion and close the paper with concluding remarks.

2. Theoretical model

Kinetics analysis for the interaction of immobilized receptor and soluble analyte, BSA and Anti-BSA in our case, can be done through real-time monitoring of the output signal. In our LRSPP biosensors, changes in the output power indicate binding events occurring along the surface of the metal stripe. The output power is monitored continuously over time and plotted as the sensorgram.

In general, the interaction between two biomolecules A and B can be modelled as:

$$A + B \leftrightarrow AB \tag{1}$$

The rate of this reaction can be expressed as:

$$d[AB]/dt = k_a[A][B] - k_d[AB] \tag{2}$$

where k_a is the association rate constant and k_d is the disassociation rate constant (concentrations are implied by square brackets). The concentration of B can be expressed in terms of its initial concentration and the concentration of complex AB, after an interaction time t, as $[B] = [B]_0 - [AB]$. Substituting this into Eq. (2) yields:

$$d[AB]/dt = k_a[A]([B]_0 - [AB]) - k_d[AB] \tag{3}$$

Based on the above, the net rate of formation of complex AB depends on the concentrations of A and B as well as the interaction kinetics. In our biosensor application, B represents the receptor immobilized on the surface of the device, and A soluble analyte, so complex AB forms on the surface of the device as A in solution binds to B immobilized thereon. The output signal is dependent on the concentration of complex AB forming on the surface which can be expressed, generally, in terms of surface mass density Γ. By analogy with Eq. (3), we write the time rate of change of the surface mass density accumulating on the surface as:

$$d\Gamma/dt = k_a C(\Gamma_{max} - \Gamma) - k_d\Gamma \tag{4}$$

where C is the concentration of the injected analyte. At equilibrium $d\Gamma/dt = 0$ and rearranging Eq. (4) yields:

$$\Gamma/C = k_a/k_d(\Gamma_{max} - \Gamma) \tag{5}$$

where k_a/k_d is defined as the affinity constant K. The affinity constant can thus be obtained as the slope of a plot of Γ/C vs. Γ. Rearranging Eq. (4) yields:

$$d\Gamma/dt = k_a C\Gamma_{max} - (k_a C + k_d)\Gamma \tag{6}$$

where the concentration C and the maximum surface mass density Γ_{max} are known. The rate constants k_a and k_d can be extracted from this equation by plotting $d\Gamma/dt$ *vs.* Γ. Different slope values k_s for such plots are obtained for different analyte concentrations C:

$$k_s = k_a C + k_d \tag{7}$$

Using this equation, the association and disassociation rate constants can be obtained from the slope and the intercept of the k_s *vs.* C plot, respectively. The extraction of the disassociation rate constant is more error prone, because k_d values are usually small.

The integrated rate equation is obtained by solving Eq. (6) directly, yielding:

$$\Gamma = \frac{k_a C\Gamma_{max}\left[1 - e^{-(k_a C + k_d)t}\right]}{(k_a C + k_d)} \tag{8}$$

Alternatively, the integrated rate equation can be used directly to extract the binding kinetics through fitting as will be discussed in the results and discussion section of the paper.

In our LRSPP biosensors, changes in the output power indicate binding events occurring along the surface of the metal stripe, and thus changes in surface mass density thereon. The surface mass density can be related to the output power via [18,21]:

$$\Gamma(t) = \frac{1}{k}\left(\frac{n_a - n_c}{\partial n/\partial c}\left(\frac{P_{out}(t)}{P_{out}(t_b)} - 1\right)\right) \tag{9}$$

where Γ is the surface mass density (pg/mm^2), k is 0.0318/nm [18] (a device constant), n_a and n_c are the refractive index of the biomaterial accumulating on the surface and of the carrier fluid, 1.5 and 1.338, respectively [18], $\partial n/\partial c$ is 0.185 mm^3/mg [22], and $P_{out}(t_b)$ and $P_{out}(t)$ are the output powers measured before and during analyte binding.

3. Materials and methods

3.1. Chemicals and reagents

16-Mercaptohexadecanioc acid (16-MHA), phosphate buffered saline (PBS) 0.01 M, pH 7.4, bovine serum albumin (BSA), sodium dodecyl sulfate (SDS), 2- isopropanol alcohol (IPA), acetone HPLC grade ≥99.9, octane, glycerol (electrophoresis grade), N-Hydroxysuccinimide sodium salt (NHS), 1 -ethyl-3-(3-dimethylaminopropyl) carbodiimide hydrochloride, ≥99% (EDC) and anti-BSA antibody produced in rabbit were obtained from Sigma-Aldrich. Distilled water was deionized using Millipore filtering membranes (Millipore, Milli-Q water system at 16 MΩ cm).

The buffer used in the experiments was prepared by mixing PBS and glycerol (PBS/Gly) to achieve a refractive index of n = 1.338 at the wavelength of operation (~1310 nm), in order to achieve an approximate refractive index match to Cytop and high sensitivity [18]. The pH of the solution remains constant throughout the experiments. The lab temperature also remains constant at 25 °C and all solutions are allowed to stabilise to lab temperature before use.

100 μg/mL and 20 μg/mL BSA solutions were prepared by mixing lyophilized BSA with PBS/Gly buffer. Different antibody concentrations, (1 μg/mL, 5 μg/mL, 30 μg/mL and 100 μg/mL) were prepared by mixing powdered antibody with PBS/Gly buffer.

1% SDS was prepared in PBS/Gly for the purposes of disrupting Anti-BSA to BSA binding in order to regenerate the receptor surface.

3.2. Sensing device and instrumentation

LRSPP straight waveguides composed of gold stripes embedded in CYTOP with a fluidic channel etched into the top cladding were used as the sensing structure in the experiments. The device is fabricated using optical lithography to define Au features on a bottom cladding of CYTOP. A fluidic channel of length L = 1.65 mm (sensing length) was formed by etching the top CYTOP cladding down to the gold surface. Fabrication details can be found in [23]. The sensor die incorporated straight waveguides with a Au stripe 5 μm wide, 35 nm thick and 3.8 mm in length.

An optical setup comprised of a DFB laser, a cleaved PM-SMF, a collimating objective, an aperture, a beam splitter and a power sensor, as sketched in Fig. 1, was used to capture the output of a straight

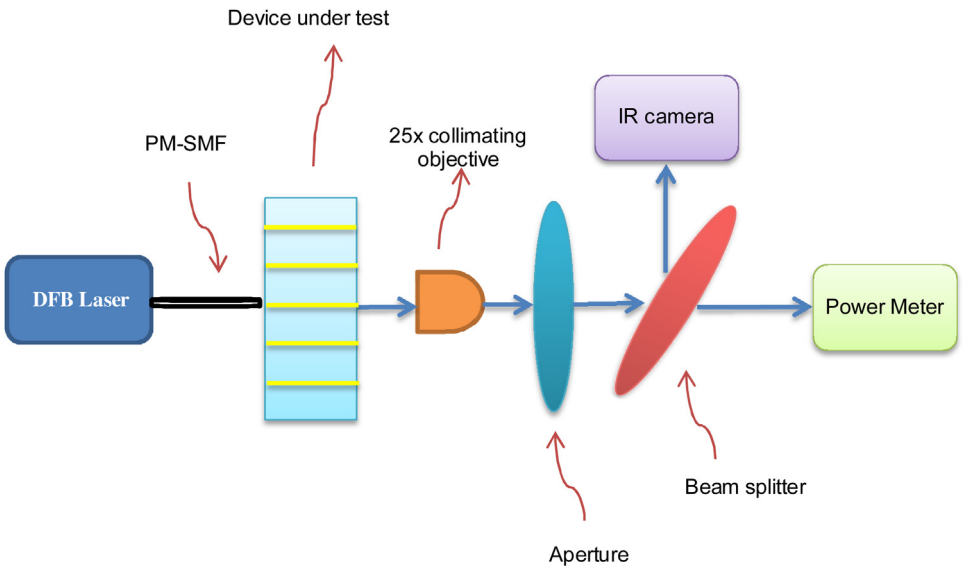

Fig. 1. Optical setup used to measure the output power.

waveguide. The buffer solution was injected into the fluidic channel using a syringe pump at a constant flow rate of 20 μl/min. The output power was measured using a power sensor and recorded using Labview.

3.3. Device preparation

A sensor device was cleaned by ultra-sonication in octane for 5 mins to remove possible debris on the sensor facets left behind by the dicing process. Then the device was left in a first acetone bath for 5 mins to remove most of the dicing photoresist, then in a second acetone bath for another 30 mins to completely clean the device. After that, the sensor was rinsed with IPA and dried with nitrogen gas. To remove any organic material from the sensor surface, the device was placed in a UV ozone chamber with the UV lamp on for 30 mins and then off for another 30 mins. The clean sensor was then stored in 1 mM 16-MHA solution in IPA for 24 h for the formation of the self-assembled monolayer (SAM). Before assembling the device into the fluidic jig, it was rinsed with IPA and distilled/deionized water (DDI H2O), and then dried with nitrogen gas. The final steps in this protocol, consisting of rinsing with IPA and DDI H2O, UV ozone cleaning and storing in 16-MHA solution, can be repeated sequentially after each experiment in order to fully regenerate the device down to the gold surface, in order to perform a subsequent experiment. The sensor facet quality would eventually deteriorate after 4 to 5 regeneration cycles, causing loss of power and an increase in background light.

4. Results and discussion

The sensorgram presented in Fig. 2 shows a full experimental sequence, including the interaction between immobilized BSA and Anti-BSA in solution. The sensor surface was first carboxylated with a self-assembled monolayer (SAM) of 16-MHA applied through incubation. A solution of EDC/NHS in buffer (0.1 M NHS and 0.1 M EDC) was flowed for 15 mins to activate the carboxyl groups, followed by a buffer rinse. The large drop in signal observed during EDC/NHS injection is due to the change in refractive index of the solutions (bulk step). BSA was then immobilized on the sensor surface through amine coupling. BSA immobilisation is followed by the injection of Anti-BSA over 20 min, then by disassociation of Anti-BSA during the buffer rinse, and finally, regeneration of the surface down to the BSA level using an SDS wash for 20 min. The buffer baseline at the level of BSA is recovered after the SDS wash, indicating essentially complete removal of Anti-BSA, enabling the BSA surface to be re-used in a subsequent iteration. The experiments were performed at the constant flow rate of 20 μl/min, unless otherwise specified—for instance, the EDC/NHS and antibody flows were stopped after 5 mins and the system maintained under static conditions for the rest of the injection period to reduce biomaterial consumption.

In previous studies [14,15], it has been shown that the surface could be regenerated using 0.5% SDS without affecting its immunoreactivity. In this study 0.5% SDS was used initially to regenerate the surface but this concentration was not high enough to break the BSA antibody-antigen binding. As a result the buffer level after SDS wash was not retrieved and consequently there was no antibody binding in the second repeat. By increasing the SDS concentration to 1%, the surface was regenerated down to the BSA level, as shown in Fig. 2.

The choice of BSA concentration to form the immobilized layer of BSA in this set of experiments was 20 μg/mL (in solution). 20 μg/mL BSA produces a surface mass coverage equal to 1450 pg/mm^2 (according to BSA binding portion of Fig. 2), which is equivalent to 21×10^{-15} mol/mm^2.According to [19], the amount of immobilized receptor should be kept as low as possible to avoid mass transport limitations. However, the concentration of immobilized receptor should be high enough to produce a reliable binding rate. The recommended range for the surface concentration of immobilized receptor is $5–20 \times 10^{-15}$ mol/mm^2 [19]. In our set of experiments a second BSA concentration of 100 μg/mL (in solution) was used to form the immobilized layer of BSA, and the kinetics constants obtained from that set of experiments was close to those obtained with 20 μg/mL, confirming that we are not operating in the mass transport limited regime.

Fig. 3 presents the normalized output power *vs.* time for 4 different antibody concentrations. The measured power in dBm is converted to μW and normalized to the power level before the antibody injection (baseline level): $P_{out}(t)/P_{out}(t_b)$—as identified in Fig. 2. The power level drops as the antibody binds to the antigen. By decreasing the antibody concentration, the power drop also decreases, as expected, due to less mass accumulating on the surface of the biosensor. The power drop due to the antibody-antigen

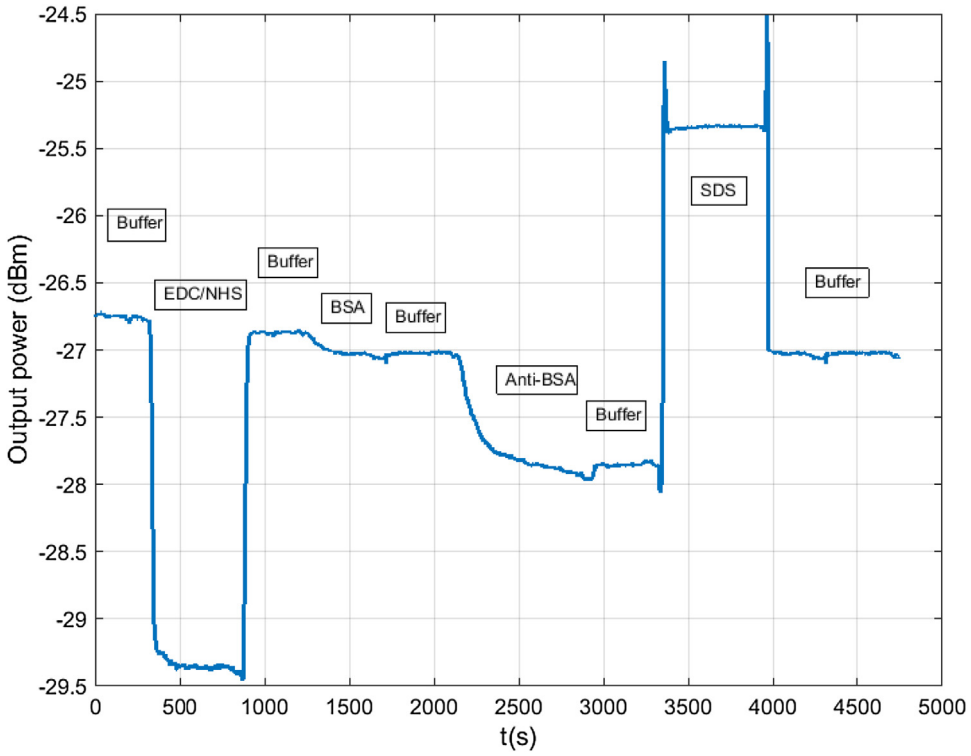

Fig. 2. Sensorgram of a complete experimental cycle, illustrating anti-BSA/BSA interaction and regeneration of the surface down to the BSA level. The power level before the antibody injection is considered as the baseline level. The normalized power is obtained by dividing the output power to the baseline.

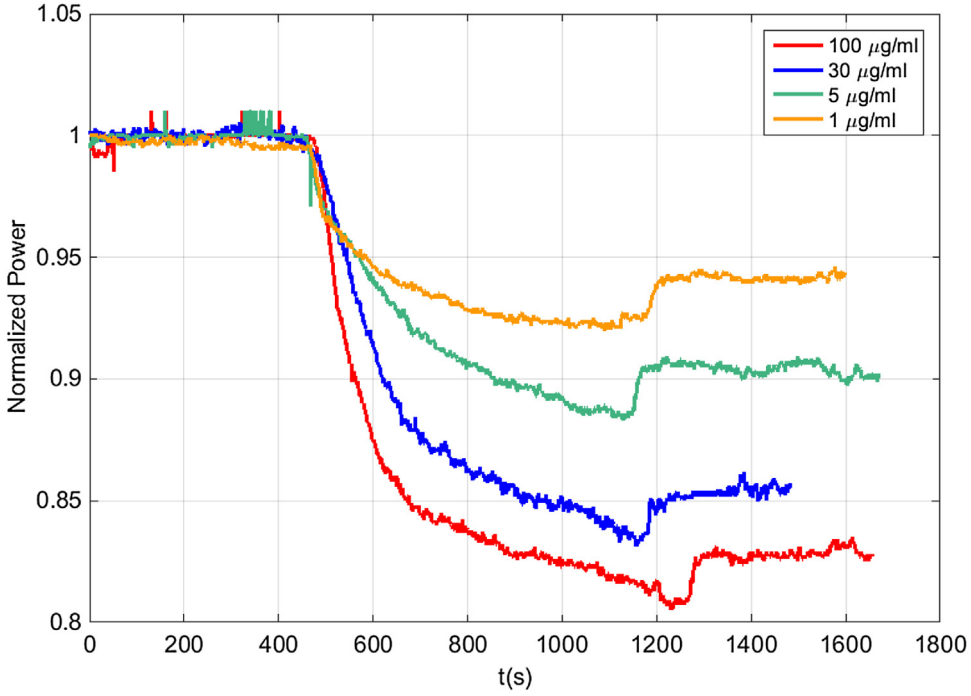

Fig. 3. Normalized output power ($P_{out}(t)/P_{out}(t_b)$) for different Anti-BSA concentrations on a BSA surface (BSA immobilisation concentration of 20 μg/mL in solution).

interaction can be converted to changes in surface mass density using Eq. (9).

Fig. 4 represents the surface mass density *vs.* time for 4 antibody concentrations. As can be seen in this figure, the binding curves are noisy which prevents us from taking the derivative of the data directly, as required by Eq. (6). In order to produce noiseless binding curves, the data was modelled by fitting to an exponential model (using the Curve Fitting Toolbox in Matlab). Fig. 5 shows the fitted curves to the data for the 4 antibody concentrations.

The inset to Fig. 4 shows the repeats (after SDS wash) for the concentration of 100 μg/mL. The surface mass density is plotted *vs.* time for the first antibody injection as well as the first repeat (second injection) and the second repeat (third injection). As can be seen from this inset, the first and second repeats after SDS wash,

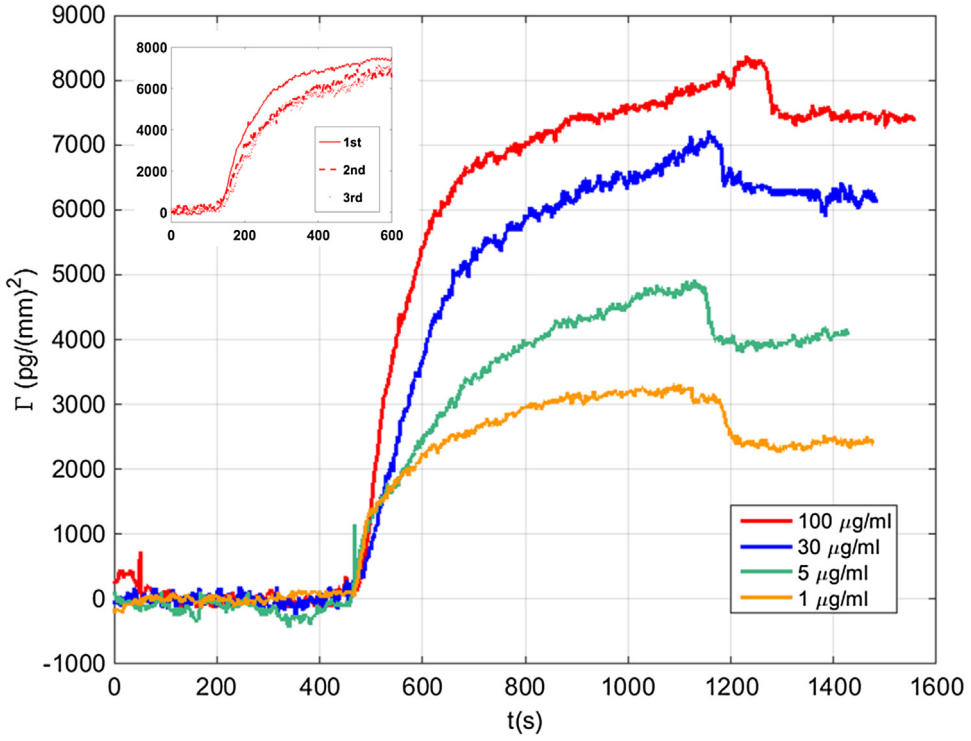

Fig. 4. Surface mass density for different Anti-BSA concentrations on a BSA surface (BSA immobilisation concentration of 20 μg/mL in solution). The inset shows the antibody repeats for the concentration of 100 μg/mL.

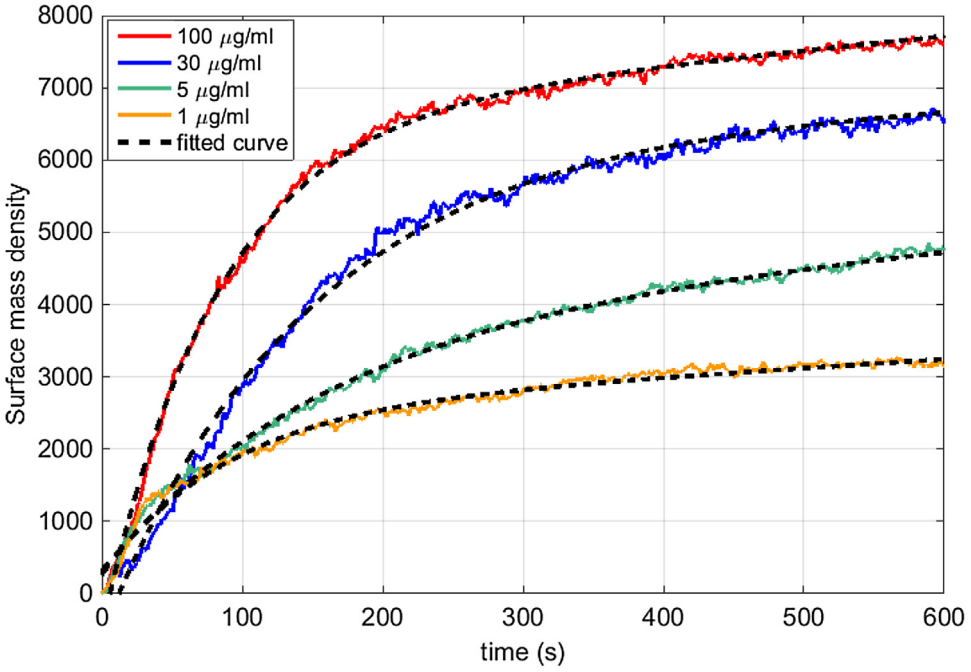

Fig. 5. Surface mass density responses during the association phase along with fitted curves (black dash).

produces a binding curve which is comparable to the initial antibody binding before the SDS washes. This confirms that the washing protocol has minimum impact on the immobilized BSA on the surface.

One approach to obtain the kinetic constants from the binding curves is based on the linear least squares regression described in [19]. Each binding curve was plotted as dΓ/dt *vs.* Γ following Eq. (6), as shown in Fig. 6, with $d\Gamma/dt$ computed form the noiseless fits (black dashed curves in Fig. 5) over the time interval ranging from 300 s to 600s. The slope value k_s is obtained from each plot, and plotted *vs.* antibody concentration C, as shown in Fig. 7. Based on Eq. (7) the slope of this line is the association constant k_a, which works out to $9.37 \times 10^3\ M^{-1}\ s^{-1}$, and the intercept value represents the dissociation constant k_d which is equal to $3.6 \times 10^{-3}\ s^{-1}$.

The association and disassociation constants obtained from this set of experiments are within the expected range for Anti-BSA/BSA

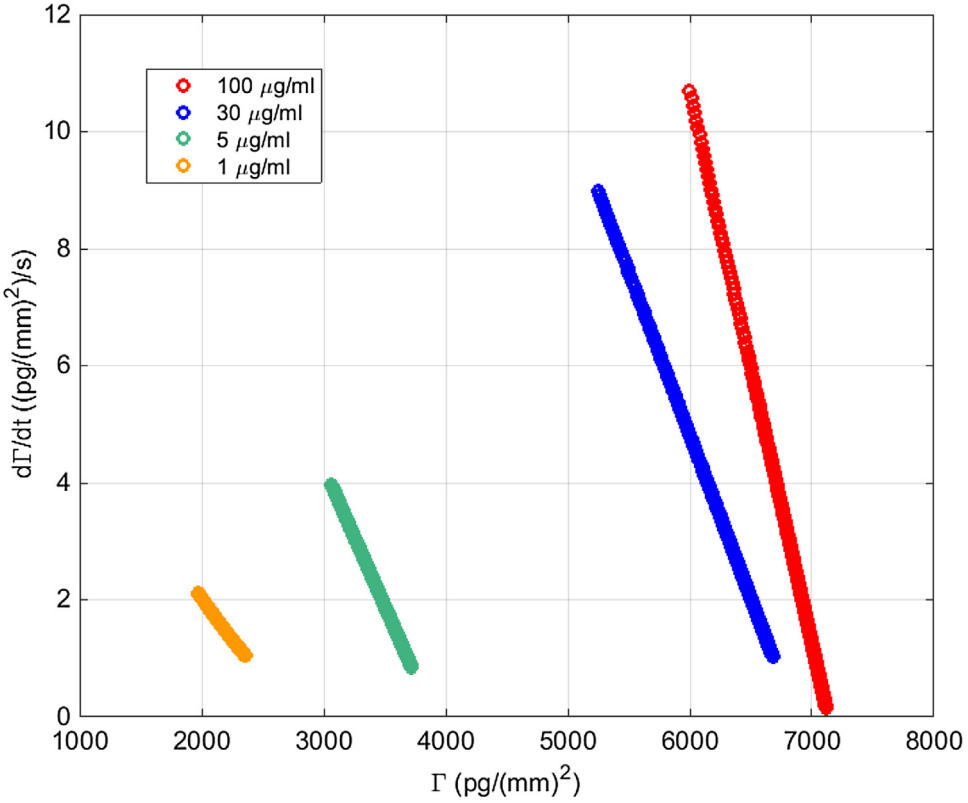

Fig. 6. Binding rate *vs.* response.

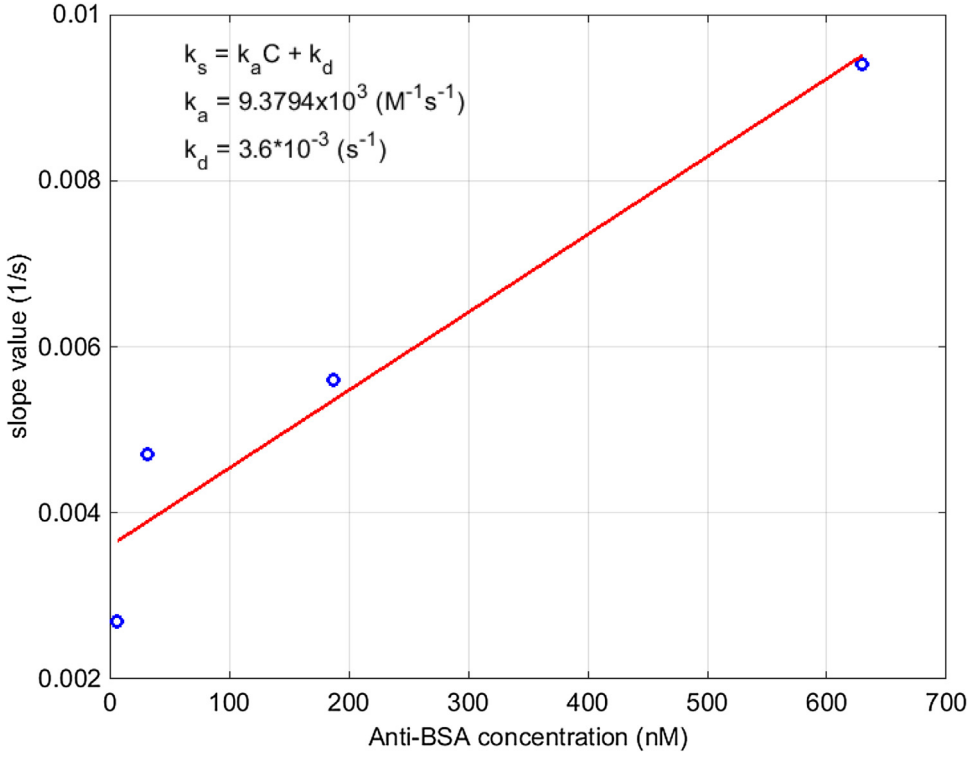

Fig. 7. Slope value k_s *vs.* Anti-BSA concentration C on a BSA surface (BSA immobilisation concentration of 20 μg/mL in solution). From the slope of the curve, $k_a = 9.37 \times 10^3\ M^{-1}\ s^{-1}$ and the intercept value $k_d = 3.6 \times 10^{-3}\ s^{-1}$.

Table 1
Rate constants obtained from three iterations using SDS wash.

Repeat	k_a ($M^{-1}s^{-1}$)	k_d (s^{-1})
1	9.37×10^3	3.6×10^{-3}
2	8.02×10^3	3.8×10^{-3}
3	10.25×10^3	4.3×10^{-3}

interaction. k_a and k_d obtained in [24] are 9.36*10$\hat{3}$ M^{-1} s^{-1} and 7.85*10^−3 s^{-1}, respectively.

Since the value of k_d obtained from the intercept in Fig. 7 is small, it is more error prone. In this reaction, the Anti-BSA binds to BSA very tightly so only small changes are observed in the signal due to disassociation in buffer flow (Fig. 4). Thus, the disassociation constant is more error prone due to the small changes in the signal in comparison with the noise level. For this reason, the disassociation portion of the binding curves (Fig. 4) cannot be used directly to extract k_d.

The affinity constant K can also be extracted from the curves, by plotting Γ/C vs. Γ (Eq. (5)). Based on that the affinity constant K works out to 1.58×10^6 M^{-1}. On the other hand the affinity constant can also be obtained directly from the ratio k_a/k_d which yields 2.6×10^6 M^{-1}. The values obtained for the affinity constant are slightly different due to the error in the k_d value.

The set of experiments were repeated 3 times for each concentration using an SDS wash between repeats to regenerate the surface down to the BSA level. The values of k_a and k_d for each iteration are reported in Table 1. We observe that the association and disassociation constants are reproducible to within ±15%.

Another approach to extract the kinetic constants from the binding curves is based on nonlinear least squares fitting of the integrated response to the curves (Eq. (8)), as described in [20]. As opposed to the linear least square analysis, which requires multiple binding curves for different concentrations to extract single values for the rate constants, each binding curve can be fit separately to the integrated rate equation. Using the MATLAB curve fitting toolbox, Eq. (8) was fit to the curves of Fig. 4, and the values of k_a and k_d were extracted directly. It should be noted that the single exponential model described in Eq. (8) is valid only when there is a single interaction between species A and B. if there is more than one interaction in the system (*e.g.* nonspecific binding), the single exponential integrated rate equation cannot be used. In that case, the kinetics interaction could be described using a double exponential [20]. Since a single exponential model fits our data accurately, nonspecific binding in our system is negligible, and the binding curves used to extract the kinetic constants just represent the interaction between BSA and Anti-BSA.

The average values of the association and disassociation constants obtained using nonlinear least squares fitting of the integrated response are $k_a = 9.1 \times 10^3$ $M^{-1}s^{-1}$ and $k_d = 3.25 \times 10^{-3}$ s^{-1}. The rate constants thus obtained are very similar to those obtained using the first approach (Table 1), but it should be noted that, the disassociation rate constant extracted from the association part of the curve is error prone due to the strong binding affinity of the antibody and antigen and the noise level, as discussed above. The nonlinear least squares method is advantageous in that it allows for the determination of the kinetics rate constants for each binding experiment, while the linear least squares approach requires multiple binding curves to extract the binding kinetics.

5. Conclusion

In conclusion, we extracted the binding kinetics constants for anti-BSA/BSA interaction using our LRSPP biosensor. The binding curves are obtained by monitoring the output power of the system continuously over time and converting the raw data to surface mass concentrations. The affinity and kinetics constants obtained are within the range expected for this interaction. The repeatability of the results was confirmed using surface regeneration, with the binding constants remaining within ±15% of the mean.

Acknowledgments

The authors gratefully acknowledge Anthony Olivieri, Ewa Lisicka-Skrzek, Oleksiy Krupin and Wei Ru Wong for their assistance.

References

[1] M.A. Cooper, Nat. Rev. Drug Discov. 1 (2002) 515–528.
[2] S. Kumbhat, K. Sharma, R. Gehlot, A. Solanki, V.J. Joshi, Pharm. Biomed. Anal. 52 (2010) 255–259.
[3] A.R. Camara, A.C.M. Dias, P.M. Gouvêa, A. Braga, R.F. Dutra, R.E. Araujo, I.C. Carvalho, In Workshop on Specialty Optical, Sigtuna, Sweden, Aug 28–30, 2013; Optical Society of America: Washington, DC, 2013.
[4] N.V. Zaytseva, R.A. Montagna, E.M. Lee, A.J. Baeumner, Anal. Bioanal. Chem. 380 (2004) 46–53.
[5] N.V. Zaytseva, R.A. Montagna, A.J. Baeumner, Anal. Chem. 77 (2005) 7520–7527.
[6] Y. Zhang, J.T. Bahns, Q. Jin, R. Divan, L. Chen, Anal. Biochem. 356 (2006) 161–170.
[7] J.M. Malmqvist, Nature 361 (1993) 186–187.
[8] J. Homola, Chem. Rev. 108 (2008) 462–493.
[9] S. Lofas, Assay Drug Dev. Technol. 2 (2004) 407–416.
[10] P. Berini, Adv. Opt. Photon. 1 (2009) 484–588.
[11] P. Berini, New J. Phys. 10 (2008) 105010.
[12] M. Vala, S. Etheridge, J. Roach, J. Homola, Sens. Actuators B 139 (2009) 59–63.
[13] V. Chabot, Y. Miron, M. Grandbois, P.G. Charette, Sens. Actuators B 174 (2012) 94–101.
[14] W.R. Wong, O. Krupin, S.D. Sekaran, F.R.M. Adikan, P. Berini, Anal. Chem. 86 (2014) 1735–1743.
[15] W.R. Wong, S.D. Sekaran, F.R.M. Adikan, P. Berini, Biosens. Bioelectron. 78 (2016) 132–139.
[16] P. Béland, O. Krupin, P. Berini, Biomed. Opt. Express 6 (2015) 2908–2922.
[17] O. Krupin, P. Berini, Lab Chip 15 (2015) 4156–4165.
[18] W.R. Wong, O. Krupin, F.R.M. Adikan, P. Berini, J. Lightwave Technol. 33 (2015) 3234–3242.
[19] R. Karlsson, A. Michaelsson, L. Mattsson, J. Immunol. Methods 145 (1991) 229–240.
[20] D.J. O'shannessy, M. Brigham-Burke, K. Soneston, P. Hensley, I. Brooks, Anal. Biochem. 212 (1993) 457–468.
[21] O. Krupin, W.R. Wong, P. Béland, F.R.M. Adikan, P. Berini, J. Lightwave Technol. 34 (2016) 4673–4681.
[22] J.A. De Feijter, J. Benjamins, F.A. Veer, Biopolymers 17 (1978) 1759–1772.
[23] C. Chiu, E. Lisicka-Skrzek, R.N. Tait, P. Berini, J. Vac. Sci. Technol. B 28 (2010) 729–735.
[24] A. Kausaite, M. Dijk, J. Castrop, A. Ramanaviciene, J.P. Baltrus, J. Acaite, A. Ramanavicius, Int. Union Biochem. Mol. Biol 35 (2007) 57–63.

Biographies

Maryam Khodami received her B.Sc. degree in Electrical Engineering from Isfahan University of Technology, Iran and her M.Sc degree from University of Ottawa, Canada. She is currently working toward her PhD degree in the advanced research complex, University of Ottawa. Her research interests include optics and photonics, biophotonics, microwave and millimetre waves and periodic structure.

Pierre Berini received his Ph.D. and M.Sc.A. degrees in Electrical Engineering from École Polytechnique de Montréal, and his B.E.Sc. and B.Sc. degrees in Electrical Engineering and Computer Science, respectively, from the University of Western Ontario. Dr. Berini is a Professor of Electrical Engineering at the University of Ottawa and is the Founder and Chief Technology Officer of Spectalis Corp., a venture capital backed company commercializing surface plasmon devices. He is a Canada Foundation for Innovation researcher and has received an URSI Young Scientist Award (1999), a Premier of Ontario Research Excellence Award (2000), the University of Ottawa Young Researcher of the Year Award (2001), and an NSERC E. W. R. Steacie Memorial Fellowship (2008). Dr. Berini is a senior member of the IEEE and a member of the OSA. He is an Associate (Topical) Editor of Optics Express. He is the author or co-author of 17 patents (issued and pending), and of numerous publications in scientific journals and conference proceedings. His broad research interests include optics and photonics, electromagnetics, numerical methods, and the microfabrication of integrated optical structures. His research is currently focused on the area of plasmonics and related device applications including biosensors. Dr. Berini consults for industry, venture capital and grant councils.berini@eecs.uottawa.ca.

Chapter 4

Low detection limits using sandwich and inhibition assays on long range surface plasmon waveguide biosensors

4.1 Summary

Low detection limits using enhanced immunoassay formats is presented in this chapter. As described in Chapter 3, biomolecular interaction analysis (BIA) is used in assay developments and studying of antibody-antigen interactions. This includes sandwich and inhibition immunoassay format to improve the limit of detection of the platform down to pg/ml concentrations in solution. In the sandwich immunoassay format, a secondary antibody is introduced to enhance the binding response of the system. On the other hand, in the inhibition assay format a predetermined amount of the antibody is added to the solution bearing the antigen. As a result, antibody binding to the immobilized antigen on the sensor surface is competing with the antigen in solution resulting in lower response for higher antibody concentrations. A titration curve can be obtained in both cases which describes the output signal *vs.* antibody concentration. This curve could be used to determine the concentration of unknown samples. The experiments presented in this chapter shows that our optical biosensor based on LRSPP waveguides can detect molecular concentrations as low as 10 pg/ml in clean solutions, which is among the lowest reported in the literature.

4.2 Contribution

The results provided in this chapter are published in ***Sensors and Actuators B: Chemical***, Volume 273, 2018. Maryam Khodami designed the experiments and carried out the measurements. Maryam Khodami obtained the titration curves from the raw experimental data. Maryam Khodami interpreted the results and wrote the manuscript. Pierre Berini contributed to the interpretation of the results and revised the manuscript.

4.3 Article

The article follows here verbatim.

Sensors & Actuators: B. Chemical 273 (2018) 1156–1161

Contents lists available at ScienceDirect

Sensors and Actuators B: Chemical

journal homepage: www.elsevier.com/locate/snb

Low detection limits using sandwich and inhibition assays on long-range surface plasmon waveguide biosensors

Maryam Khodami[a,b], Pierre Berini[a,b,c,*]

[a] School of Electrical Engineering and Computer Science, University of Ottawa, 800 King Edward Ave., Ottawa, Ontario, K1N 6N5, Canada
[b] Centre for Research in Photonics, University of Ottawa, 25 Templeton Ave., Ottawa, Ontario K1N 6N5, Canada
[c] Department of Physics, University of Ottawa, 150 Louis Pasteur, Ottawa, Ontario K1N 6N5, Canada

ARTICLE INFO

Keywords:
Biosensors
LRSPP
SPR
BSA
Sandwich assay
Inhibition assay

ABSTRACT

A long-range surface plasmon polariton waveguide composed of a gold stripe embedded in CYTOP with an etched microfluidic channel has been used as a label-free real-time biosensor to demonstrate enhanced assay formats capable of very low detection limits. Specifically, sandwich and inhibition (competitive) assays were developed and demonstrated using Bovine Serum Albumin (BSA) and anti-BSA produced in rabbit as a model bio-specific pair. Carbodiimide coupling to a self-assembled COOH-terminated alkanethiol monolayer on the gold stripe was used to immobilize biomaterial to its surface. The optical output power from the biosensor was measured continuously over time and converted into surface mass density. Titration curves were extracted for both immunoassays. We demonstrate that protein concentrations in solution of 10 pg/ml can be detected with a signal-to-noise ratio of 20 using this new optical biosensor technology.

1. Introduction

Different immunoassay formats have been developed over time to improve the detection of biomolecules and proteins at low concentrations. Direct assays, sandwich assays and inhibition assays are the most frequently used immunoassay formats developed to date [1]. Biosensors, composed of a bio-recognition element and a physical transducer, exploit highly selective antibody-antigen binding for the detection of specific analytes in solutions. Based on the type of physical transducer, biosensor technologies can be divided into different types, *e.g.*, piezoelectric (quartz crystal micro balance) [2,3], electrochemical (potentiometric and amperometric) [4,5], and optical evanescent wave sensors such as surface plasmon resonance and fluorescence [6–9]. Among all of the technologies, surface plasmon resonance (SPR) has attracted a lot of attention as a sensitive label-free and real-time optical biosensor technology.

For example, using SPR technology, the direct detection of Bovine Serum Albumin (BSA) has been studied and a detection limit of 100 pM was reported [10]. In this study protein A film is fabricated on a self-assembled monolayer to realize the immune sensor. The detection of staphylococcal enterotoxin B (SEB) in milk to a detection limit of 5 ng/ml in a direct assay format, and to 0.5 ng/ml in a sandwich assay format in buffer and milk was reported in [11]. Cardiac troponin was detected using a sandwich assay to a detection limit of 25 μg/ml [12]. Domoic acid was detected using an inhibition (competitive) assay to a detection limit of 0.1 ng/ml [13]. Benzo[*a*]pyrene (BaP) detection has been reported in [14] and a detection limit of 50 pg/ml was achieved using an inhibition assay. The detection of pituitary hormones using an inhibition assay was reported in [15], where detection limits of 6 ng/ml for human growth hormone (hGh) in serum, and of 1 ng/ml for human follicle stimulating hormone (hFSH) and human luteinizing hormone (hLH) in urine were reported. The detection of BSA in milk using various immunoassay formats including sandwich and inhibition assay was reported in [16], where a detection limit of 1 ng/ml was achieved using an inhibition assay. Multi-analyte detection of environmentally relevant pesticides is performed by using a two-channelled SPR biosensor. Using inhibition immunoassay format a detection limit of 18 ng/ml for DDT, 50 ng/ml for chlorpyrifos and 52 ng/ml for carbaryl is reported [17]. Selective detection of methamphetamine was realized using inhibition assay format. The SPR sensor was capable of detecting concentrations in the range of 0.1–1000 ng/ml [18]. A chip-based digital SPR platform was used for BSA detection yielding a detection limit of 1 pg/ml [19]. So according to this (limited) subset of the literature on enhanced assays with SPR, detection limits in the broad range from 1 pg/ml to 25 μg/ml have been achieved, with a few ng/ml being typical. The detection limit depends on the target analyte, the sensing medium, the

* Corresponding author at: School of Electrical Engineering and Computer Science, University of Ottawa, 800 King Edward Ave., Ottawa, Ontario, K1N 6N5, Canada.
E-mail address: berini@eecs.uottawa.ca (P. Berini).

https://doi.org/10.1016/j.snb.2018.06.100
Received 5 February 2018; Received in revised form 2 June 2018; Accepted 23 June 2018
Available online 28 June 2018

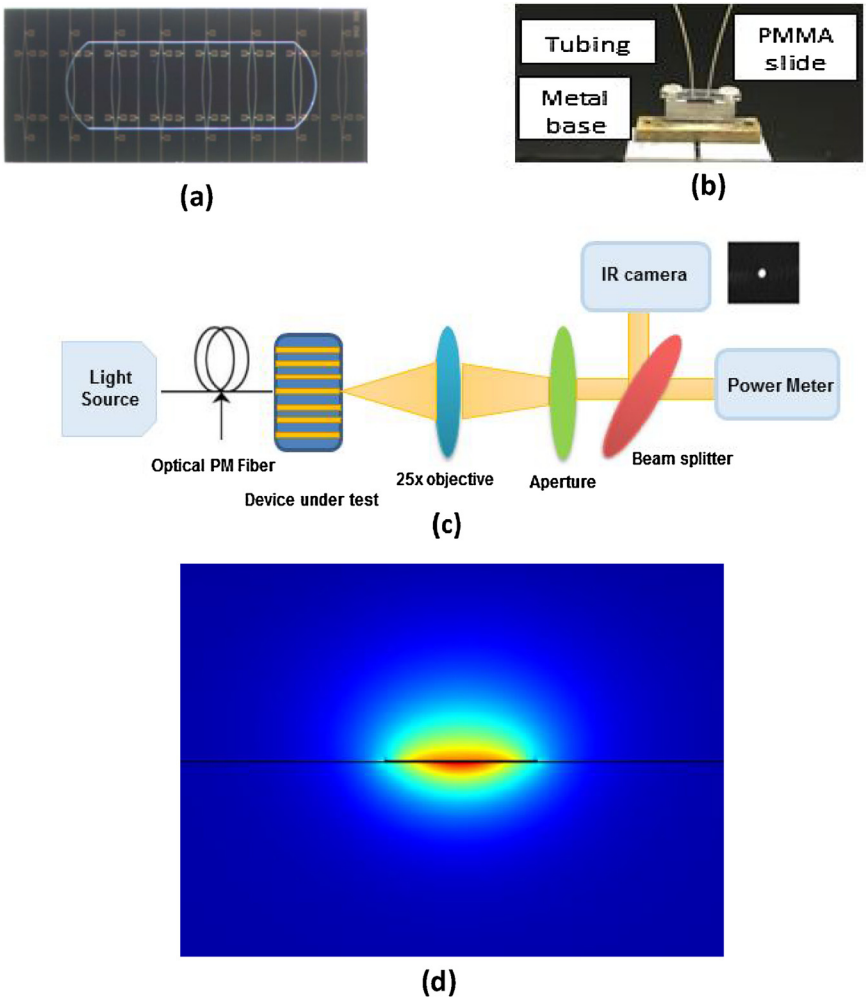

Fig. 1. (a) Microscope image of the sensor die with straight waveguides and other structures alternatively. (b) Custom made fluidic jig consisting of a PMMA cover slide, fluidic tubing and a metal base. (c) Optical setup used to measure the output power along with mode output image (d) Computed mode field distribution of the LRSPP waveguide.

interrogation apparatus and sensor chip, and the experimental conditions.

In this study, enhanced assay formats such as sandwich and inhibition assays are applied and demonstrated on novel long-range surface plasmon polariton (LRSPP) waveguide biosensors. For convenience, we demonstrate the assays using BSA and anti-BSA produced in rabbit as a model bio-specific pair, in buffer. LRSPP waveguide biosensors define a novel compact, low-cost and integrated biosensor technology for rapid, label-free and highly-sensitive detection of biomolecular interactions. LRSPPs are TM polarized optical surface waves that can propagate over an appreciable length and thus have a much longer interaction length with the sensing medium [20]. LRSPPs have been excited on metal slabs in prism-coupled systems, and used for the detection of *e.coli* bacteria [21], and for studying the effects of toxins on HEK-293 cells [22]. LRSPPs on metal stripe waveguides are also very sensitive; using a waveguide structure offers the additional advantages of compact and integrated biosensor geometries that can be arrayed. LRSPP waveguide biosensors have been used for the detection of Dengue infection in patient blood plasma [23,24], for bacteria detection in urine [25], and for the detection of leukemia markers in patient serum [26], all using a direct assay format. They have also been used for studying and extracting the binding kinetics of an immunological pair [27].

Here we demonstrate advanced assay formats, specifically, sandwich and inhibition assays that improve the limit of detection over direct assays on LRSPP waveguide biosensors using BSA and anti-BSA as a model system. The output optical power from straight gold waveguide biosensors is recorded continuously (over time) and the binding curves are obtained for anti-BSA/BSA interaction. The binding responses are then converted into surface mass concentration and used for the extraction of titration curves. The titration curves could subsequently be used to determine an unknown concentration of the analyte. The limit of detection obtained using both assays is better than 10 pg/ml, which is better than what is reported in most studies involving optical (including SPR) biosensors. This paper is organized as follows: First the materials and methods are discussed, then the results are presented for the sandwich and inhibition assay formats, and the paper is closed with concluding remarks.

2. Materials and methods

2.1. Chemicals and reagents

16-Mercaptohexadecanioc acid (16-MHA), phosphate buffered saline (PBS) 0.01 M, pH 7.4, bovine serum albumin (BSA), sodium dodecyl sulfate (SDS), 2- isopropanol alcohol (IPA), acetone HPLC grade ≥99.9, octane, glycerol (electrophoresis grade), N-Hydroxysuccinimide sodium salt (NHS), 1 - ethyl - 3 - (3 - dimethylaminopropyl) carbodiimide hydrochloride, ≥99% (EDC) and anti-BSA antibody produced in rabbit were obtained from Sigma-Aldrich. Distilled water was deionized

using Millipore filtering membranes (Millipore, Milli-Q water system at 16 MΩ cm).

The sensing buffer solution was prepared by mixing PBS and glycerol (PBS/Gly). In order to achieve high sensitivity, the refractive index of the buffer was chosen to be n = 1.338 at the wavelength of operation ($\lambda_0 \sim 1310$ nm) [28].

Different BSA concentrations (1 µg/mL, 100 ng/ml, 10 ng/ml, 1 ng/ml, 100 pg/ml and 10 pg/ml) were prepared by mixing lyophilized BSA with buffer. 50 µg/mL antibody concentrations were prepared by mixing powdered antibody with buffer.

2.2. Sensing device and instrumentation

The optical biosensor that is used in this work consists of gold stripes embedded in CYTOP with an etched microfluidic channel. The gold stripes are 5 µm wide, 35 nm thick and 3.8 mm in length. The fabrication details are described in [29] and consist of using a bilayer lift-off lithography process with evaporation to define the gold waveguides on the bottom CYTOP cladding. The top cladding is formed by spin-coating CYTOP, which is subsequently etched down to the gold surface to form microfluidic channels. A microscope image of a fabricated sensor chip is shown in Fig. 1(a). Light is butt-coupled to the input of the chip as described below, exciting LRSPPs that propagate along the length of the gold stripe.

The fluidic part of the setup consists of a fluidic jig and a syringe pump. A custom made fluidic jig, consists of a Plexiglas (PMMA) slide and a metal base designed to hold the device under test, as shown in Fig. 1(b). The fluidic tubing passes through holes that are drilled at each end of the PMMA slide. An O-Ring (Apple Rubber Product Inc.) seals around the etched channel. The metal base is machined to hold the device under test and is integrated into the optical interrogation setup. The syringe pump is used to inject the sensing solutions into a microfluidic channel. Fig. 1(c) shows a schematic of the setup used to capture the mode output of a straight gold waveguide along with a typical optical mode output image captured using the IR camera. The setup consists of a DFB laser operating at 1310 nm, a polarization-maintaining (PM) single-mode optical fiber, an objective, aperture, beam splitter, power sensor and infrared camera.

Fig. 1(d) shows the computed mode field distribution of the LRSPP at $\lambda_0 = 1310$ nm supported by a 5 µm wide 35 nm thick gold stripe ($\varepsilon_r = -86.08$ - j8.322), on Cytop (n = 1.3348) and covered by PBS/Gly buffer (n = 1.338), corresponding to the experimental situation of interest in this paper. The field is noted to peak along the metal surface (characteristic of surface plasmons) thus enabling high surface sensitivity biosensors. LRSPPs then propagate through the sensing channel and respond to changes in the bulk index of the sensing fluid or to the growth of an adlayer forming along the top surface of the stripe. In the present study, both effects are evident in the forthcoming sensorgrams, but are easily separated through careful application of the sensing protocol *via* the different timescales involved - bulk steps occur over much shorter timescales characteristic of the fluidic exchange time in the channel (*e.g.*, 60 s) compared to adlayer growth which is characteristic of binding kinetics (*e.g.*, 60 min).

The output power of the system is measured in dBm, then converted into W, and used in the following relation to determine the surface mass density of biomaterial accumulating on the waveguide surface [19]:

$$\Gamma(t) = \frac{1}{k}\left(\frac{n_a - n_c}{\partial n/\partial c}\left(\frac{P_{out}(t)}{P_{out}(t_b)} - 1\right)\right) \quad (1)$$

In the above, Γ is the surface mass density (pg/mm^2), k is analogous to parameter G and equal to 0.0318 nm^{-1} as described in [30], n_a and n_c are the refractive indices of the biomaterial accumulating on the surface and of the carrier fluid, 1.5 and 1.338, respectively [30], $\partial n/\partial c$ is the change in RI with analyte concentration and equal to 0.185 mm^3/mg [28], and $P_{out}(t_b)$ and $P_{out}(t)$ are the output powers (W) measured before and during analyte binding.

2.3. Device preparation

The cleaning process of an optical biosensor chip consists of consecutive steps to ensure clean facets enabling maximum optical coupling at the input and output of a chip, and to produce a clean gold sensing surface along the waveguide amenable to biomolecular attachment. Ultra-sonication in an octane bath is performed for 5 min as the first step to clean the sensor facets of dicing debris. In the second step, the dicing photoresist is removed using acetone. As the final step, the device is left in acetone for an extra 30 min to ensure the cleanliness of the waveguides and then thoroughly washed with IPA and DI water to remove any acetone residue. Any residual organic material is then removed from the sensing surface by placing the chip in a UV ozone chamber with the UV lamp on for 30 min followed by another 30 min with the lamp off. The biosensor chip is then stored for 24 h in a 1 mM solution of 16-MHA in IPA to form a self-assembled monolayer on the gold surface.

Regeneration of the biosensor surface down to the gold level was performed by exposure to UV-ozone after each experiment. Theoretically the regeneration process can be performed indefinitely in order to reuse the same device. Although in practice, the facet quality of our chips diminished after a few regeneration cycles, which caused more loss in the optical path and thus a weaker mode output.

3. Results and discussion

3.1. Sandwich assay

Fig. 2 shows a schematic representation of several immunoassay formats of interest, namely the direct assay, the sandwich assay, and the competitive (inhibition) assay. In general, the detection limit of a direct assay can be improved using the sandwich or inhibition assays. In a direct assay, antibodies are immobilized on the sensor surface, and binding curves are obtained as a solution containing analyte bearing antigen is injected over the immobilized antibodies. The surface mass density obtained from the binding curves is proportional to the concentration of analyte in solution. Although direct assays are easy to perform, the limit of detection is generally inadequate for detection at low concentrations.

Similarly to the direct assay, the first step in a sandwich assay involves the immobilization of antibodies on the sensor surface and the subsequent injection of analyte bearing antigen over the immobilized

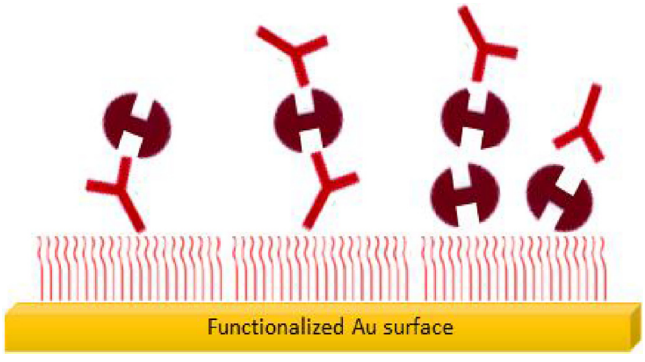

Fig. 2. From left to right: direct, sandwich, and inhibition (competitive) assay formats. The sensor surface is functionalized with a thiol-SAM, then exposure to EDC/NHS facilitates the covalent attachment of antibodies or protein to the SAM. In a direct assay, antigens react directly with immobilized antibodies. In a sandwich assay, a secondary antibody is added to the direct assay. In an inhibition assay, proteins bearing the antigen of interest are attached to the SAM, and the sensing solution containing unreacted antibodies is inject.

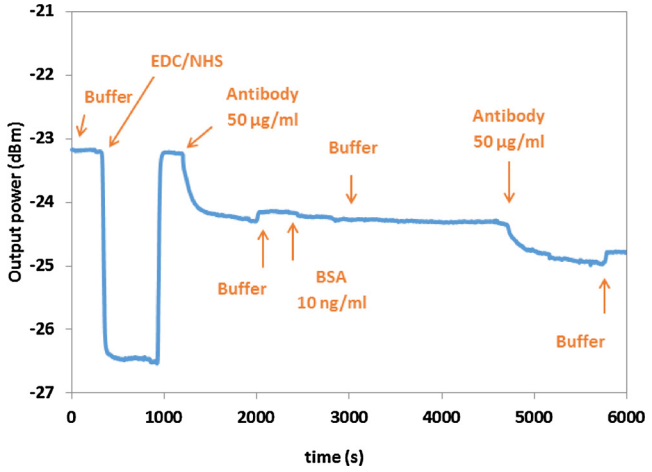

Fig. 3. Sensorgram of a complete experimental cycle for the sandwich assay, illustrating anti-BSA/BSA/anti-BSA interaction.

antibodies. Then, to enhance the response of the system, a secondary antibody that also binds to the analyte is injected over the captured analyte to obtain a secondary binding response. This secondary response is measured relative to the first binding response and used in the generation of calibration curves.

A full experimental cycle for the sandwich immunoassay format is shown in Fig. 3. A biosensor chip was initially incubated in a solution of 16-MHA in IPA in order to form a self-assembled monolayer (SAM) on the sensing surface. As a first step in the experimental cycle, an EDC/NHS solution in buffer is flowed over the sensor surface to activate the carboxylic groups (COOH) terminating the SAM layer. This step is followed by a buffer rinse. Subsequently, the immobilization of antibodies (anti-BSA) on the sensor surface is performed as the first step of the sandwich immunoassay. This step lasts for 20 min to allow the antibodies to react with the SAM, and is also followed by a buffer rinse. Next, BSA in buffer is injected over the immobilized antibodies for 10 min, followed by a buffer rinse. As the last step in the sandwich assay protocol, secondary antibodies (also anti-BSA) are injected and allowed to react with BSA for 20 min, followed by a buffer rinse to complete the experiment. In this example sensorgram, the BSA concentration used (10 ng/ml) is near the detection limit of the direct assay so its binding response is not evident, but a clear secondary anti-BSA response is observed as the second step in the sandwich assay. The experiments were performed at a constant flow rate of 20 µl/min, unless otherwise specified.

Fig. 4 presents the measured calibration curve obtained in the 10^{-6} to 1 µg/ml range of BSA concentration. The binding curve associated with the secondary antibody injection (measured optical output power in dBm) was converted to µW and normalized to the power level before the antibody injection (baseline level). The results were then converted to surface mass density using Eq. (1), following [27]. This procedure was repeated for different BSA concentrations. The inset to Fig. 4 shows the secondary antibody binding response to the BSA surface for different BSA concentrations, including the case 10 pg/ml. The surface mass response was then plotted *vs.* the logarithm of BSA concentration in solution. The maximum surface mass density (pg/mm^2) of each case was used to obtain the calibration curves. As can be seen in Fig. 4, detection down to 10 pg/ml of BSA in buffer has been achieved using this immunoassay format. The signal-to-noise ratio of the secondary binding curve in this case was 20 (inset) suggesting that even lower concentrations are detectable.

3.2. Inhibition assay

The inhibition assay is based on the addition of a predetermined concentration of antibody solution to analyte samples diluted to different concentrations. The first step in this assay is to immobilize analyte (BSA) on the sensor surface. Solutions of different BSA concentrations are then mixed with 50 µg/ml anti-BSA solution and injected over the immobilized BSA. The binding responses are proportional to the analyte (BSA) concentration since the concentration of the antibody is kept constant in all samples. Antibody binding to the immobilized BSA is inhibited by the BSA in solution, and thus increases as the concentration of BSA in solution decreases. Fig. 2 (right) gives a schematic of this assay format - the antibody in solution is partially available to bind with the immobilized analyte on the surface due to the presence of analyte in solution.

Fig. 5 shows the full experimental cycle for the inhibition assay format. The first step involves the activation of carboxylic groups terminating the SAM by injecting an EDC/NHS solution over the sensor surface. Then the analyte (BSA) is immobilized on the sensor surface. After a buffer rinse, a solution containing a mixture of BSA and anti-BSA is injected over the immobilized BSA. This step of the experimental cycle lasts for 20 min. and is followed by a buffer rinse. The optical response of the system is continuously recorded then converted to surface mass density, which is then used to extract the calibration curve.

The calibration curve is extracted over the 10^{-6} to 1 µg/ml range of BSA concentration. As described in the case of the sandwich assay, the binding curve associated with the BSA/anti-BSA solution injection (measured output optical power in dBm) is converted to µW and normalized to the power level before the antibody injection (baseline level). The results are then converted to surface mass density using Eq. (1), following [27]. This procedure was repeated for different BSA concentrations. The surface mass response was then plotted *vs.* the logarithm of BSA concentration in solution, as shown in Fig. 6. The lower left inset to Fig. 6 shows the anti-BSA binding to the BSA surface for different BSA concentrations in solution.

The maximum surface mass density (pg/mm^2) of each case was used to obtain the calibration curves. As can be seen in Fig. 6, the lowest BSA concentration detected is 10 pg/ml for the inhibition assay as well. Compared to the sandwich assay, the competitive assay does not show higher sensitivity, although the shorter experimental time (due to fewer steps) is an advantage.

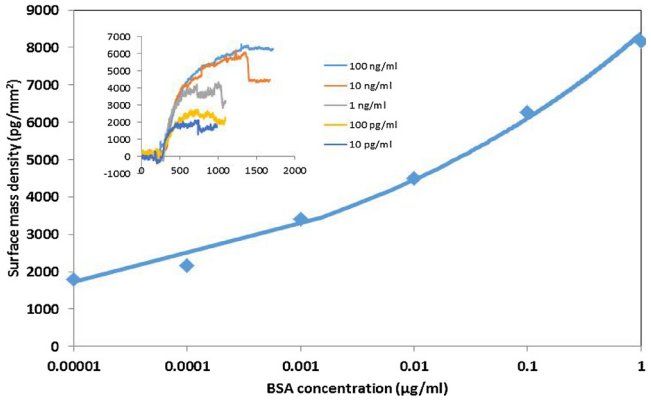

Fig. 4. Calibration curve for the sandwich assay in the concentration range of 10 pg/ml to 1 µg/ml of BSA in buffer. The inset shows the secondary antibody binding to the BSA surface for different BSA concentrations. (For interpretation of the references to colour in this figure legend, the reader is referred to the web version of this article).

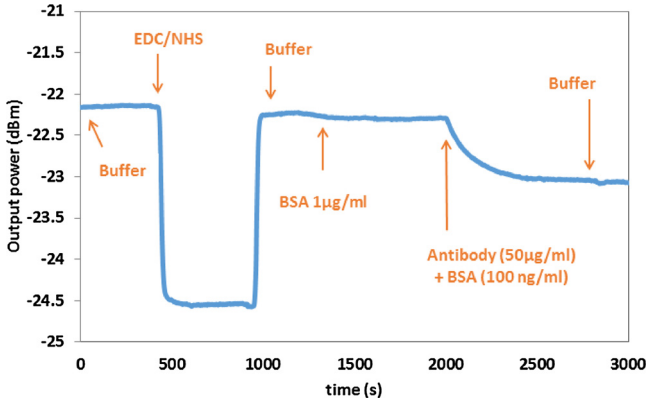

Fig. 5. Sensorgram of a complete experimental cycle for the inhibition assay, illustrating anti-BSA/BSA interaction.

A negative control was introduced into the experimental cycle to check the specificity of the binding interaction and examine the effect of non-specific binding on the results. For this purpose, a solution of 50 µg/ml cardiac troponin was injected after the BSA immobilization (first step). The interaction between the negative control and the BSA on the surface was observed to be minimal in comparison with the subsequent anti-BSA binding as shown in the top right inset of Fig. 6 - the red curve shows the surface mass concentration due to the negative control while the blue curve shows the surface mass concentration due to anti-BSA binding. So the surface mass density which is used to extract the calibration curves in both assay formats (sandwich and inhibition) is attributed to the specific anti-BSA/BSA interaction.

3.3. Kinetics analysis

Kinetics analysis for the interaction of the immobilized receptor and the soluble analyte, BSA and Anti-BSA in our case, can be performed using the method described in [27]. Using the linear least squares technique one can fit $d\Gamma/dt$ *vs.* Γ for each response. The slope value k_s is obtained from each plot, and plotted *vs.* analyte concentration C, for which the slope is equal to association rate constant k_a and the intercept value represents the dissociation constant k_d. Alternatively, one can fit the integrated rate equation to the measured responses to extra directly the constants of interest.

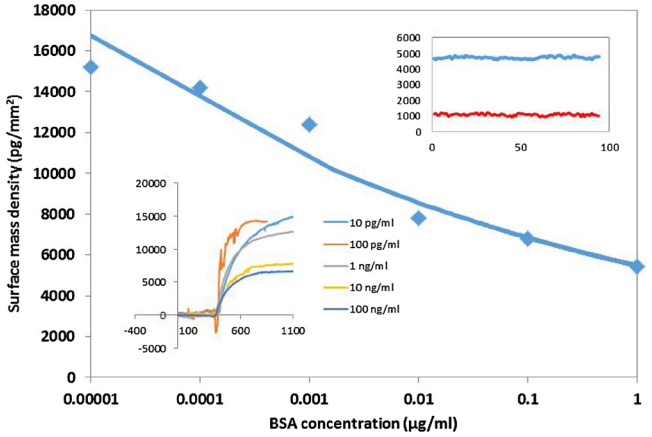

Fig. 6. Calibration curve for the inhibition assay in the concentration range of 10 pg/ml to 1 µg/ml of BSA in buffer. The top right inset shows the surface mass concentration comparison between the negative control cardiac troponin (in red) and anti-BSA (blue) in a competitive assay format. The lower left inset shows antibody plus antigen binding to the BSA surface for different BSA concentrations (For interpretation of the references to colour in this figure legend, the reader is referred to the web version of this article).

Kinetics constants were obtained for BSA interacting with Anti-BSA immobilized on the surface in the first step of the sandwich assay format. Using linear least square analysis, and considering the best fits among all BSA binding data sets, the association and disassociation rate constants k_a and k_d were found to be $21.6 \times 10^3\ M^{-1}s^{-1}$ and $32 \times 10^{-3}\ s^{-1}$.

Kinetics constants were also obtained for Anti-BSA interacting with immobilized BSA on the surface in the second step of the sandwich assay format. Since the concentration of BSA on the surface is changing, the non-linear least squares method was used to extract the association and disassociation rate constants by fitting directly the integrated rate equation to the responses. The integrated rate equation is described as:

$$\Gamma = \frac{k_a C \Gamma_{max}[1-e^{-(k_a C + k_d)t}]}{(k_a C + k_d)}$$

The average values obtained in this case for k_a and k_d are $32.9 \times 10^3\ M^{-1}s^{-1}$ and $0.62 \times 10^{-4}\ s^{-1}$, respectively. These values differ from those obtained in the first step of the sandwich assay but are still within the range for protein-protein interaction [27,31,32]. The difference may be due to the substantially more massive free partner in the second step (anti-BSA in buffer) compared to the first step (BSA in buffer).

4. Conclusion

In conclusion, we demonstrated enhanced assay formats consisting of the sandwich and inhibition assays using LRSPP waveguide biosensors. We obtained titration curves for these assays using BSA/Anti-BSA as a model biospecific pair. A limit of detection of 10 pg/ml was achieved for both assay formats. In the case of the sandwich assay, this detection limit was achieved with a signal-to-noise ratio of 20, suggesting that even lower concentrations are detectable. This is among the lowest detection limits reported in the literature for surface plasmon based biosensors. The kinetics constant are obtained for BSA interacting with Anti-BSA and *vice versa*, using linear and non-linear least square analysis. The constants are within the range for protein-protein interactions.

References

[1] J. Homola, Anal. Bioanal. Chem. 377 (3) (2003) 528–539.
[2] N. Miura, H. Higobashi, G. Sakai, A. Takeyasu, T. Uda, N. Yamazoe, Sens. Act B 13 (1–3) (1993) 188–191.
[3] B. Zhang, Q. Mao, X. Zhang, T. Jiang, M. Chen, F. Yu, W. Fu, Biosens. Bioelectron. 19 (7) (2004) 711–720.
[4] D. Tang, R. Yuan, Y. Chai, Y. Liu, J. Dai, X. Zhong, Anal. Bioanal. Chem. 381 (3) (2005) 674–680.
[5] F. Darain, S.U. Park, Y.B. Shim, Biosens. Bioelectron. 18 (5) (2003) 773–780.
[6] S. Kumbhat, K. Sharma, R. Gehlot, A. Solanki, V. Joshi, J. Pharm, Biomed. Anal. 52 (2) (2010) 255–259.
[7] J. Homola, Chem. Rev. 108 (2) (2008) 462–493.
[8] S.M. Borisov, O.S. Wolfbeis, Chem. Rev. 108 (2) (2008) 423–461.
[9] T. Ruckstuhl, M. Rankl, S. Seeger, Biosens. Bioelectr. 18 (2003) 1193–1199.
[10] W. Lee, D.B. Lee, B.K. Oh, W.H. Lee, J.W. Choi, Enzyme Microb. Technol. 35 (6) (2004) 678–682.
[11] J. Homola, et al., Int. J. Food Microb. 75 (1) (2002) 61–69.
[12] J. Wei, Y. Mu, D. Song, X. Fang, X. Liu, L. Bu, H. Zhang, G. Zhang, J. Ding, W. Wang, Q. Jin, G. Luo, Anal. Biochem. 321 (2) (2003) 209–216.
[13] Q. Yu, S. Chen, A.D. Taylor, J. Homola, B. Hock, S. Jiang, Sens. Act B 107 (1) (2005) 193–201.
[14] K.V. Gobi, C. Kataoka, N. Miura, Sens. Act B 108 (1) (2005) 784–790.
[15] J. Treviño, et al., Clin. Chim. Acta 403 (1) (2009) 56–62.
[16] H.E. Indyk, B.D. Gill, D.C. Woollard, Int. Dairy J. 47 (2015) 72–78.
[17] E. Mauriz, et al., Anal. Bioanal. Chem. 387 (4) (2007) 1449–1458.
[18] G. Sakai, et al., Electrochim. Acta 44 (21–22) (1999) 3849–3854.
[19] M. Pan, K.L. Lee, L. Wang, P.K. Wei, Biosens. Bioelectron. 91 (2017) 580–587.
[20] P. Berini, Long-range surface plasmon polaritons, Adv. Opt. Phot. 1 (3) (2009) 484–588.
[21] M. Vala, S. Etheridge, J. Roach, J. Homola, Sens. Act B 139 (1) (2009) 59–63.
[22] V. Chabot, Y. Miron, M. Grandbois, P.G. Charette, Sens. Act B 174 (2012) 94–101.
[23] W.R. Wong, O. Krupin, S.D. Sekaran, F.R.M. Adikan, P. Berini, Anal. Chem. 86 (3) (2014) 1735–1743.
[24] W.R. Wong, S.D. Sekaran, F.R.M. Adikan, P. Berini, Biosens. Bioelectron. 78 (2016) 132–139.
[25] P. Béland, O. Krupin, P. Berini, Biomed. Opt. Express 6 (8) (2015) 2908–2922.

[26] O. Krupin, P. Berini, Lab Chip 15 (21) (2015) 4156–4165.
[27] M. Khodami, P. Berini, Sens. Act B 243 (2017) 114–120.
[28] W.R. Wong, O. Krupin, F.R.M. Adikan, P. Berini, J. Lightwave Technol. 33 (15) (2015) 3234–3242.
[29] C. Chiu, E. Lisicka-Skrzek, R.N. Tait, P. Berini, J. Vac. Sci. Technol. B 28 (4) (2010) 729–735.
[30] J.A. De Feijter, J. Benjamins, F.A. Veer, Biopolymers 17 (1978) 1759–1772.
[31] R. Karlsson, A. Michaelsson, L. Mattsson, J. Immunol. Methods 145 (1991) 229–240.
[32] D.J. O'Shannessy, M. Brigham-Burke, K. Soneston, P. Hensley, I. Brooks, Anal. Biochem. 212 (1993) 457–468.

Maryam Khodami received her B.Sc. degree in Electrical Engineering from Isfahan University of Technology, Iran and her M.Sc degree from University of Ottawa, Canada. She is currently working toward her PhD degree in the advanced research complex, University of Ottawa. Her research interests include optics and photonics, biophotonics, and nano fabrication.

Pierre Berini received his pH.D. and M.Sc.A. degrees in Electrical Engineering from École Polytechnique de Montréal, and his B.E.Sc. and B.Sc. degrees in Electrical Engineering and Computer Science, respectively, from the University of Western Ontario. Dr. Berini is a Professor of Electrical Engineering at the University of Ottawa and is the Founder and Chief Technology Officer of Spectalis Corp., a venture capital backed company commercializing surface plasmon devices. He is a Canada Foundation for Innovation researcher and has received an URSI Young Scientist Award (1999), a Premier of Ontario Research Excellence Award (2000), the University of Ottawa Young Researcher of the Year Award (2001), and an NSERC E. W. R. Steacie Memorial Fellowship (2008). Dr. Berini is a senior member of the IEEE and a member of the OSA. He is an Associate (Topical) Editor of Optics Express. He is the author or co-author of 17 patents (issued and pending), and of numerous publications in scientific journals and conference proceedings. His broad research interests include optics and photonics, electromagnetics, numerical methods, and the microfabrication of integrated optical structures. His research is currently focused on the area of plasmonics and related device applications including biosensors. Dr. Berini consults for industry, venture capital and grant councils.berini@eecs.uottawa.ca

Chapter 5

Grating couplers for (Bloch) long range surface plasmons on metal stripe waveguides

5.1 Summary

The design and optimization of a (Bloch) LRSPP waveguide biosensor is presented in this chapter. Straight Au waveguides embedded in Cytop with an etched microfluidic channel were presented and characterized in previous chapters to extract the binding kinetics of protein-protein interaction and to demonstrate enhanced assay formats. LRSPPs were excited in this structure using the end-facet coupling technique, with coupling efficiencies of up to 90% as long as high-quality end facets are available. Although Cytop has a refractive index close to water, which makes it suitable for biosensing applications, it exhibits a low glass transition temperature that introduces limitations in fabrication processes. This problem could be addressed by replacing Cytop with a truncated 1D photonic crystal, supporting Bloch LRSPPs over a limited wavenumber and wavelength range. Motivated by the variable quality of end facets in general, grating couplers were optimized and used as input/output means to excite the Bloch LRSPP mode of the waveguide in this structure. Thus, gratings capable of in-coupling an incident Gaussian beam into (Bloch) LRSPPs are investigated using 2D FEM and 3D FDTD methods. Wide gratings on (non-)adiabatic flared stripes are designed to enable size matching and coupling to a larger incident beam. Calculations were carried out to determine the amount of reflected, transmitted and absorbed power by the

structure. A coupling efficiency of 25% at λ=1310 nm is predicted for the optimal grating design. Similar grating couplers previously reported in the literature suffer from significant losses due to the coupling of input light into multilayer slab modes, given the sub-optimal design of the coupler [61]. The optimal grating design on a flared stripe along with the original design on a straight waveguide are fabricated using photolithography and electron beam lithography techniques and measured using an optical setup to verify the design concepts. An 8-10 dB improvement in the output power of the structure is observed for the optimal design. A coupling efficiency of 16% is obtained from the measurement, which is lower that the predicted values. This is due to the mismatch between the size of the input beam and the grating coupler. This problem could be addressed using a tapered or lensed fiber.

5.2 Contribution

The results provided in this chapter are published in the ***Journal of Optical Society of America B***, Volume 36, Issue 7, 2019. Maryam Khodami modeled and optimized the waveguide and grating coupler structures by carrying out FEM and FDTD calculations. Pierre Berini designed the multilayer stack and calculated the dispersion diagram, the detail of which can be found elsewhere [68]. Maryam Khodami fabricated the device and measured the wavelength response of the structure. Maryam Khodami interpreted the results and wrote the manuscript. Pierre Berini contributed to the interpretation of the results and revised the manuscript.

5.3 Article

The article follows here verbatim.

Research Article Vol. 36, No. 7 / July 2019 / Journal of the Optical Society of America B 1921

Journal of the Optical Society of America B

OPTICAL PHYSICS

Grating couplers for (Bloch) long-range surface plasmons on metal stripe waveguides

MARYAM KHODAMI[1,2] AND PIERRE BERINI[1,2,3,*]

[1]School of Electrical Engineering and Computer Science, University of Ottawa, 800 King Edward Ave., Ottawa, Ontario K1N6N5, Canada
[2]Center for Research in Photonics, University of Ottawa, 25 Templeton Street, Ottawa, Ontario K1N6N5, Canada
[3]Department of Physics, University of Ottawa, 150 Louis Pasteur, Ottawa, Ontario K1N6N5, Canada
*Corresponding author: berini@eecs.uottawa.ca

Received 27 March 2019; revised 23 May 2019; accepted 28 May 2019; posted 31 May 2019 (Doc. ID 363400); published 21 June 2019

Gratings capable of incoupling an incident Gaussian beam into long-range surface plasmon polaritons (LRSPPs), propagating along a thin narrow Au stripe on a low-index cladding (fluoropolymer), or on a truncated 1D photonic crystal as a Bloch LRSPP, are investigated for potential biosensing application. The gratings are optimized, initially, through 2D modeling using the vectorial finite element method. Different 3D grating designs are then investigated through 3D modeling using the vectorial finite difference time domain method, including wide gratings on adiabatic and nonadiabatic flared stripes. Wide gratings on flared stripes have a larger area enabling size matching and coupling to larger incident beams, which facilitates optical alignments. We also investigate the effects of changing the size of the beam incident on the structures. Incoupling efficiencies of up to 25% at $\lambda_0 = 1310$ are predicted for optimal gratings—such coupling efficiencies are among the highest reported to date for a structure of this kind. Similar grating designs are also examined as outcoupling structures, capable of coupling (Bloch) LRSPPs into a perpendicularly emerging Gaussian beam. The absorptance, reflectance, and transmittance of the structure were also calculated. Structures were fabricated on a multilayer wafer supporting Bloch LRSPPs to verify design concepts.

https://doi.org/10.1364/JOSAB.36.001921

1. INTRODUCTION

Surface plasmon polaritons (SPPs) are TM-guided optical waves propagating along a metal–dielectric interface. SPPs attract significant attention due to their unique properties and their potential applications, including to biosensing [1,2]. The use of SPPs in biosensing is widely studied, especially in prism-coupled configurations [3,4]. In this technique, the Kretschmann–Raether geometry is primarily employed to satisfy the excitation condition of SPPs at the metal–solution interface by an incident optical beam. Metal gratings to excite SPPs along a metal–dielectric interface have also been investigated in the literature [5–9]. For example, a coupler on a Ag-SiO_2 interface was projected to yield a 50% coupling efficiency for an incident Gaussian beam to SPPs [5]. A 58.4% coupling efficiency was reported for a multigrooved structure, fabricated using focused ion beam (FIB) milling on a 450 nm thick Au film on glass [8]. Slanted groove gratings were also investigated, and improved coupling efficiencies of up to 68% were demonstrated for a Ag-SiO_2 interface [9].

The application of SPPs is limited by their high propagation loss due to the absorption of light in the metal; so consequently, they have a short propagation length. Alternatively, bounding a thin metal film on all sides by the same dielectric reduces the loss, because such structures support so-called long-range SPPs (LRSPPs) [10]. LRSPPs are supermodes that arise from the coupling of SPPs at the metal–dielectric interfaces to form a coupled mode. The longer propagation length of LRSPPs yields advantages in sensitivity compared to SPPs because a longer optical interaction length with the sensing medium is possible [11]. End-fire coupling [12], prism coupling [13,14], and coupling at broadside using an optical fiber [15,16] can be used to excite LRSPPs from fiber modes or free space beams.

In LRSPP waveguide biosensors the metal stripe is covered by an aqueous solution within a microfluidic channel, so the lower cladding must have a refractive index close to the sensing solution, motivating the use of low-index fluoropolymers such as CYTOP or Teflon [17,18]. These materials mimic the behavior of a homogenous background medium by ensuring that the bottom cladding and the sensing solution on top have a similar refractive index, thereby enabling the propagation of LRSPPs. The use of LRSPP waveguides excited via end-fire coupling in biosensing applications has already been studied in the literature [19–22]. Coupling efficiencies greater than 90% can be achieved in this scheme as long as the end facets are of high quality, which is not typically trivial to achieve. Prism coupling is an alternative [13,14], and although straightforward, the prism adds bulk and is incompatible with integration and miniaturization.

Comparatively less work has been done on grating couplers to excite LRSPPs on waveguides [23–25].

Although Cytop has a refractive index suitable for biosensing (i.e., close to water), its use introduces limitations in fabrication processes due to its low glass transition temperature and the fact that the material remains vulnerable to its solvent post curing [17]. A truncated 1D photonic crystal (1DPC) can replace a low-index polymer cladding to support Bloch LRSPPs within the bandgap of the 1DPC over prescribed ranges of wavenumber and wavelength [26–28]. Similar sensitivities to LRSPPs in the corresponding fluoropolymer/solution system are expected with Bloch LRSPPs because the main modal characteristics are retained (attenuation, wavenumber, and mode size) [28,29]. A rudimentary grating coupler was used in Ref. [29] to successfully excite Bloch LRSPPs, but a significant portion of the input light was diffracted into multilayer slab modes given the suboptimal design of the coupler.

Motivated by quality issues with end facets and the bulkiness of prism coupling, we seek to optimize gratings for use in a broadside coupling scheme where a Gaussian beam excites LRSPPs on a Au stripe on a fluoropolymer, or Bloch LRSPPs on a Au stripe on a truncated 1DPC. Adiabatic and nonadiabatic flared stripes accommodating wide gratings size-matched to an incident Gaussian beam and to the LRSPP are investigated. Such structures maximize the coupling efficiency to LRSPPs, minimize coupling to slab modes, and ease alignment tolerances. Given their compatibility with planar technology, grating couplers could be integrated into arrays of biosensors enabling multichannel biosensing [30].

We explore the design space of grating couplers by optimizing their structural parameters such as height, duty cycle, and pitch. Initially, optimization is carried out on a 2D cross-sectional model of the structure (for expediency), followed by full modeling in 3D of some preferred designs. Flared stripe widths and the effects of changing the excitation beam size are studied via the 3D model. We focus on maximizing the coupling efficiency into LRSPPs while minimizing forward-propagating background light (coupling to slab modes). Gratings for outcoupling LRSPPs into broadside radiation are also studied.

2. CONCEPTS

Longitudinal cross-sectional sketches of the two structures of interest are given in Fig. 1. We are interested in the operation of these structures at free-space operating wavelengths near $\lambda_0 = 1310$ nm. The structure of Fig. 1(a) comprises a 35 nm thick, 5 μm wide Au stripe ($\varepsilon_r = -86.8 - j8.322$ [23]), with a grating coupler consisting of rectangular Au ridges, each of height H and width W, arranged in a period of Λ. The top and bottom claddings are assumed to be a fluoropolymer (Cytop, $\varepsilon_r = 1.3348$ [17]), each of the same thickness of 10 μm. The structure is supported by a silicon wafer ($\varepsilon_r = 3.5029$). The waveguide supports the propagation of LRSPPs along the length of the Au stripe, as sketched.

The other structure investigated in this study is shown in Fig. 1(b) and comprises the same Au stripe incorporating the same grating ridges, but on a truncated 1DPC covered by Cytop. The 1DPC can be used as the lower cladding below a thin metal film to mimic the properties of the dielectric

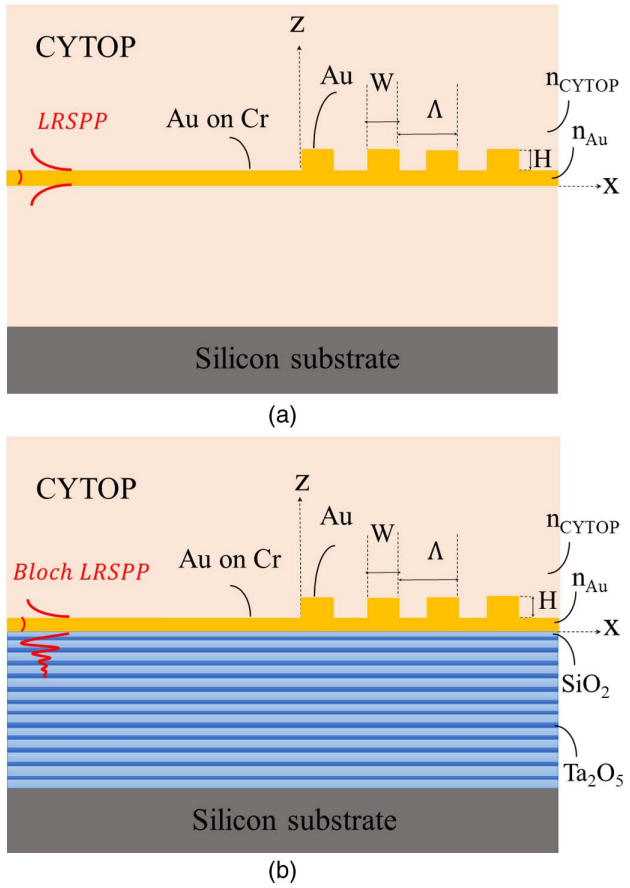

Fig. 1. Longitudinal cross-sectional views of the structures investigated. (a) LRSPP (sketched in red) on a Au stripe with a grating coupler embedded in a fluoropolymer (Cytop). (b) Bloch LRSPP (sketched in red) on a Au stripe with a grating coupler on a truncated 1DPC (SiO_2/Ta_2O_5) with a fluoropolymer upper cladding (Cytop).

medium on the other side [28]. The structure supports Bloch LRSPPs, which propagate in the plane of the 1DPC, along the Au stripe and dielectric medium. For a 1DPC similar to the one shown in Fig. 1(b), optical modes have the transverse form of

$$U(z) = p_K(z)e^{-jKz}, \tag{1}$$

where U is any of the mode field components, K is the Bloch wavenumber, and p_K is a periodic function of the same periodicity as the crystal [31]. The design of the truncated 1DPC should be selected such that the Bloch LRSPP supported by the structure [Fig. 1(b)] has similar modal properties as the LRSPP supported in the corresponding fluoropolymer structure [Fig. 1(a)], including similar wavenumbers at $\lambda_0 = 1310$ nm such that a good grating coupler design for the fluoropolymer structure [Fig. 1(a)] can be transferred to the 1DPC [Fig. 1(b)] yielding a similar coupling efficiency.

Following [28,29], our 1DPC design consists of 12 periods of alternating layers of SiO_2/Ta_2O_5 of thickness $d_{SiO_2} = 625$ nm ($n_{SiO_2} = 1.447$) and $d_{Ta_2O_5} = 209$ nm ($n_{Ta_2O_5} = 2.069$). The dispersion curves of the corresponding semi-infinite stack under TM plane wave excitation are plotted in Fig. 2(a)

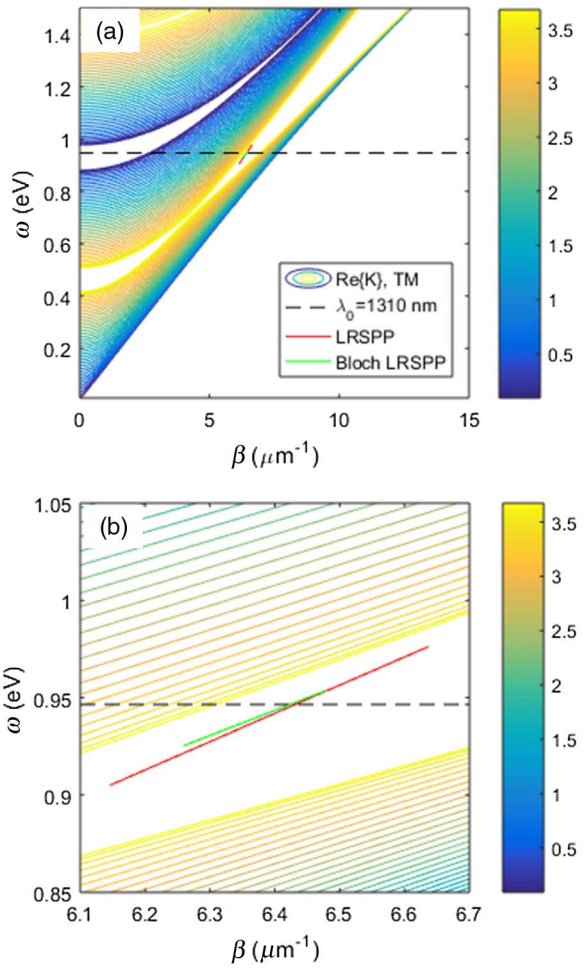

Fig. 2. (a) Dispersion curves of the corresponding semi-infinite truncated 1DPC under TM plane wave excitation. $\lambda_0 = 1310$ nm is marked as the horizontal dashed line, the dispersion curve of the LRSPP in the fluoropolymer structure is plotted in red, and the dispersion curve of the Bloch LRSPP on the 1DPC is plotted in green. K is the Bloch wavenumber, and β is the in-plane wavenumber. (b) Zoom in the region of the (Bloch) LRSPP.

(neglecting material dispersion). The curves reveal two bandgaps of relevance to operation at $\lambda_0 = 1310$ nm: the Bloch LRSPP will propagate in-plane within the first bandgap, and the second bandgap will reflect light at normal incidence. A final layer of SiO_2 ($d_{cap} = 462$ nm) then covers the stack to achieve wavenumber matching, and a 10 μm thick Cytop upper cladding is assumed. The wavenumber of the Bloch LRSPP is then the same as that of the LRSPP in the corresponding fluoropolymer structure [Fig. 1(a)]. Figure 2(b) shows the first bandgap in expanded view, with the dispersion curve of the LRSPP in the fluoropolymer structure and the dispersion curve of the Bloch LRSPP on the 1DPC, computed using modal analysis. Both wavenumbers are similar at $\lambda_0 = 1310$ nm and well within the bandgap as expected [28,29].

A perpendicularly incident *p*-polarized Gaussian beam of waist radius 2 or 4 μm is launched from a source plane 10 μm above the grating ridges and is incident on the grating at a 8 μm offset from the center to launch LRSPPs preferentially in the $-x$ direction. Multiple steps are taken to alter the grating design to maximize the coupling into the LRSPP mode. Starting from the grating equation, the pitch Λ must satisfy

$$\Lambda = m\lambda_0/(n_{\text{eff},a} - n_1 \sin\theta), \tag{2}$$

where m is an integer representing the grating order, $n_{\text{eff},a}$ is the average effective index of the mode to be excited, n_1 is the refractive index of the bounding medium (Cytop in this case), and θ is the angle of incidence. From this equation, it is evident that the coupling angle θ changes with the wavelength. Thus we consider $\theta = 0°$ (broadside excitation) and $m = 1$ for the lowest grating order. In this case, the grating equation simplifies to

$$\Lambda = \lambda_0/n_{\text{eff},a}. \tag{3}$$

3. SIMULATION RESULTS AND DISCUSSION

A. 2D Modeling Using the FEM Method

The vectorial finite element method (FEM) was used to model a longitudinal 2D cross section of the fluoropolymer-cladded structure at the free-space wavelength of 1310 nm and to optimize the grating design to maximize the coupling efficiency.

The initial grating design, adopted from [29], incorporates 16 ridges, 150 nm in height, and is arranged in a 1 μm pitch. The geometrical parameters of the grating consisting of the ridge width, height, and pitch were altered, and the power transmitted by the LRSPP was calculated 200 μm away from the grating plane to ensure that spatially transient fields have decayed sufficiently to be negligible (cf. also Fig. 5, below). In addition, the effects of adding a Au pedestal under the grating were explored.

The simulation domain was set to 220 μm × 20 μm, and the boundaries terminated using perfectly matched layers (PMLs). The mesh was set to 5 nm inside the metal regions and 75 nm everywhere else. The Gaussian beam launched 10 μm above the grating plane had a beam width of 4 μm. The simulations were carried out on the Frontenac cluster provided by the center for advanced computing at Queen's University (CPU model Xenon-E7-4860, 256 GB of memory). Depending on the number of degrees of freedom, a simulation can take up to 5 h or more to be completed. The distribution of the calculated $|E_z|$ field over the longitudinal 2D cross section is shown in Fig. 3 for an example grating structure embedded in fluoropolymer and on the 1DPC. As shown in this figure, the transient fields are strong close to the grating [Fig. 3(a)], but they decay rapidly such that the LRSPP field distribution is revealed away from the grating [Fig. 3(b)].

The effects of varying the grating pitch, ridge, width (duty cycle), ridge height, and the pedestal height under the grating, as well as the nonverticality of the grating side walls on the normalized transmitted power, were determined. The wavelength response of the grating coupler was also obtained over a wavelength range near 1300 nm.

The normalized transmitted power was computed as the total power flowing in the $-x$ direction, normalized to the source power, at a distance far enough from the grating to ensure that it was dominated by the LRSPP (no spatial transients). A vertical line spanning the height of the computational domain was used, along which a line integral of the x component

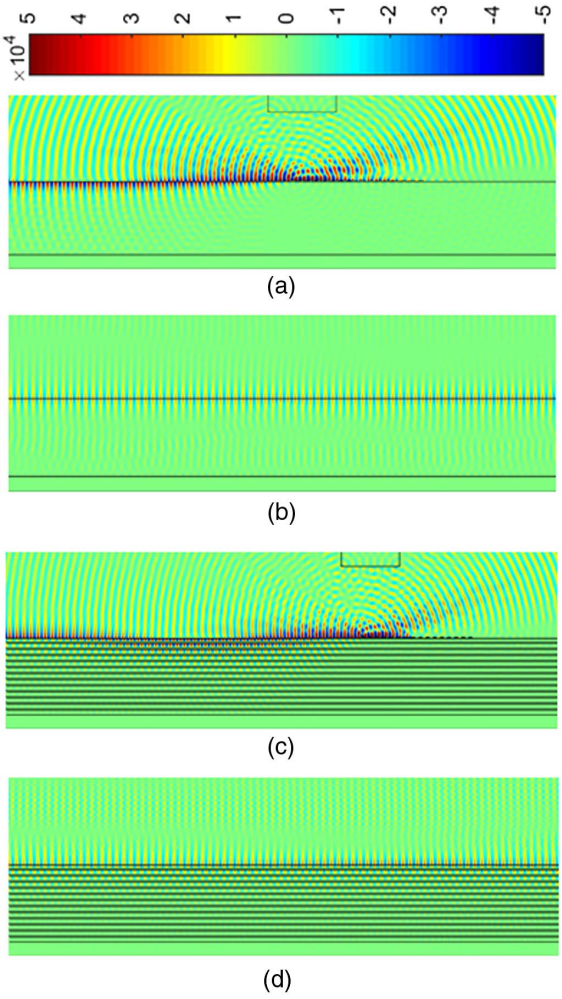

Fig. 3. Distribution of $|E_z|$ computed using the FEM over the longitudinal 2D cross section of the structure. The structure of interest comprises a Au stripe with grating ridges embedded in fluoropolymer [Fig. 1(a)] and on a 1DPC [Fig. 1(c)]. Field distribution (a, c) close to the grating, and (b, d) far from the grating.

of the real part of the Poynting vector was taken. The range for each parameter was selected as follows: $\Lambda = [900:10:1070]$, $W = [300:10:480]$, $H = [100:10:200]$ and pedestal height $= [10:10:80]$ nm (where [min: step: max] is implied). In each case all other parameters were kept constant, and the cycle repeated until convergence to an optimal design was acquired.

From Fig. 4 it is evident that the maximum normalized transmitted power is obtained for a grating design having $W = 380$ nm, $H = 160$ nm, $\Lambda = 980$ nm on a pedestal 20 nm in height.

A clear peak is observed in each simulation case, which corresponds naturally to the behavior of the grating, and in the case of Fig. 4(a) to its wavelength selectivity in response to the input Gaussian beam. It has also been confirmed that changing the number of metal ridges from 11 to 16 does not impact the coupling efficiency because the beam size remains fixed and smaller than the grating. Performing optimization cycles for the case involving the 1DPC [Fig. 1(b)] is computationally very demanding (even in 2D), but fortunately the Bloch LRSPP thereon shares the same modal characteristics as the LRSPP in the fluoropolymer, so the optimal design is similar (following the discussion in the theory section). The coupling efficiency calculated in both cases was indeed found to be essentially the same, confirming that the designs are transferable.

The effect of the nonverticality of the grating ridge side walls was studied by varying the parameter $b = [0:10:190]$ nm where $b = 0$ represents rectangular ridges and $b = 190$ nm represents triangular ridges (for $W = 380$ nm). As can be seen in Fig. 4(e), the transmitted power drops dramatically for $b > 50$ nm, which corresponds to 20° tilted ridge walls.

The wavelength response, over the range $\lambda_0 = [1280:5:1370]$ nm, of a grating coupler is given in Fig. 4(f) for coupling into Bloch LRSPPs on the 1DPC. As can be seen, the wavelength response is maximal at 1305 nm and has a FWHM of ~40 nm.

The coupling efficiency is the fraction of power that couples from the incident Gaussian beam to the LRSPP mode of the waveguide, and it can be computed using the method described in Ref. [23]. Following [23], the distribution of power along the x direction can be written as

$$P_x(x) = P_{x,0}e^{2\alpha(x-x_0)} + P_{x,r}(x), \tag{4}$$

where $P_{x,0}$ is the power carried by the LRSPP at the location of the grating, α is the field attenuation constant of the LRSPP, $P_{x,r}$ is the power carried by all other modes except the LRSPP in the $-x$ direction, which rapidly decays to zero as the distance from the grating increases due to radiation and absorption losses. This leads to the dominant term far from the grating:

$$P_x(x) \approx P_{x,0}e^{2\alpha(x-x_0)}. \tag{5}$$

The complex effective index of the LRSPP mode can be obtained from modal analysis. Using the imaginary part of the effective index, α can be calculated and inserted into Eq. (5) to obtain $P_{x,0}$. The coupling efficiency can then be obtained by normalizing $P_{x,0}$ to the input power. The input power was set to 0.5 W, and as a result, $P_{x,0}$ is divided by 0.5 when calculating the coupling efficiency from Eq. (5). Following this approach, 25% coupling efficiency is expected for our optimal grating design ($W = 380$ nm, $\Lambda = 980$ nm, $H = 160$ nm on a pedestal of height 20 nm) at $\lambda_0 = 1310$, which is among the highest reported to date for a coupler of this kind. By comparison, a coupling efficiency close to 100% is achievable using a prism in an attenuated total reflection (ATR) geometry, and about 87% using a conformal grating and a non-normal angle of incidence [32]. The high coupling efficiency observed in this case was achieved by using a weak conformal grating with a sinusoidal profile and a beam incident at an optimized (non-normal) angle.

The effect of changing the angle of incidence was studied over the range of $\theta = [0:2:10]$ degrees. We determined that the coupling efficiency improves slightly for $\theta = 2°$, and then drops as the angle of incidence increases. This is unsurprising as the grating was optimized for normal incidence.

Figure 5 shows the distribution of the electric field along the z direction as a function of distance from the left edge of the grating for the structure embedded in fluoropolymer and on a 1DPC. It is evident from these plots that the E_z field cut

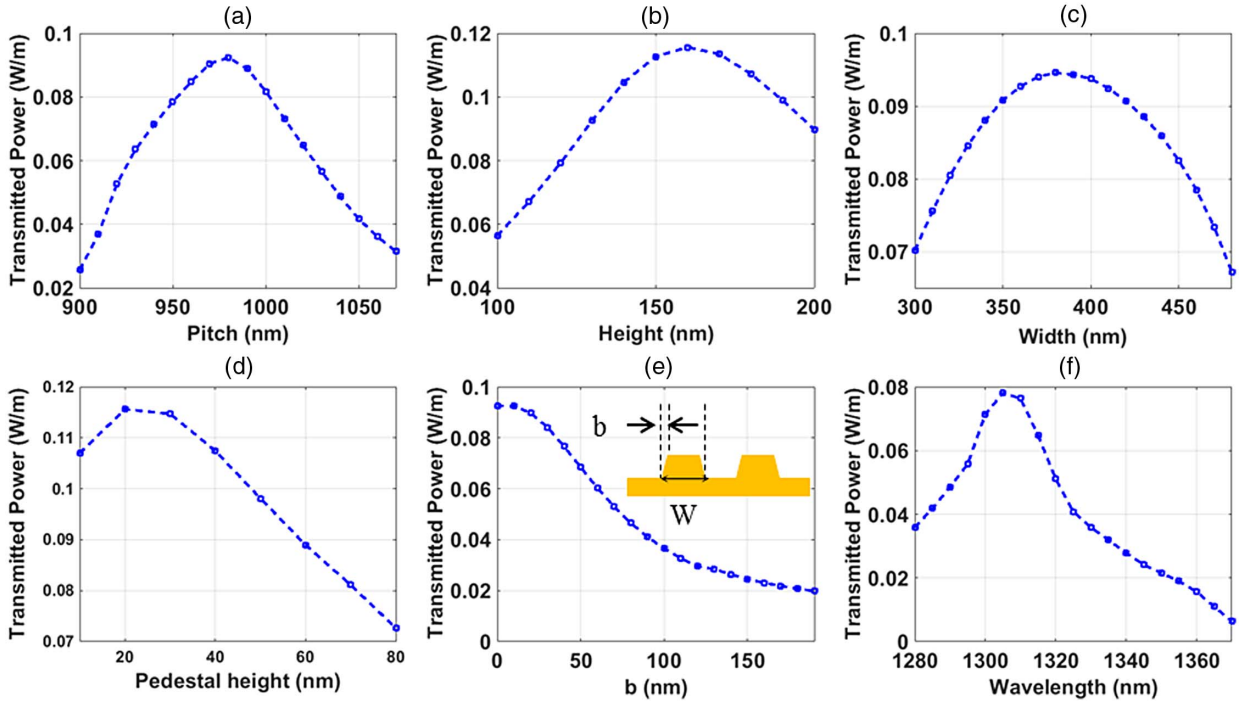

Fig. 4. Transmitted normalized power into the LRSPP for a grating structure embedded in fluoropolymer as a function of (a) pitch Λ ($W = 380$ nm, $H = 150$ nm), (b) height H of the grating ridges ($W = 380$ nm, $\Lambda = 980$ nm), (c) width W of the grating ridges ($H = 150$ nm, $\Lambda = 980$ nm), and (d) pedestal height ($W = 380$ nm, $H = 160$ nm, $\Lambda = 980$ nm). (e) Effect of the nonverticality of the grating ridge walls ($W = 380$ nm, $H = 150$ nm, $\Lambda = 980$ nm). (f) Wavelength response of a grating coupler into Bloch LRSPPs on the 1DPC ($W = 380$ nm, $H = 160$ nm, $\Lambda = 980$ nm).

evolves into an unvarying smooth distribution recognized as that of the LRSPP about 200 μm away from the grating. The field profile is distorted close to the grating region due to spatial transients. This confirms that 200 μm is a sufficient distance to sample the transmitted power from which the coupling efficiency to the LRSPP can be extracted and the grating design optimized.

While the grating coupler is capable of coupling light from an incident *p*-polarized Gaussian beam to the (Bloch) LRSPP mode of the waveguide, it is also capable of coupling the (Bloch) LRSPP mode propagating along the waveguide to output *p*-polarized light having a profile similar to a Gaussian beam.

The output characteristics of grating couplers were also investigated using our 2D FEM model. The absorbed, reflected, transmitted, and outcoupled powers from a grating, relative to incident LRSPPs, were calculated by modeling a complete structure using a large simulation domain that includes input and output couplers separated by 400 μm. The longitudinal cross-sectional distribution of $|\mathbf{E}|$ near the output grating is plotted in Fig. 6. As is evident from this result, LRSPPs are partially backreflected into the $-x$ direction due to the presence of the grating, forming a standing wave pattern in the $|\mathbf{E}|$ field distribution for $x < 0$. This reflection could be reduced by apodizing the grating strength along its length, which could also improve the quality of the output beam.

A line integral of the z component of the real part of the Poynting vector was obtained along a horizontal line placed 9.5 μm above the output grating to calculate the output coupling efficiency, relative to the LRSPP incident on the grating. The output coupling efficiency obtained was ~20%. This coupling efficiency could be achieved in practice using, e.g., a large-area power sensor or a large-core multimode optical fiber connected to a power sensor, placed near the edge of the grating. The outcoupling efficiency was verified by computing $P_{\text{out}}/P_{\text{in}} = C_1 C_2 e^{2\alpha L}$ of the full structure, where P_{in} and P_{out} are the input and output powers calculated using horizontal monitors at the input and output gratings, C_1 and C_2 are the input and output grating coupling efficiencies, respectively, and L is the distance between the edges of the input and output gratings.

The absorptance of the gratings was calculated by accounting for the net power passing through a bounding box with power monitors placed around the output grating and imposing the conservation of power. Specifically, a computational domain was defined to isolate the incoming and outgoing powers using vertical and horizontal cut-lines along which line integrals of the x and z components of the real part of the Poynting vector were computed. In this manner, the absorbed power P_A could be extracted and divided by the LRSPP power input into the system to extract the absorptance. A grating absorptance of ~15% was determined.

The reflection coefficient of the LRSPP incident onto the output grating was calculated using the distribution of the magnitude of the electric field extracted from a horizontal line placed at $z = 30$ nm above the metal stripe. The voltage standing wave ratio (VSWR) can be extracted from the maximum and minimum values of the electric field as $\text{VSWR} = E_{\max}/E_{\min}$. The magnitude of the reflection coefficient is

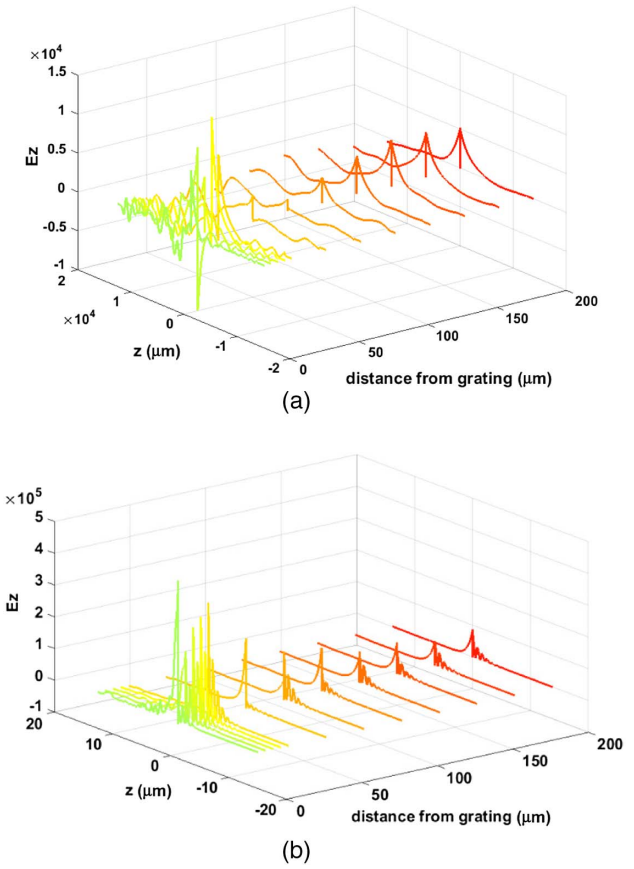

Fig. 5. Distribution of the electric field component E_z along z as a function of distance away from the grating for (a) the LRSPP on the embedded in fluoropolymer and (b) the Bloch LRSPP on the 1DPC structure.

$$|\Gamma_L| = \frac{\text{VSWR} - 1}{\text{VSWR} + 1}. \tag{6}$$

This value is then corrected by accounting for the propagation loss between the field observation point and the distance to the output grating edge L_0 : $\Gamma_0 = \Gamma_L / e^{-2\alpha L_0}$. It should be noted that the input power calculation is performed far away from the input and output gratings ($L_0 = 200$ μm away from each), where the spatial transients due to diffraction from the gratings are minimal. E_z has a smooth and unvarying profile at this location. Using the zoom shown as inset in Fig. 6(b), Γ_0 was calculated at the location of the grating, yielding 7%. The corresponding LRSPP mode power reflection coefficient is 0.5%.

The LRSPP power transmitted through the output grating was calculated 200 μm away from the output grating where a smooth and unvarying field distribution is observed. Using Eq. (5), the transmittance was found to be 31%.

B. 3D Modeling Using the FDTD Method

The full 3D model of the structures under investigation, along with their top views, are shown in Fig. 7. The full structure consists of a nonadiabatic or adiabatic flared stripe constructed from oppositely curved sections of radius R, bearing 16 Au ridges that form the grating. The nonadiabatic flared stripe

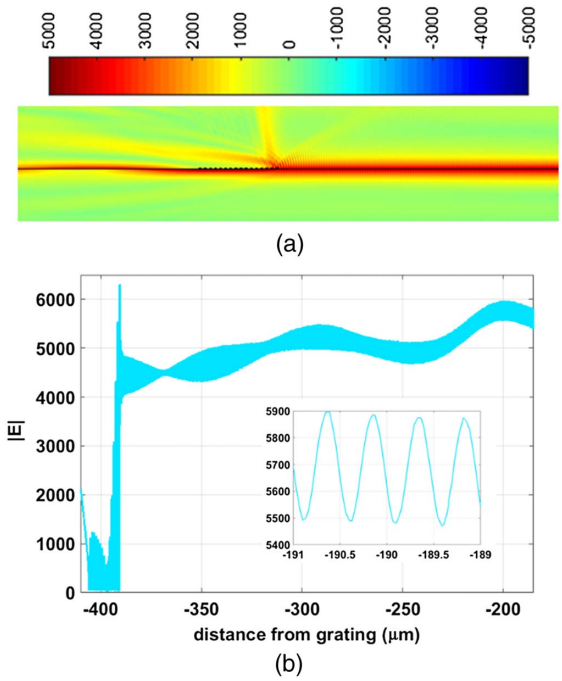

Fig. 6. (a) Distribution of the electric field magnitude |**E**| along x as a function of distance away from the output grating, for a domain that is extended from −500 to −200 μm. (b) Distribution of |**E**| along x at $z = 30$ nm. The region $x \sim -190$ μm is shown as the inset.

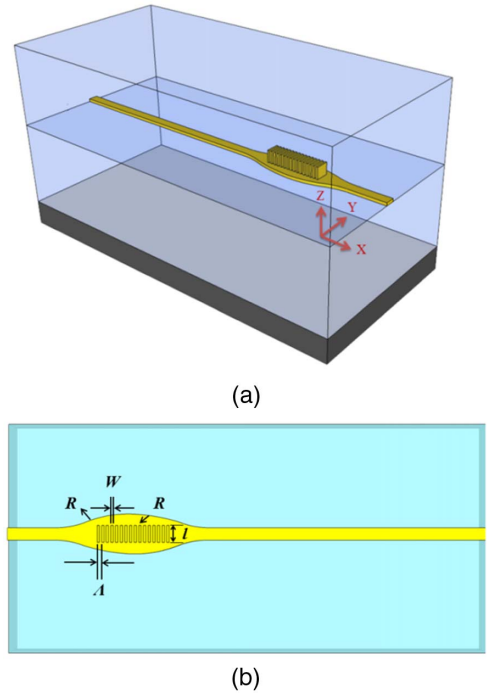

Fig. 7. (a) 3D sketch showing the structure of interest with a nonadiabatic flared stripe. (b) Top view of the nonadiabatic flared stripe. The radius of curvature R, the width W and length l of the ridges, and the pitch Λ of the grating are shown.

is 20 μm long and 12 μm wide sharply curved down to a 5 μm width matching the straight stripe width, whereas the adiabatic flared stripe is 120 μm long and 12 μm wide gradually curved down to 5 μm. The corresponding radii of curvature are $R = 5$ μm in the nonadiabatic structure and $R = 4000$ μm in the adiabatic structure. The purpose of the flared stripes is to widen the grating to 10 μm (i.e., lengthen the grating ridges to $l = 10$ μm) in order to accommodate a larger diameter incident Gaussian beam, thereby facilitating alignments. The adiabatic flared stripe ensures a low-loss transition between a large Gaussian beam and the LRSPP mode of the straight stripe, thereby improving the coupling of input light relative to the nonadiabatic flared stripe. Both flared stripes also help minimize coupling of input light to slab modes. The structure embedded in fluoropolymer of Fig. 1(a) and the structure incorporating the 1DPC of Fig. 1(b) are considered. In previous work, it was demonstrated that $l = 4$ μm long grating ridges on a 5 μm wide straight stripe produced significant scattering of input light into slab modes in addition to exciting the LRSPP mode of the waveguide [29]—it is anticipated that longer ridges on flared stripes will improve the coupling of light into the LRSPP mode while minimizing coupling to slab modes (the latter are deleterious as they produce undesirable background in the output light). As an alternative, the whole grating region can be curved to focus light directly onto the waveguide, in the case where unidirectional coupling is desired, following approaches in Si photonics [33–35].

Full vectorial 3D-FDTD simulations were carried out using FDTD Solutions (Lumerical). The optimized 2D design obtained from FEM analysis was expanded to 3D (along y) to investigate the effects of the flared stripe on the quality of the excited LRSPP. The 3D computational area was set to 425 × 26 × 26 μm^3, and the boundaries were terminated by PMLs. The simulation grid was defined as an automatic conformal mesh everywhere except in the gold regions, where it was explicitly defined to have a space step of 5 nm. A 2D Gaussian beam was launched 10 μm above the grating plane through a square aperture 100 μm^2 in area. The beam waist radius was initially set to 2 μm, but larger radii were also investigated. The beam was aligned with the center of the grating to exploit structural symmetry, thereby enabling us to shrink the computational volume to 1/4 of the full domain. Thus, a perfect electric wall and a perfect magnetic wall were placed through the transverse and longitudinal centers of the structure. When the input Gaussian beam is aligned to the center of the grating, the beam splits to excite fields in equal proportion along the $+x$ and $-x$ directions. Figure 8 shows top views as the Gaussian beam is perpendicularly incident on the grating at different distances above the grating plane as well as a cut through the middle of the grating ridges.

The electric field distributions over y–z cross sections taken at various locations x from the edge of the grating are shown in Fig. 9, for the structure embedded in fluoropolymer [Fig. 9(a)] and the one on a 1DPC [Fig. 9(b)], for the case of a nonadiabatic flared stripe. As is evident from Fig. 9(a), the transient fields are very strong close to the grating, but vanish gradually such that the unvarying and stable field profile of the LRSPP mode eventually emerges. A secondary beam diffracted at an angle up from the stripe is also apparent from the field cuts of Fig. 9(a) taken close to the grating—this beam is also observed in the 2D modelling as seen in the longitudinal cut of Fig. 5. The LRSPP mode field peaks along the metal surfaces, enabling high-surface-sensitivity biosensors, as in the case of straight gold waveguides excited using butt-coupling [19–22]. The Bloch LRSPP of Fig. 9(b) has a field distribution in the upper cladding similar to that of the LRSPP in the homogeneous structure [Fig. 9(a)], but its distribution in the 1DPC forming the lower cladding is evanescent with an oscillatory character as expected for a Bloch mode [28,29].

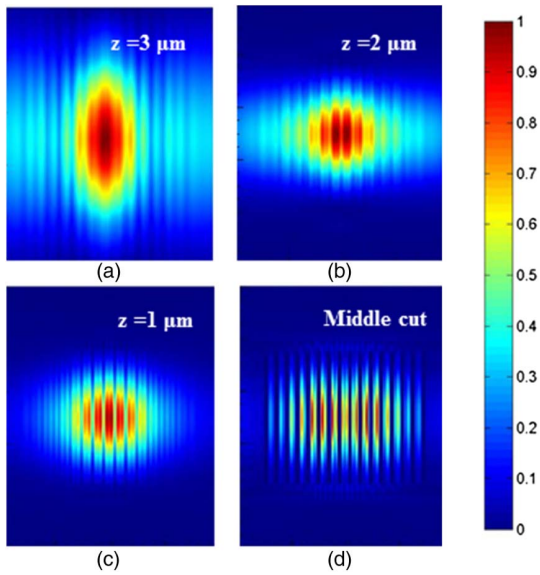

Fig. 8. Field distribution (magnitude) of the perpendicularly incident Gaussian beam over several x–y planes (18 × 18 μm^2 in area) at different heights above the grating and at a simulation time when the beam is interacting with the grating: (a) 3 μm above the grating, (b) 2 μm above the grating, (c) 1 μm above the grating, and (d) through the middle of the grating ridges.

Field distributions taken at cross sections 180 μm away from the grating are shown in Fig. 10 for the nonadiabatic [Figs. 10(a) and 10(c)] and adiabatic [Figs. 10(b) and 10(d)] flared stripes for Gaussian beams of two radii, for the structure embedded in fluoropolymer. As can be seen, increasing the radius of the Gaussian beam causes the mode to become increasingly distorted as more background light is introduced into the distribution due to scattering of input light into slab modes. This effect is more evident in the case of the nonadiabatic flared stripe. Thus, exciting the grating with a Gaussian beam that is size-matched to the LRSPP reduces the background light, as does using an adiabatic flared stripe under the grating coupler [Fig. 10(b)].

The output coupling characteristics of our optimal grating design on the nonadiabatic flared stripe for the structure embedded in fluoropolymer was examined using our full 3D model. A mode source originating at a distance $L = 25$ μm to the left edge of the grating was defined using a finite difference mode solver. The LRSPP mode used to excite the system has an effective index of $n_{\text{eff}} = 1.3408 + j0.0002$ (MPA of 8.83 dB/mm). The computational domain was set to a volume of 55 × 26 × 45 μm^3 and terminated using PMLs on all

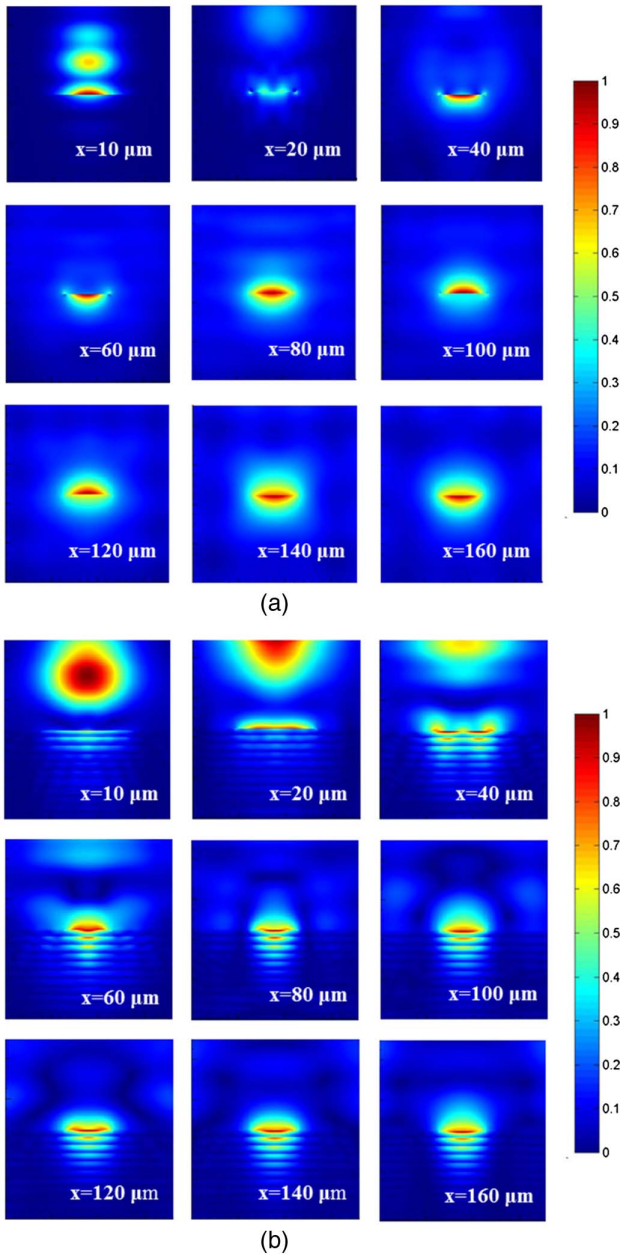

Fig. 9. Evolution of the $|E_z|$ field at several y–z cross-sectional planes located along the length of the waveguide at $-x \sim 10$, 20, 40, 60, 80, 100, 120, 140, and 160 μm away from the grating, plotted over a 18×18 μm^2 area. (a) Structure embedded in fluoropolymer, showing fields that eventually evolve to reveal the LRSPP mode. (b) Structure with the 1DPC, showing fields that eventually evolve to reveal the Bloch LRSPP mode.

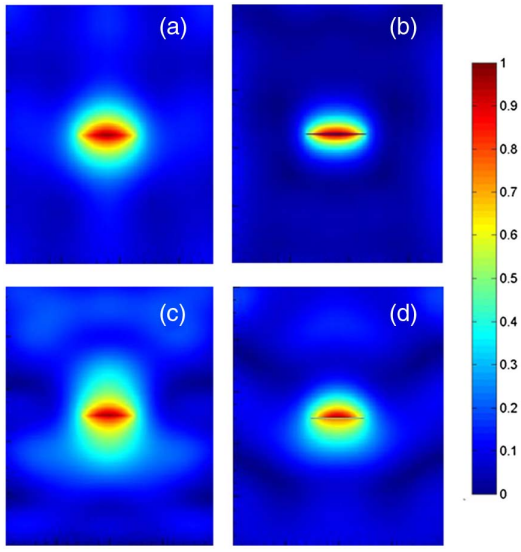

Fig. 10. Distribution of the $|E_z|$ field at a y–z cross-sectional plane located along the length of the waveguide 180 μm away from the grating for the structure embedded in fluoropolymer [Fig. 1(a)]. (a) Nonadiabatic flared stripe, 2 μm Gaussian beam radius. (b) Adiabatic flared stripe, 2 μm Gaussian beam radius. (c) Nonadiabatic flared stripe, 4 μm Gaussian beam radius. (d) Adiabatic flared stripe, 4 μm Gaussian beam radius.

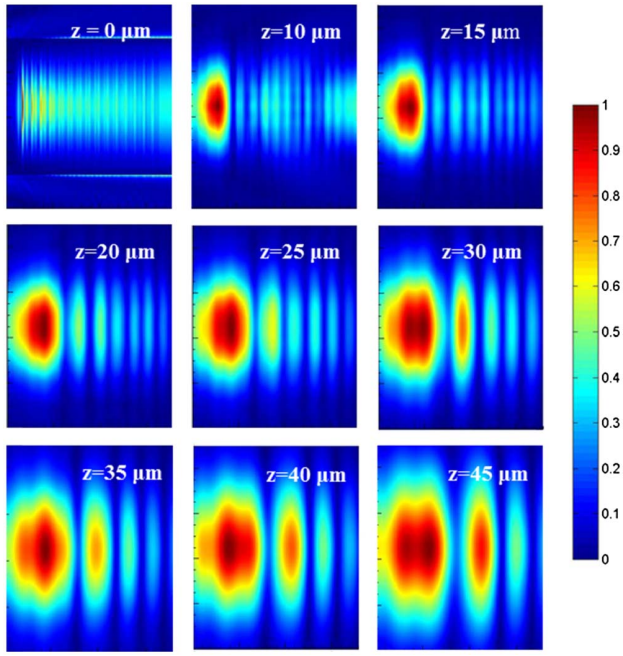

Fig. 11. Field distribution $|\mathbf{E}|$ of perpendicularly emerging light over several x–y planes (18×18 μm^2 in area) at different distances above the grating plane (indicated on each panel) and at a simulation time when the beam is interacting with the grating. The main lobe, located near the first grating ridge, broadens with increasing distance from the grating.

boundaries. The mesh was defined automatically as a conformal mesh everywhere except within the Au regions where the mesh dimensions were set to 5 nm. Power monitors were defined at different locations above the grating coupler to assess its directionality.

Figure 11 shows the distribution of the electric field magnitude $|\mathbf{E}|$ over a portion of the x–y plane at different locations z above the grating, including at $z = 0$. From this figure, it is observed that the main perpendicular radiation lobe is launched near the first grating ridge, and that it broadens with increasing distance from the grating. Although distorted, the field distributions bear some resemblance to a Gaussian beam.

4. EXPERIMENTAL RESULTS

The grating structure proposed in this study was fabricated and characterized for the purposes of concept verification. A multilayer wafer, consisting of a stack of dielectric layers of SiO_2 and Ta_2O_5 as prescribed in Section 2, was used as the starting wafer. A bilayer lift-off photolithography process involving LOR 1A and SPR 955 was used to define Au waveguides. The wafer was exposed and then developed using MF CD-26, followed by metallization and lift-off. A layer 35 nm thick of Au was thermally evaporated on a 0.3 nm thick Cr adhesion layer (also evaporated) to realize the Au stripes. A bilayer lift-off e-beam lithography process, consisting of PMMA 495K A6 and PMMA 950K A2, was used to define the Au gratings. The wafer was exposed and then developed using MIBK:IPA (3:1) solution at 20°C. A layer 160 nm thick of Au was thermally evaporated and lifted off overnight in an acetone bath to form the grating ridges. The waveguides were coated with Cytop as the upper cladding following the procedure described in Ref. [36]. Optical and scanning electron microscope images of fabricated structures are shown in Fig. 12.

The wavelength response of structures consisting of input and output gratings in cascade with a length of stripe [as in Fig. 12(a)] were measured using an optical setup with a tunable laser operating near 1300 nm. A polarization-maintaining single-mode optical fiber and a multimode optical fiber, aligned perpendicularly to the input and output gratings, were used as the input and output means in an experimental arrangement similar to that described in Ref. [24]. The wavelength response for gratings consisting of 4 μm wide ridges ($W = 450$ nm, $\Lambda = 1000$ nm) on a 5 μm wide straight stripe, and for gratings consisting of 10 μm wide ridges ($W = 380$ nm, $\Lambda = 980$ nm) on a 12 μm wide adiabatic flared stripe, are shown in Fig. 13. In both cases the input and output gratings were separated by a waveguide of length 1000 μm. It can be seen from these measurements that the maximum output power is 8 dB higher for the optimal design on an adiabatic flared stripe compared with the narrower design on a straight stripe. The maximum output power obtained at 1350 nm corresponds to an insertion loss of 24 dB. The mode power attenuation expected for the Bloch

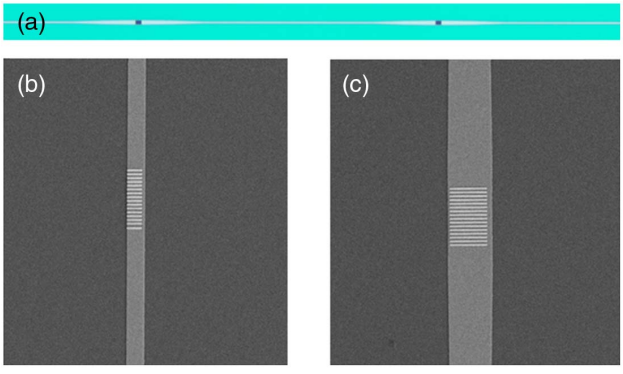

Fig. 12. Optical and scanning electron microscope images of fabricated structures, showing Au waveguides incorporating grating couplers. (a) Input and output gratings in cascade with a length of waveguide; (b) grating on a straight stripe ($W = 450$ nm, $\Lambda = 1000$ nm); (c) grating on an adiabatic flared stripe ($W = 380$ nm, $\Lambda = 980$ nm).

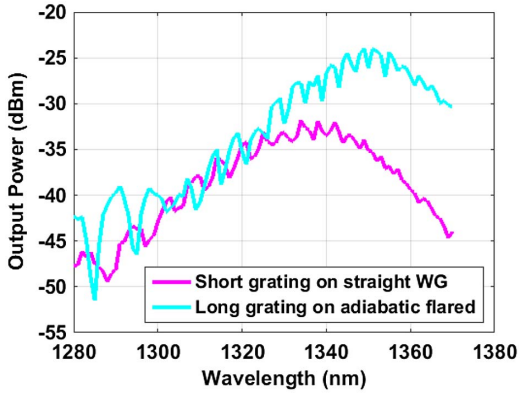

Fig. 13. Wavelength response of fabricated devices following the arrangement of Fig. 12(a) with grating couplers on a straight stripe ($W = 450$ nm, $\Lambda = 1000$ nm) and on an adiabatic flared stripe ($W = 380$ nm, $\Lambda = 980$ nm).

LRSPP on this waveguide is about 8 dB/mm, which implies 16 dB total coupling loss for the input and output gratings. Considering that the input and output gratings have identical designs, a coupling loss of 8 dB is assigned to each, which corresponds to a 16% coupling efficiency. It should be noted that the incident beam emerging from the input cleaved fiber is not very well focused onto the grating, resulting in a coupling loss that is higher than expected. Using a tapered or lensed input fiber to produce a smaller beam on the input grating (as in Section 3.B) would improve the coupling efficiency.

5. CONCLUSION

Gratings capable of coupling an incident Gaussian beam into LRSPPs propagating along a Au stripe embedded in fluoropolymer, or into Bloch LRSPPs propagating along a Au stripe on a truncated 1DPC covered with fluoropolymer, were proposed, investigated, and optimized. The gratings comprise an array of rectangular Au ridges on a flared Au stripe. The structural parameters of the ridges, such as their width and height, and period used for the arrangement were varied to maximize the coupling efficiency for the case of broadside excitation by a Gaussian beam. We find a maximum input coupling efficiency of 25% at $\lambda_0 = 1310$, for an optimized grating design ($W = 380$ nm, $\Lambda = 980$ nm, $H = 160$ nm on a pedestal of height 20 nm). The use of adiabatic and nonadiabatic flared stripes was proposed in order to support wider gratings (i.e., longer ridges) that are size-matched to a larger incident Gaussian beam. Adiabatic flared stripes were found to work best in maintaining a high coupling efficiency to large beams, while minimizing the background light coupled into slab modes of the structures. The gratings were also examined in terms of their output coupling ability, consisting of coupling LRSPPs or Bloch LRSPPs into perpendicularly directed light, resembling a Gaussian beam. Structures were fabricated, and their wavelength responses were acquired, thereby verifying the design improvements consisting of using wide grating ridges on an adiabatic flared stripe.

REFERENCES

1. P. Berini, "Long-range surface plasmon polaritons," Adv. Opt. Photon. **1**, 484–588 (2009).
2. J. Homola, "Present and future of surface plasmon resonance biosensors," Anal. Bioanal. Chem. **377**, 528–539 (2003).
3. J. Homola, "Surface plasmon resonance sensors for detection of chemical and biological species," Chem. Rev. **108**, 462–493 (2008).
4. X. D. Hoa, A. Kirk, and M. Tabrizian, "Towards integrated and sensitive surface plasmon resonance biosensors: a review of recent progress," Biosens. Bioelectron. **23**, 151–160 (2007).
5. J. Lu, C. Petre, E. Yablonovitch, and J. Conway, "Numerical optimization of a grating coupler for the efficient excitation of surface plasmons at an Ag-SiO_2 interface," J. Opt. Soc. Am. B **24**, 2268–2272 (2007).
6. I. P. Radko, S. I. Bozhevolnyi, G. Brucoli, L. Martín-Moreno, F. J. García-Vidal, and A. Boltasseva, "Efficiency of local surface plasmon polariton excitation on ridges," Phys. Rev. B **78**, 115115 (2008).
7. I. P. Radko, S. I. Bozhevolnyi, G. Brucoli, L. Martín-Moreno, F. J. García-Vidal, and A. Boltasseva, "Efficient unidirectional ridge excitation of surface plasmons," Opt. Express **17**, 7228–7232 (2009).
8. Y. Bao, H. Liang, H. Liao, Z. Li, C. Sun, J. Chen, and Q. Gong, "Efficient unidirectional launching of surface plasmons by multi-groove structures," Plasmonics **12**, 1425–1430 (2017).
9. J. Andkjear, S. Nishiwaki, T. Nomura, and O. Sigmund, "Topology optimization of grating couplers for the efficient excitation of surface plasmons," J. Opt. Soc. Am. B **27**, 1828–1832 (2010).
10. P. Berini, "Bulk and surface sensitivities of surface plasmon waveguides," New J. Phys. **10**, 105010 (2008).
11. V. N. Konopsky and E. V. Alieva, "Long-range plasmons in lossy metal films on photonic crystal surfaces," Opt. Lett. **34**, 479–481 (2009).
12. P. Berini, R. Charbonneau, N. Lahoud, and G. Mattiussi, "Characterization of long-range surface-plasmon polariton waveguides," J. Appl. Phys. **98**, 043109 (2005).
13. J. Dostálek, A. Kasry, and W. Knoll, "Long range surface plasmons for observation of biomolecular binding events at metallic surfaces," Plasmonics **2**, 97–106 (2007).
14. P. Berini, R. Charbonneau, and N. Lahoud, "Long-range surface plasmons on ultrathin membranes," Nano Lett. **7**, 1376–1380 (2007).
15. R. Charbonneau, E. Lisicka-Shrzek, and P. Berini, "Broadside coupling to long-range surface plasmons using an angle-cleaved optical fiber," Appl. Phys. Lett. **92**, 101102 (2008).
16. R. Daviau, E. Lisicka-Skrzek, R. N. Tait, and P. Berini, "Broadside excitation of surface plasmon waveguides on Cytop," Appl. Phys. Lett. **94**, 091114 (2009).
17. Asahi Glass Company, "Cytop Technical Brochure," http://www.agc.com.
18. Chemours Company, "Teflon Technical Brochure," http://www.chemours.com.
19. W. R. Wong, S. D. Sekaran, F. R. M. Adikan, and P. Berini, "Detection of dengue NS1 antigen using long-range surface plasmon waveguides," Biosens. Bioelectron. **78**, 132–139 (2016).
20. O. Krupin and P. Berini, "Detection of leukemia markers using long-range surface plasmon waveguides functionalized with Protein G," Lab Chip **15**, 4156–4165 (2015).
21. M. Khodami and P. Berini, "Biomolecular kinetics analysis using long-range surface plasmon polariton," Sens. Actuators B **243**, 114–120 (2017).
22. M. Khodami and P. Berini, "Low detection limits using sandwich and inhibition assays on long-range surface plasmon waveguide biosensors," Sens. Actuators B **273**, 1156–1161 (2018).
23. C. Chen and P. Berini, "Grating couplers for broadside input and output coupling of long-range surface plasmons," Opt. Express **18**, 8006–8018 (2010).
24. N. R. Fong and P. Berini, "Characterization of grating-coupled long range surface plasmon polariton membrane waveguide," Opt. Express **23**, 17421–17430 (2015).
25. Z. Hirbodvash, M. Khodami, N. R. Fong, E. Lisicka-Skrzek, A. Olivieri, H. Northfield, R. N. Tait, and P. Berini, "Grating couplers fabricated by e-beam lithography for long-range surface plasmon waveguides embedded in a fluoropolymer," Appl. Opt. **58**, 2994–3002 (2019).
26. V. N. Konopsky and E. V. Alieva, "Long-range propagation of plasmon polaritons in a thin metal film on a one-dimensional photonic crystal surface," Phys. Rev. Lett. **97**, 253904 (2006).
27. E. V. Alieva and V. N. Konopsky, "Photonic crystal surface waves for optical biosensors," Anal. Chem. **79**, 4729–4735 (2007).
28. A. Delfan, I. Degli-Eredi, and J. E. Sipe, "Long-range surface plasmons in multilayer structures," J. Opt. Soc. Am. B **32**, 1615–1623 (2015).
29. N. R. Fong, M. Menotti, E. Lisicka, H. Northfield, A. Olivieri, N. Tait, M. Liscidini, and P. Berini, "Bloch long-range surface plasmon polaritons on metal stripe waveguides on a multilayer substrate," ACS Photon. **4**, 593–599 (2017).
30. W. R. Wong, H. Fan, F. R. M. Adikan, and P. Berini, "Multichannel long-range surface plasmon waveguides for parallel biosensing," J. Lightwave Technol. **36**, 5536–5546 (2018).
31. B. E. Saleh and M. C. Teich, *Fundamentals of Photonics* (Wiley, 2018).
32. J. Homola, I. Koudela, and S. S. Yee, "Surface plasmon resonance based on diffraction gratings and prism coupler: sensitivity comparison," Sens. Actuators B **54**, 16–24 (1999).
33. R. Halir, P. J. Bock, P. Cheben, A. Ortega-Moñux, C. Alonso-Ramos, J. H. Schmid, J. Lapointe, D.-X. Xu, J. G. Wangüemert-Pérez, Í. Molina-Fernández, and S. Janz, "Waveguide subwavelength structures: a review of principals and application," Laser Photon. Rev. **9**, 25–49 (2015).
34. R. Waldhausl, B. Schnabel, P. Dannberg, E.-B. Kley, A. Bräuer, and W. Karthe, "Efficient coupling into polymer waveguides by gratings," Appl. Opt. **36**, 9383–9390 (1997).
35. F. Van Laere, T. Claes, J. Schrauwen, S. Scheerlinck, W. Bogaerts, D. Taillaert, D. Van Thourhout, and R. Baets, "Compact focusing grating couplers for silicon-on-insulator integrated circuits," IEEE Photon. Technol. Lett. **19**, 1919–1921 (2007).
36. S. Hassan, M. Khodami, R. N. Tait, and P. Berini, "Fabrication of long-range surface plasmon-polariton Bragg gratings with microfluidic channels in Cytop cladding," Microelectron. Eng. **135**, 38–44 (2015).

Chapter 6

Bloch long-range surface plasmons on Au waveguides integrated with Pt counter electrodes as multimodal biosensors

6.1 Summary

A novel optical biosensor operating with Bloch LRSPPs on waveguide arrays integrating with electrochemical biosensors is presented in this chapter. The device is capable of simultaneous optical and electrochemical sensing based on a multichannel multimodal strategy. Multi-channel multi-modal strategy detection provides additional measurements to improve reliability in a disease detection problem. The device is fabricated on a multilayer wafer composed of alternating layers of SiO_2 and Ta_2O_5. Optical biosensors consist of Au waveguides incorporating grating couplers (as input/output means) and supporting Bloch LRSPP within the bandgap of the 1DPC over a limited wavenumber and wavelength range, as described in detail in Chapter 5. Au waveguides also operate as a working electrode in conjunction with a neighboring Pt electrode to form an electrochemical sensor. Au waveguides, Pt stripes and contact pads (for probing purposes) are fabricated using bilayer lift-off photolithography and the grating couplers are fabricated using electron beam lithography. The wafer is covered with Cytop as the upper cladding which was etched to form the microfluidic channels. The wafer is covered with borofloat silica to seal the device and enable side fluidic access. Details of the fabrication process flow are discussed, and

SEM and AFM analyses are provided to support the fabrication work. Optical measurements are performed using a tunable laser operating near λ= 1300 nm. Fully cladded waveguides incorporating the input and output gratings in cascade with a length of waveguide are used to characterize the optical performance of the structure. Wet measurements are subsequently performed using a custom fluidic fixture enabling side fluidic access. Bulk sensing is performed using solutions with different refractive indices and surface sensing measurement is performed using Bovine Serum Albumin (BSA) protein. Electrochemical measurements including cyclic voltammetry are performed using Au waveguides and Pt stripes as the working and counter electrodes respectively.

6.2 Contribution

The results provided in this chapter are in preparation for publication. Maryam Khodami performed the device fabrication work including photolithography and metallization, electron-beam lithography, microfluidic channel etching, wafer bonding, SEM and AFM inspections on the final product wafer(s). Maryam Khodami, Howard Northfield and Ewa Lisicka-Skrzek contributed to channel etching process development and post etching acid clean process discovery as will be described in full detail in Chapter 7. Maryam Khodami measured the wavelength response of the optical biosensors. Zohreh Hirbodvash, and Wei Ru Wong assisted with the optical measurement. Oleksiy Krupin contributed the bulk and surface sensing measurements. Zohreh Hirbodvash contributed the cyclic voltammetry and electrochemical measurement. Choloong Hahn assisted with the FIB imaging. Maryam Khodami interpreted the results and wrote the manuscript. Pierre Berini contributed to the interpretation of the results and revised the manuscript.

6.3 Article

The manuscript presented here is to be submitted for publication.

Bloch long-range surface plasmons on Au waveguides integrated with Pt counter electrodes as multimodal biosensors

Maryam Khodami,[1,2] Zohreh Hirbodvash,[2,3] Oleksiy Krupin,[1,2] Wei Ru Wong,[4] Ewa Lisicka-Skrzek,[2] Howard Northfield,[2] Choloong Hahn[1,2] and Pierre Berini[1,2,3]

School of electrical engineering and computer science, University of Ottawa, 800 King Edward Ave., Ottawa, Ontario, K1N 6N5, Canada
[2] Center for research in Photonics, University of Ottawa, 25 Templeton St., Ottawa, Ontario, K1N 6N5, Canada
[3] Dept. of Physics, University of Ottawa, 150 Louis Pasteur, Ottawa, Ontario, K1N 6N5, Canada
[4] Dept. of Electrical Engineering, Faculty of Engineering, University of Malaya, 50603 Kuala Lumpur, Malaysia

Abstract— **A novel optical biosensor based on Bloch long-range surface plasmon polaritons (LRSPPs) propagating along a waveguide integrated with an electrochemical counter electrode is presented. The structures are fabricated on a truncated 1D photonic crystal comprised of a 15 period stack of alternating layers of SiO_2/Ta_2O_5. The optical biosensors consist of Au stripes supporting Bloch LRSPPs, with integrated grating couplers as input/output means. The Au stripes also operate as a working electrode in conjunction with a neighboring Pt electrode to form an electrochemical sensor. The waveguide structures are fabricated using bilayer lift-off photolithography and the gratings are fabricated using overlaid e-beam lithography. The planar waveguides are integrated into arrays capable of multichannel biosensing. The wafer is covered with CYTOP as the upper cladding with etched microfluidic channels and is wafer-bonded to a Borofloat silica wafer to encapsulate the fluidic channels and enable edge (in-plane) fluidic interfacing. The wavelength response of grating-coupled optical waveguides operating with Bloch LRSPPs are presented, along with bulk and surface sensing results. Cyclic voltammetry (CV) measurements obtained using the Au and Pt stripes as the working and counter electrodes are also presented.**

***Index Terms*—Bloch LRSPP, Optical biosensor, Electrochemical biosensor, multimodal detection**

I. INTRODUCTION

Long-range surface plasmon polaritons (LRSPPs) supported by dielectric-metal-dielectric structures have received considerable attention in the literature, including for biosensing applications [1]. Unlike single-interface surface plasmon polaritons (SPPs), LRSPPs can propagate over an appreciable length (due to their low attenuation), thus increasing the sensitivity of sensors by increasing the optical interaction length with the sensing medium [2], or by producing a sharp resonance under spectral or angular interrogation in a prism-coupled system [3,4]. A conventional waveguide biosensor structure supporting LRSPPs is composed of a Au waveguide embedded in CYTOP with microfluidic channel etched over a portion of the device enabling top fluidic exchange [5-8].

LRSPP waveguide biosensors are typically excited via end-fire coupling [5-8], and although coupling efficiencies greater than 90% can be achieved using this scheme, coupling is strongly dependent on facet quality, which may require

polishing. As an alternative, prism couplers could be used to excite LRSPPs [3,4] as in conventional single-interface SPP biosensors [9], and although straightforward, the prism adds bulk and is incompatible with integration and miniaturization. Among other coupling techniques, grating couplers for dielectric waveguides [10], SPPs [11-15] and LRSPPs [16-18] have attracted significant attention due to their compatibility with planar technologies and integrated optics.

In typical LRSPP waveguide biosensors [5-8] the metal stripe is covered by an aqueous solution and supported by a substrate that has a refractive index close to water, *e.g.*, CYTOP [19] or Teflon [20]. Fluoropolymers such as CYTOP exhibit softening behavior above their glass transition temperature (T_g) which introduces limitations in fabrication processes. A truncated 1D photonic crystal (1DPC) can replace a low-index polymer cladding to support Bloch LRSPPs within the bandgap of the 1DPC over limited ranges of wavenumber and wavelength [21-24]. Given their compatibility with planar technology, gratings and Au stripes on a truncated 1DPC [24, 25] can be integrated to form an array of biosensors enabling multi-channel biosensing. Multi-channel detection provides additional measurements to improve reliability in a disease detection problem. In addition, a Au stripe could also be used as a working electrode in conjunction with a neighboring Pt electrode to form an electrochemical sensor. Thus, the device is capable of simultaneous optical and electrochemical sensing and could be used to address disease detection problems using a multimodal strategy.

Previous reports of joint optical/electrochemical sensing platforms are limited to SPPs excited in prism-coupled systems, where changes in the optical parameters of the medium at the metal/liquid interface due to electrochemical reactions occurring thereon cause a shift in the reflection minimum. As such, SPPs were used as an optical probe of electrochemical reactions [26], where a prism covered with a thin silver film was used in an ATR configuration in contact with perchlorate and halide electrolytes. In another study, a flow-through electrochemical SPP resonance system was employed to investigate the electrochemical reactions in a hydroquinone–benzoquinone system, where the semiquinone radical was detected by producing a large negative SPR shift [27]. An electrochemical SPP biosensor with an absorptive redox mediator film was used for the detection of reversible refractive index changes that occur in the film during potentiostatic oxydoreduction [28]. An optoelectrochemical sensor based on an electrochromic thin-film sensing layer on top of a planar waveguide was reported in [29], where the oxidation state of the sensing film was measured by the evanescent field of the waveguide. An electrochemical/SPP glucose biosensor capable of detecting enzymatic reactions in a conducting glucose polymer oxidase (GO_x) multilayer thin film was reported in [30]. A gold-coated graded index channel waveguide sensor, designed for simultaneous electrochemical and SPP sensing, was designed and fabricated in [31], and changes in the transmittance through the device were measured simultaneously while cyclic voltammetry was carried out in sulphuric or perchloric acid solutions. Electrochemistry on a localized surface plasmon resonance (LSPR) sensor was demonstrated in [32], where using cyclic voltammetry synchronized with LSPR sensing, surface reactions on gold nanostructures were detected electrically and optically.

Numerous studies have also shown that plasmon-induced hot carriers (electrons and holes) generated on metal nanoparticles (*e.g.,* Ag, Au and Cu) catalyze reactions when excited by visible and near-infrared light [33]. This class of reactions is distinct from photochemical and photocatalytic reactions, where ultraviolet photons are often required to induce reactions. Hot carriers on plasmon-excited nanostructures have been investigated for applications in photovoltaic [34, 35] and photo-catalysis [36-38]. The lifetime of hot carriers is generally very short (100 fs), and as a result plasmon-induced chemical reactions (*e.g.*, redox reactions) occur if the charge transfer and subsequent reactions are faster than the carrier lifetime. Hot carrier induced catalysis has also been successfully realized on metal-semiconductor structures where the semiconductor is used to separate charges and increase their lifetime. Applications such as water splitting using Ag/TiO_2

and Au/TiO_2 [39, 40], and redox reactions of CO/CO_2 using Au/Fe_2O_3 and Au/ZnO [41, 42] have been demonstrated.

In this paper, a novel optical-electrochemical biosensor, based on Bloch LRSPPs propagating along a Au stripe on a truncated 1D photonic crystal integrated with a Pt counter electrode is presented. The structures were fabricated, and optical and electrochemical measurements were obtained, including wavelength responses, bulk and surface sensing responses, and cyclic voltammetry. These results serve as proof of concept, confirming that the device could be used to address disease detection problems using a multimodal strategy.

II. Theoretical

The structure of interest consists of a thin Au stripe (ε_r = -86.8 - j8.322) on a truncated 1D photonic crystal covered with CYTOP ($\varepsilon_r = (1.3348)^2$) as a waveguide supporting Bloch LRSPPs over a range of wavenumbers and wavelengths about λ_0 = 1310 nm. 3D and cross-sectional views of the structure are depicted in Figs. 1(a) and 1(b), showing a 5 μm wide, 35 nm thick Au waveguide, incorporating rectangular Au ridges forming grating couplers, on a truncated 1D photonic crystal (1DPC). The 1DPC is composed of N = 15 periods of a SiO_2/Ta_2O_5 unit cell of thicknesses d_{SiO_2} = 495 nm (n_{SiO_2} = 1.447) and $d_{Ta_2O_5}$ = 235 nm ($n_{Ta_2O_5}$ = 2.069), on a starting layer of SiO_2 of the same thickness, designed to achieve wavenumber matching at free-space wavelengths near λ_0 = 1310 nm. The plasmonic waveguides incorporate non-adiabatic or adiabatic flared regions, constructed from oppositely curved sections of radius R = 5 μm or R = 4000 μm, respectively. The flared regions accommodate 10 μm wide gratings that are size-matched to the perpendicularly-incident *p*-polarized Gaussian beam emerging from the tip of a polarization-maintaining single mode fiber (PM-SMF). The gratings are designed to excite Bloch LRSPPs propagating along the Au stripe [25]. The structure is supported by a Si wafer and the stack is designed such that the losses due to light tunneling into the Si slab are minimized. Fig. 1(b) gives a cross-sectional sketch taken longitudinally along a Au stripe, through a pair of grating couplers, illustrating the excitation scheme. Pt electrodes formed parallel to the Au waveguides within the etched microfluidic channels are also shown in the 3D sketch of Fig. 1(a). Access to the microfluidic channels is provided along the lateral chip facets upon dicing of the wafer, enabling edge (in-plane) microfluidic interfacing.

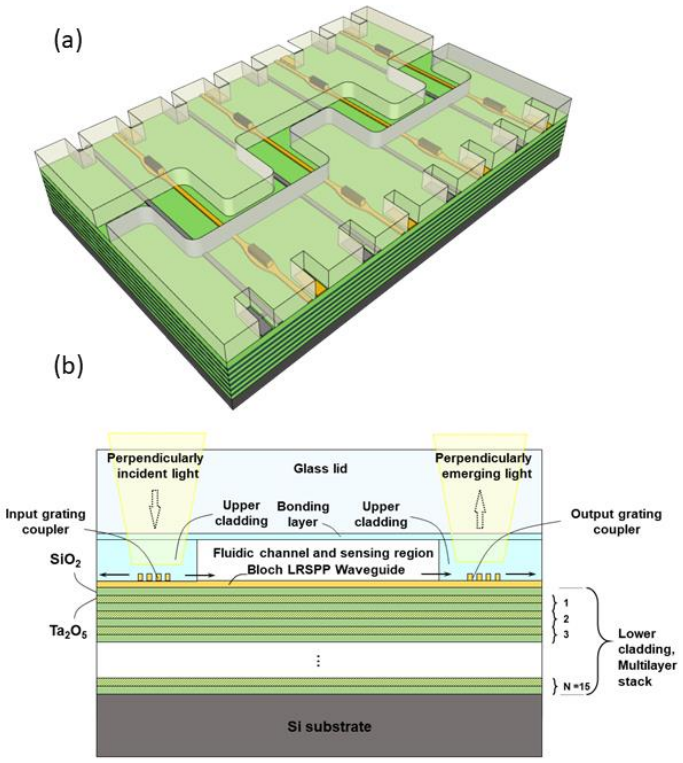

Fig. 1. (a) 3D view of the structure of interest, showing Au stripes and grating couplers on a 15 period stack of alternating layers of SiO_2 and Ta_2O_5 covered with CYTOP. The fluidic channel is etched over a portion of the Au waveguides to allow exposure to the sensing solution. A wafer-bonded lid seals the microfluidic channels. (b) Longitudinal cross-sectional view of the structure.

The dispersion of our 1DPC, computed using the transfer matrix approach [43], is given in Fig. 2. Our 1DPC design consists of 15 periods of alternating layers of SiO_2/Ta_2O_5 of thickness and refractive index given in the previous paragraph (d_{SiO_2} = 495 nm, n_{SiO_2} = 1.447, and $d_{Ta_2O_5}$ = 235 nm, $n_{Ta_2O_5}$ = 2.069, as illustrated in Fig. 1(b)). The dispersion curves of the semi-infinite stack under TM plane wave excitation are plotted in Fig. 2(a), neglecting material dispersion. Light at normal incidence (β = 0, incident away from the grating

couplers) does not encounter a bandgap and propagates through the stack with little reflection.

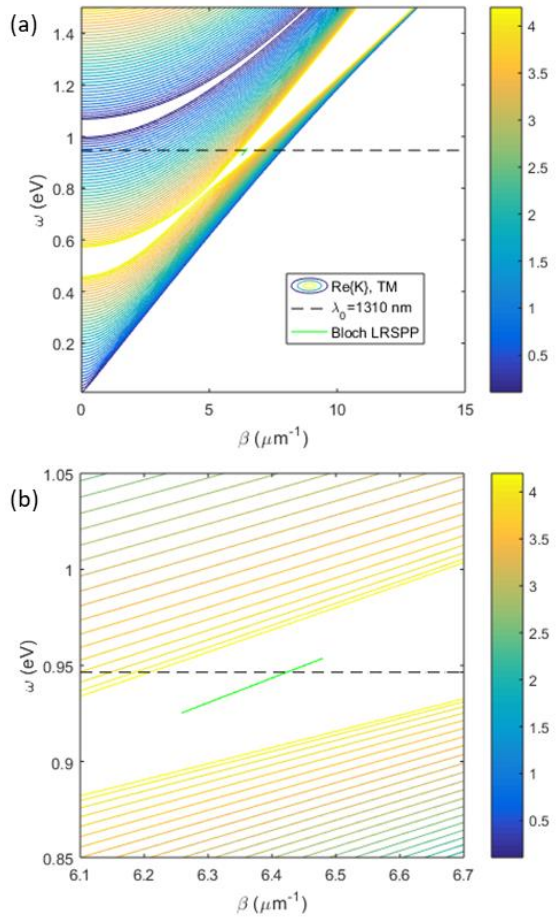

Fig. 2. (a) Dispersion curves of the semi-infinite truncated 1DPC under TM plane wave excitation. λ_0 = 1310 nm is marked as the horizontal dashed line, and the dispersion curve of the Bloch LRSPP on the 1DPC is plotted in green. K is the TM Bloch wavenumber (μm^{-1}) and its real part is plotted as the colored contours; and β is the in-plane wavenumber (μm^{-1}). (b) Expanded view of the region where the Bloch LRSPP is supported

The stack was designed following the prescription of [23], such that the wavenumber of the Bloch LRSPP on the Au stripe on the 1DPC upper-cladded with CYTOP is matched to the wavenumber of the LRSPP on the Au stripe completely embedded in CYTOP at the design wavelength of λ_0 = 1310 nm. The dispersion of the Bloch LRSPP is controlled by the refractive index and thickness of each layer of the 1DPC and are selected such that the Bloch LRSPP propagates in-plane within the first bandgap at λ_0 = 1310 nm. Fig. 2(b) shows the first bandgap in expanded view, with the dispersion curve of the Bloch LRSPP on the 1DPC, computed using a finite-difference mode solver, plotted as the green curve. The dispersion curve is well contained within the first bandgap.

The distribution of the electric field magnitude of the Bloch LRSPP propagating along the waveguide is shown in Fig. 3. As is evident from this figure, the tail of the mode has an oscillating form into the 1DPC as it propagates in plane. The mode also appears to be radiative in-plane, in directions away from the metal stripe, as suggested by wavelets in the 1DPC (this effect is under further investigation).

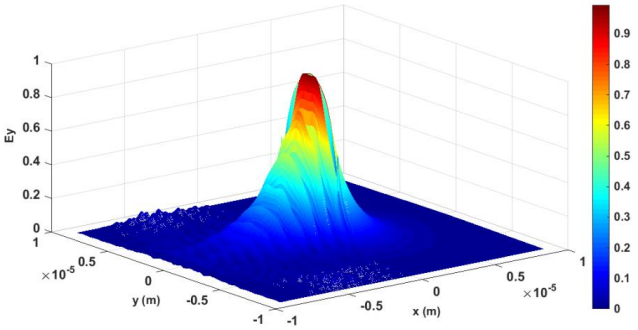

Fig. 3. Distribution of the electric field magnitude of the Bloch LRSPP propagaring along a Au stripe on a truncated 1D photonic crystal.

III. Experimental Results

A. Device Fabrication

The sensor structure of Fig. 1 was fabricated using multiple steps, the main one being the formation of (*i*) Au waveguides, (*ii*) Pt stripes, (*iii*) Au contact pads, (*iv*) Au gratings, (*v*) CYTOP upper cladding, (*vi*) microfluidic channels, and (*vii*) lidding. The structure was fabricated on a multilayer substrate composed of a 15-period stack of SiO_2/Ta_2O_5, acting as a 1D photonic crystal, as described in the theoretical section.

Fig. 4 illustrates the main steps in the fabrication process flow. Au stripes, Pt stripes and Au contact pads were defined using UV lithography, and gratings were defined using electron-beam lithography. Evaporation and lift-off were used in

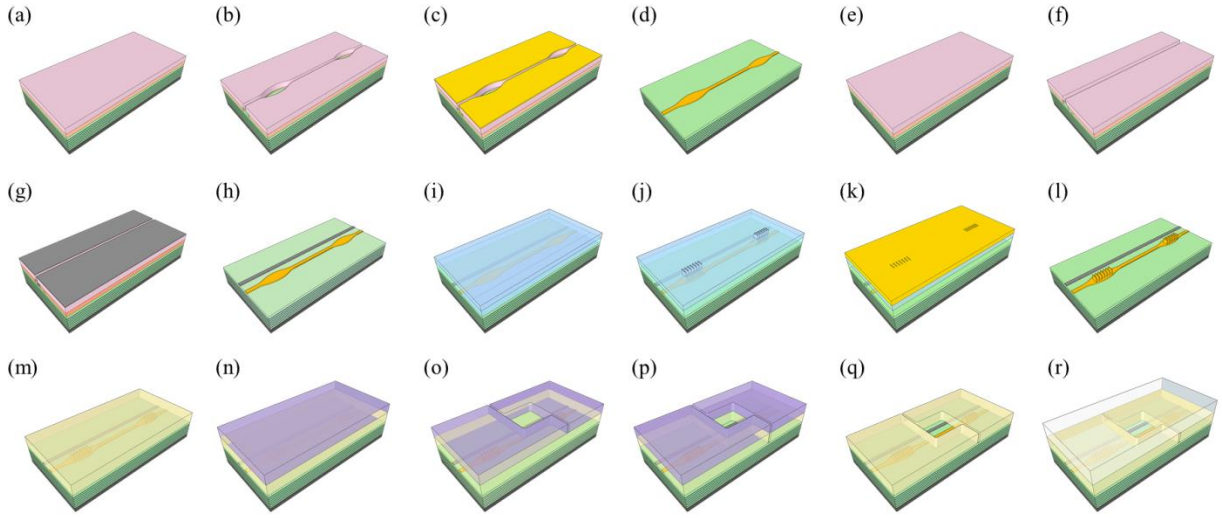

Fig. 4. Fabrication process flow. (a) LOR 1A and SPR 955 deposition; (b) exposure and development to define Au waveguides; (c) Au deposition; (d) lift-off; (e) LOR 1A and SPR 955 deposition; (f) exposure and development to define Pt stripes; (g) Pt deposition; (h) lift-off; (i) PMMA bi-layer deposition; (j) overlay electron-beam exposure and development to define gratings; (k) Au deposition; (l) lift-off; (m) CYTOP upper cladding deposition; (n) SPR 220 deposition; (o) exposure and development to define microfluidic channels; (p) channel etching using O_2 RIE; (q) SPR 220 mask removal; (r) bonding to a Borofloat wafer to seal the microfluidic channels.

in all cases. The microfluidic channels were defined using a lithography step with SPR-220 photoresist as an etch mask, and reactive ion etching (RIE) of the CYTOP upper cladding. Details of these process steps are given in what follows.

Starting Si wafers (4-inch diameter) bearing the prescribed SiO_2/Ta_2O_5 multilayer stack were obtained from Iridian Spectral Technologies. A bilayer lift-off photolithography process involving LOR 1A and Megaposit SPR 955-CM was used to define Au waveguides. LOR 1A was spin coated at 3000 rpm and baked at 180 °C for 5 min. SPR 955 was spin coated at 6000 rpm and baked at 100 °C for 3 min. The wafer was exposed to 85 mJ/cm^2 UV light (i-line filtered) using a contact mask aligner (OAI model 204IR) and then developed for 1 min in a TMAH based solution (Megaposit MF CD-26), followed by metallization and lift-off. A 35 nm thick layer of Au was thermally evaporated (Angstrom Nexdep) on a 0.3 nm thick e-beam evaporated Cr adhesion layer to realize the Au stripes. The waveguides were lifted off using PG remover followed by acetone and IPA cleaning. Pt stripes and Au contact pads were also defined using the same bilayer photolithography process. A 35 nm thick layer of Pt was thermally evaporated on a 0.3 nm thick e-beam evaporated Cr adhesion layer to realize Pt stripes, and a 165 nm thick layer of Au was e-beam evaporated to realize the contact pads providing a total metal thickness of 200 nm for the contact pads (steps not shown in Fig. 4).

A bilayer lift-off e-beam lithography process, involving PMMA 495K A6 and PMMA 950K A2, was used to define the Au gratings. PMMA 495K A6 was spin coated at 3000 rpm and baked at 200 °C for 1 hour. PMMA 950K A2 was spin coated at 4000 rpm and baked at 185 °C for 1 hour. The wafer was covered with ESPACER and exposed to 250 μC/cm^2 e-beam (Raith Pioneer) using a 30 μm aperture, 350 pA beam current, and 30 kV acceleration voltage, and then developed in an MIBK:IPA (3:1) solution at 20 °C for 2 min. A 160 nm thick layer of Au was thermally evaporated and lifted off using an overnight acetone bath to form the grating ridges.

The wafer was then coated with CYTOP as the upper cladding following a procedure described previously [4]. CYTOP M grade (CTL-809 M) was spin coated at 3000 rpm as an adhesive layer for the subsequent deposition of multiple CYTOP S grade (CTX-809 SP2) layers, each spin coated at 1500 rpm. Each layer was baked for 30 min at 50 °C to partially evaporate solvent. The full CYTOP stack

was then baked at 200 °C overnight to ensure the complete removal of solvent. The total thickness of the CYTOP stack was determined to be ~10 μm. An edge bead removal procedure using a shadow mask with RIE was performed to remove the thicker edge of the CYTOP cladding.

The wafer was then subjected to an O_2 ashing step for 30 sec at 50 W, using an oxygen plasma etcher (Plasma-Etch, PE-50), which makes the CYTOP surface hydrophilic. The wafer was then primed with an HMDS adhesion layer (YES-310TA HMDS vapor oven at 100 °C). A lithography step using SPR 220 was applied to define the channels with a dark-field mask. SPR 220 was spin coated at 2300 rpm and post-spin baked at 100 °C for 15 mins. The wafer was then exposed to 1000 mJ/cm^2 of UV light and left at room temperature overnight to allow the resist to evenly moisturize. The wafers were then subjected to a pre-development bake process involving a ramp bake from room temperature to 100 °C, followed by baking at 115 °C for 90 sec, and then cooling from 100 °C to room temperature. Photoresist development consisted of submersion in Megaposit MF-24 for 5 min followed by a DI water rinse and N_2 blow dry. Alternatively, a hard mask, produced by lifting off an Al pattern (following the process used to define the Au waveguides), was also used to define the microfluidic channels.

The patterned wafer was then subjected to O_2 dry etching in an RIE system (Samco RIE-10NR, O_2 flow of 10 sccm, 4 Pa, 25 W RF power) to remove CYTOP and define the microfluidic channels. Full exposure of the Au and Pt stripes in the channels is vital to the operation of the device. An acid clean step, involving the use of Piranha (H_2SO_4 and H_2O_2 (4:1) at 90 °C), in combination with UV ozone cleaning, was performed to ensure complete removal of grass-like residue that formed in the channels as a result of CYTOP etching, as described in full detail in [44]. Briefly, the wafer was subjected to a 10 min CD-26 bath post SPR 220 (or Al) removal, which was followed by immersion for 1 min in a Piranha solution, then a 30 min exposure to UV ozone. This step was repeated once, followed by 2 min RIE in O_2 at 100 W. The roughness on the Au stripes and at the bottom of the microfluidic channels was about 2 nm post cleaning, which indicates that the residue was substantially removed, and the sensing stipes did not incur significant damage.

A wafer bonding process was introduced to seal the channels and facilitate integration of the biosensor chips into the fluidic assembly. The wafer was bonded to a 350 μm thick Borofloat glass wafer (4-inch diameter) covered with CYTOP (1 layer of CYTOP M, followed by 4 layers of CYTOP S, formed as described above). The wafer and the glass lid were mounted in an aligner wafer bonder (AML-AWB). The chamber was closed and evacuated (1×10^{-5} mbar), and the wafers were aligned and brought into close contact. The lower and upper platen temperatures were set to 120 °C, with 5 °C/hour ramp temperature, and the force was set to 1000 N, ensuring proper bonding of the top and bottom substrates. Inter-diffusion of polymer chains across the interface caused by the applied heat and pressure results in a strong adhesive bond between the wafers. Overnight bonding was proven to be sufficient. The chamber was then allowed to cool down to room temperature prior to opening.

The wafers were then covered with SPR 220 as a protective layer and diced into several chips. Dicing naturally produces microfluidic interfaces along the lateral chip edges for in-plane microfluidic coupling (Fig. 1(a)).

Various microscope images of fabricated structures are shown in Fig. 5. Fig. 5(a) gives a scanning electron microscope (SEM) image of a fabricated grating coupler showing 16 rectangular ridges aligned along the width of a Au stripe. Fig. 5(b) shows a cross-section of a fabricated chip incorporating a Au stripe on a 15 period stack of SiO_2 and Ta_2O_5, covered by CYTOP. The cross-section was prepared using focussed ion beam (FIB) milling and the cross-section was imaged using a helium ion microscope (HIM). Briefly, a large imaging trench was opened using a strong Ga beam (beam current 3 nA, step size 10 nm, dwell time 1 μs, dose 10 nC/μm^2). A weaker Ga beam was then used to remove particles and smoothen the facet (beam current 700 pA, step size 5 nm, dwell time 1 μs, dose 10 nC/μm^2).

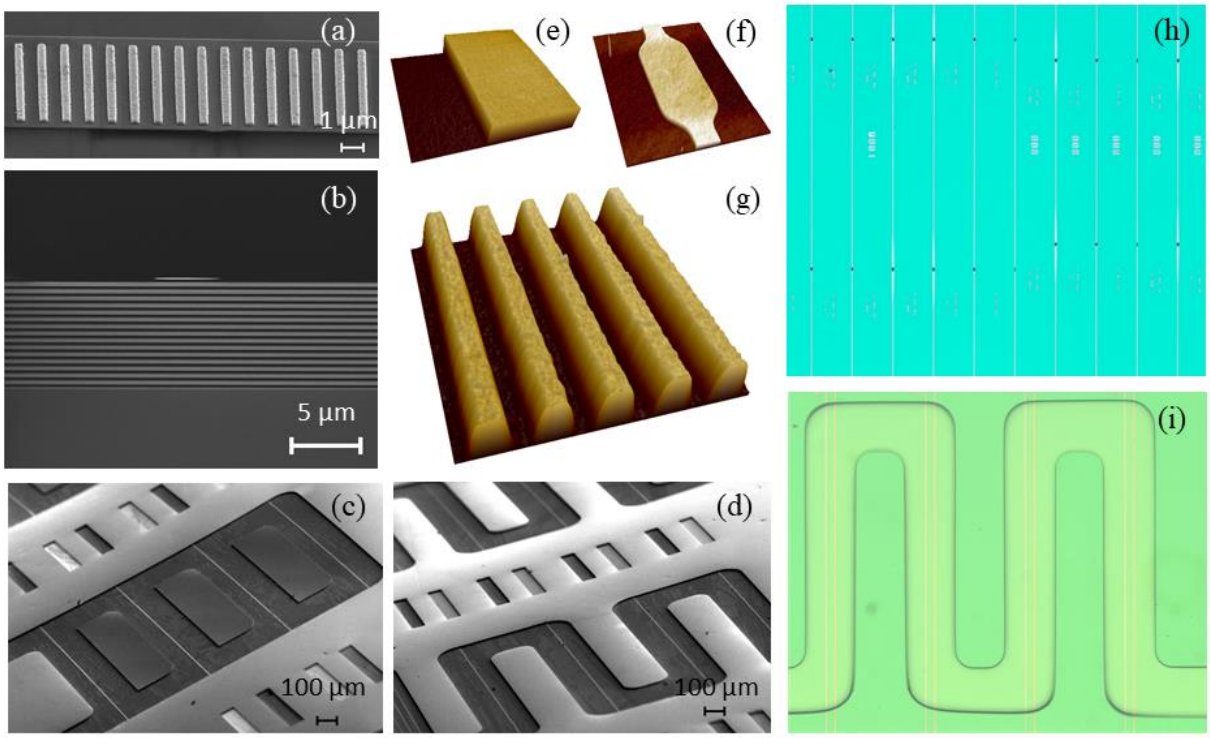

Fig. 5. (a) SEM image of a grating coupler showing 16 rectangular ridges on a Au stripe. (b) Helium ion microscope image of a polished cross-section of a Au waveguide on a multilayer stack, supported by a Si wafer and covered with CYTOP. (c) and (d) two microfluidic channel architectures, post RIE etch but prior to Al mask removal taken at a 45° imaging angle. (e) AFM scan of a portion of a contact pad (25×25 µm^2 scan area, vertical scale of 250 nm). (f) AFM scan of a portion of a Au waveguide showing a flared section which tapers down non-adiabatically to a 5 µm wide waveguide (25×25 µm^2 scan area, vertical scale of 60 nm). (g) AFM scan of a portion of a grating coupler (25×25 µm^2 scan area, vertical scale of 200 nm). (h) Optical microscope image of input and output gratings in cascade with a length of waveguide, arrayed such that the separation between gratings varies. (i) Optical microscope image of a microfluidic channel post wafer bonding with Au and Pt stripes in each channel.

Finally, fine polishing was carried out using a weak Ga beam to produce a facet that was smooth enough to inspect (beam current 300 pA, step size 2 nm, dwell time 1 µs, dose 10 nC/µm^2). A thin Al layer (20 nm) was deposited on top of the sample to assist with charge dissipation. Figs. 5(c) and 5(d) give SEM images of two different microfluidic channel architectures, post CYTOP etching but prior to Al mask removal. Figs. 5(e) - 5(g) collect atomic force microscope (AFM) scans, from which metal thickness and roughness values have been extracted. A metal contact pad (Fig. 5(e)) has a thickness of ~200 nm with a root mean square (rms) roughness of ~2 nm. A Au waveguide with a non-adiabatic flared section (Fig. 5(f)) has a thickness of ~35 nm, with a rms roughness of ~1.2 nm. The metal grating ridges (Fig. 5(g)) have a thickness of ~160 nm and an rms roughness of ~1.8 nm along the top. The rectangular ridges have a width of ~380 nm, a spacing of ~600 nm and a height of ~160 nm. All the dimensions and thicknesses are close to the target ones. An optical microscope image of input and output gratings in cascade with a length of stripe is shown in Fig. 5(h); each structure is a member of an array where the separation between gratings is varied. The flares are 10 µm wide at the location of the gratings and taper down to 5 µm wide straight stripes, as can be observed in this image. Sealed microfluidic channels incorporating a length of Au and Pt stripe, post glass bonding, are shown in Fig. 5(i). The microfluidic channels have dark edges due to non-vertically caused by sloped walls of the SPR 220 mask as well as erosion of the mask during etching [44].

B. Optical Measurements

Devices were characterized optically post cladding deposition (CYTOP), but prior to microfluidic

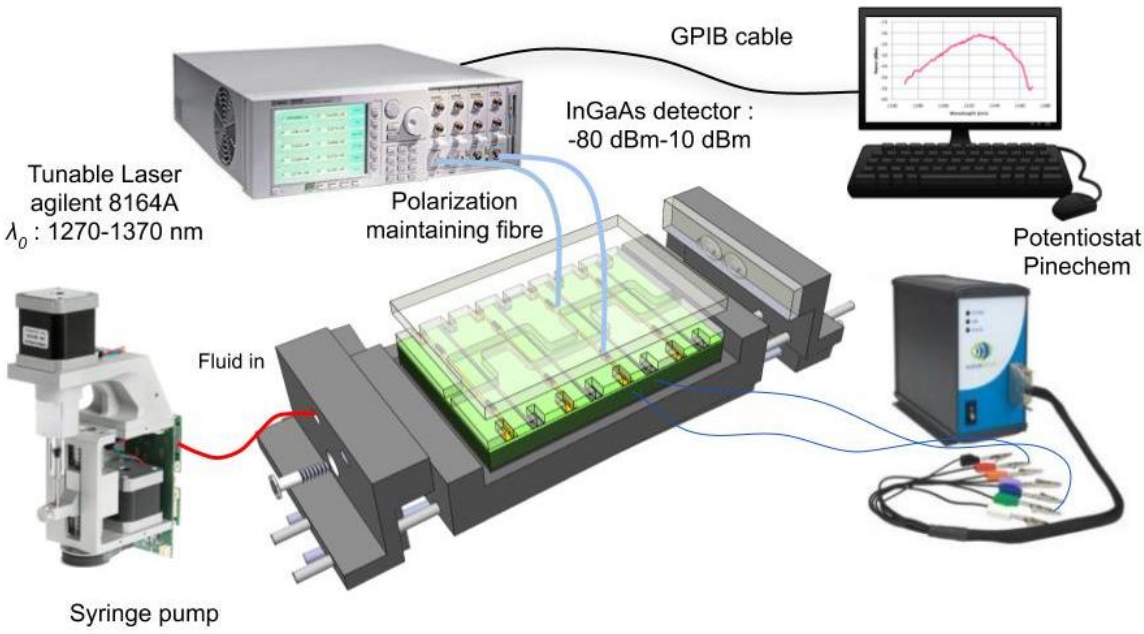

Fig. 6. Experimental setup comprising a tunable laser operating near λ_0 = 1300 nm and a potentiostat to perform optical and electrochemical experiments. The device under test is mounted in a custom fluidic fixture that enables side fluidic interfacing.

channel etching and wafer bonding (lidding), to verify the performance of the Bloch LRSPP waveguides excited via grating couplers, by carrying out wavelength responses and cut-back measurements.

The experimental setup used to carry out the measurements is shown in Fig. 6. The wavelength response of structures incorporating input and output gratings in cascade with a length of stripe was measured using a tunable laser operating near 1300 nm. A polarisation-maintaining single mode fibre (PM-SMF) and a multimode optical fiber, aligned perpendicularly to the input and output gratings, respectively, were used as input/output means. Custom 90º curved metallic holders were used to hold and align the fibers perpendicularly to the gratings, while ensuring that TM-polarized light was incident on the input grating. Several grating pairs of identical design but separated by different lengths of waveguide, as shown in the microscope image of Fig. 5(h), were used to produce cut-back measurements, from which the mode power attenuation (MPA) and coupling losses were deduced.

Fig. 7(a) gives the wavelength response of pairs of identical gratings (W ~ 380 nm, Λ ~ 980 nm, height of ~160 nm) separated by different waveguide lengths of 800, 1000, 1250, 1650, 1850 and 2050 µm. The maximum output power is obtained at λ_0 = 1325 nm, which is red shifted by 15 nm relative to the theoretical design (λ_0 = 1310 nm) [25]. This is due primarily to an increase in the effective index of the Bloch LRSPP mode on the adiabatic flared stripes, which are wider than the straight waveguide used in the theoretical calculations. The MPA (mode power attenuation) and total coupling losses (input/output) were determined by fitting a linear model to the values of insertion loss obtained for different grating separations, at the wavelength corresponding to the maximum output power (λ_0 = 1325 nm in this case). The MPA (slope) works out to 11.8 dB/mm, which is close to expected, and the total coupling losses (intercept) to 24.2 dB. The goodness-of-fit measure for the linear regression model was R^2 = 0.9682. The coupling loss is higher than expected and is mainly ascribed to mode mismatch on the input grating, which can be addressed by using a tapered or lensed PM-SMF

fiber which produces a smaller beam size on the input grating.

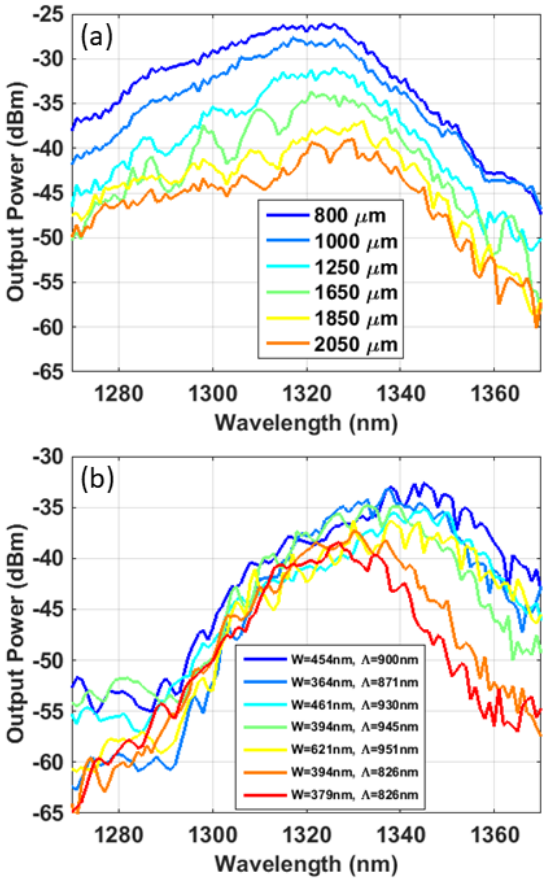

Fig. 7. (a) Wavelength response of pairs of identical gratings with different waveguide separation lengths (800, 1000, 1250, 1650, 1850 and 2050 μm). (b) Wavelength response of identical pairs of gratings, each pair of different pitch Λ and width W, separated by the same length of waveguide (2050 μm).

Fig. 7(b) gives the measured wavelength response of identical pairs of gratings, each pair of different pitch Λ and width W (measured via SEM), separated by the same length of waveguide (2050 μm). It is evident from Fig. 7(b) that a red shift in the grating response is produced by increasing the width W of the ridges or the pitch Λ of the grating. The cases plotted as the red and orange curves have a similar pitch but different widths, from which we observe that the maximum output power is shifted to a longer wavelength for the wider grating ridges (orange curve). Comparing the cases plotted as the red and dark blue curves reveals that the response is also shifted to a longer wavelength for the grating with the larger pitch (dark blue). These trends are as expected from modelling [25].

C. Biosensing Measurements

Materials: 2-Isopropanol (IPA, 733458), acetone (270725), glycerol (49767), bovine serum albumin (BSA, A0281) and phosphate buffered saline (PBS, P5368) 0.01 M, pH 7.4 were obtained from Sigma-Aldrich. A PBS solution was prepared by dissolving packaged salts in 1 L of distilled/deionized water (DDI H_2O).

Preparation: A biosensor chip was taken from a diced wafer. The top Borofloat glass surface, which was coated with dicing resist (SPR 220), was wiped clean using an acetone-dipped swab (TX757B, Texwipe). In order to remove dicing debris from the optical and microfluidic facets, the chip was cleaned in an ultrasonic bath (Fisher Scientific, FS20H) in acetone for 5 min, then washed with IPA and dried under N_2. Removal of possible organic contaminants from the sensing surfaces was performed by placing the chip into a UV/Ozone cleaning chamber (Novascan, PSD series) for 1 hr with the UV lamp on. The Borofloat glass lid (350 μm thick) has a transmittance of ~20% at a wavelength of 250 nm, such that sufficient UV intensity is transmitted through to break down organic material possibly adsorbed into the Au sensing surface.

Next, the device was aligned and clamped into a custom jig providing in-plane fluidic interfaces (Zandbelt Machine Works) [45]. DDI H_2O was injected into the chip using a microfluidic syringe system (SPM - Zero Dead Volume Diluter, Advanced MicroFluidics, Switzerland) for 10 min to ensure leak-free fluid delivery. Next, the chip was aligned into the optical setup (Fig. 6) where a lensed PM-SMF (LPF-D1-1300-7/125-P-0.44-1.1-3.2GR,1.4AS-50-3A-1-1, OZ Optics) connected to the tunable laser was mounted to a curved arm and aligned to the input grating coupler. A multimode optical fiber also mounted to a curved arm was aligned to the output grating coupler and connected to a power sensor (Hewlett Packard 8163A, InGaAs detector module 81635A). The system was aligned until maximum power transmission was observed while a buffer solution index matched to CYTOP flowed in the channel. Sensing solutions of different

refractive indices (RIs) were prepared by mixing PBS buffer with glycerol (PBS/Gly). All experiments were performed at a 4 μL/min flowrate and 5 dBm incident optical power.

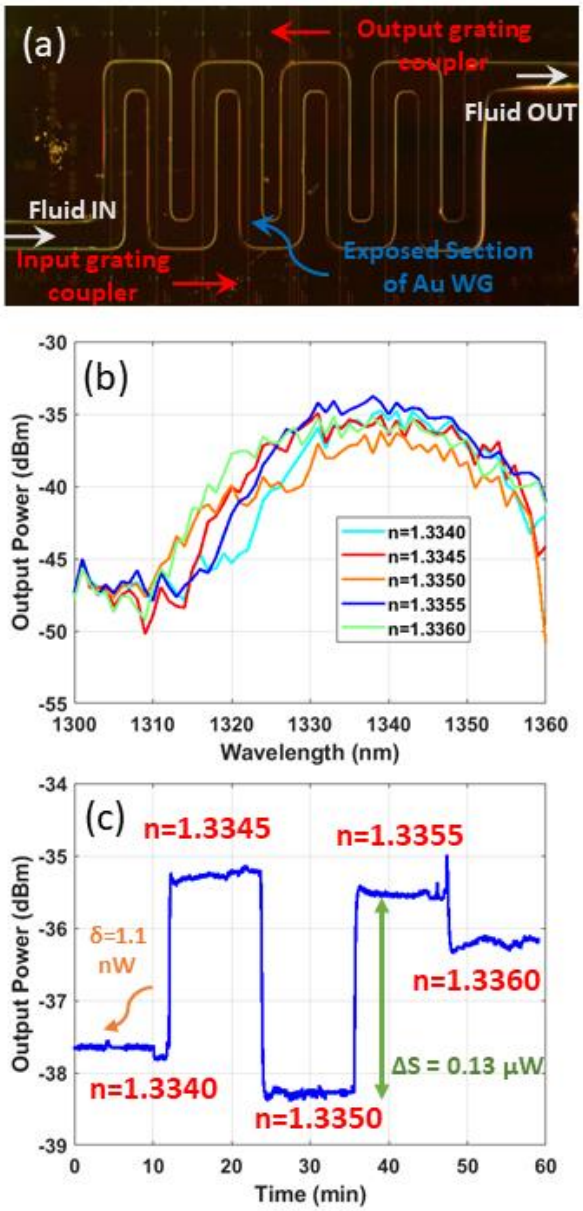

Fig. 8. (a) Microscope image of the biosensor chip tested. (b) Wavelength responses of biosensor over the wavelength range from 1300 to 1360 nm as five solutions of PBS/Gly of refractive indices 1.3340, 1.3345, 1.3350, 1.3355 and 1.3360 were injected. (c) Time response at λ_0 = 1330 nm as the five PBG/Gly solutions were injected

Bulk Sensing: Bulk sensing experiments with 5 solutions of RI near that of Cytop, ranging from 1.3340 to 1.3360 in steps of 5×10^{-4}, were conducted. A microscope image of the sensor tested is given in Fig. 8(a). The solutions were injected at a flow rate of 4 μl/min into the left inlet and emerged from the right outlet. The five solutions were injected sequentially into the chip while we performed alternately two types of measurements: a wavelength sweep from 1300 to 1360 nm in steps of 1 nm for each solution (Fig. 8(b)); and a time response of several minutes for each solution at a fixed wavelength of λ_0 = 1330 nm (Fig. 8(c)).

The wavelength responses plotted in Fig. 8(b) reveal that the largest coupling efficiency occurs at wavelengths in the range from 1330 to 1340 nm. Also, the grating responses are unaffected by the injected solutions because the gratings are cladded in Cytop and unexposed to the fluid. The sensing responses are due only to changes in the waveguide characteristics of the sensing region as different solutions were injected. The system demonstrated moderate stability with higher than expected noise - most likely due to the small channel height (8 μm) which required a high pressure from the pump to maintain the flow rate, causing slight vibration of the chip (in synch with the pump motor).

An oscillatory response with injected solution is evident from the time trace of Fig. 8(c), which was obtained at λ_0 = 1330 nm. The largest power step of 0.13 μW occurred as we switched the solution from that having n = 1.3350 to the one having n = 1.3355. The baseline noise was δ = 1.1 nW, taken as the standard deviation of the power response for the solution having n = 1.3340. Thus, the limit of detection for bulk sensing works out to 4×10^{-6} RIU. A similar bulk oscillatory response was also observed at other wavelengths in the range of 1330 to 1340 nm.

Protein Adsorption: After completion of the bulk sensing experiments, the same waveguide was used to carry out a surface sensing experiment via non-specific adsorption of BSA to the UV/Ozone cleaned Au surface. Based on the bulk responses of the sensor, we chose λ_0 = 1338 nm as the operating wavelength and the RI of the working buffer as n = 1.3350. The waveguide response due to BSA adsorption is given in Fig. 9. A baseline under PBS/Gly flow was established initially for 3 min, followed by injection of a BSA solution (50 μg/ml)

in PBS/Gly (n = 1.3350) for 8 min. As the last step, the fluidic channel was flushed with PBS/Gly, to observe the new baseline level. The rapid adsorption kinetics (90% saturation within 2 min) indicates that the Au stripe was very clean. The adsorbed BSA monolayer produced a signal change of 61.6 nW, with the baseline noise at δ = 0.8 nW, resulting in a signal-to-noise (SNR) ratio of 77.

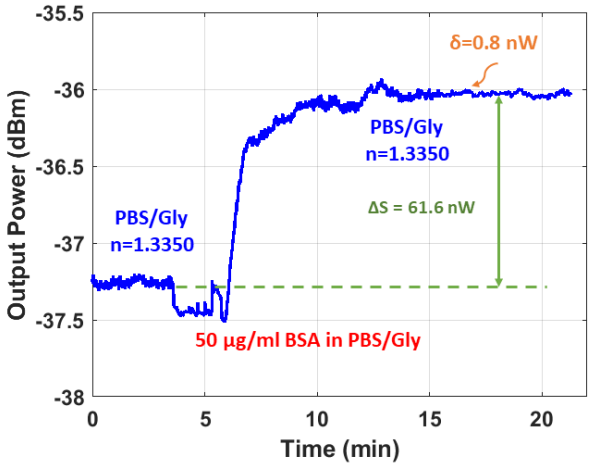

Fig. 9. Non-specific BSA adsorption on a Au sensing waveguide

D. Electrochemical Measurements

A Pt stripe in conjunction with a Au waveguide were also used to perform cyclic voltammetry measurements on intermediate (un-cladded) structures to validate the electrochemical sensing performance of the device. The electrochemical measurements were carried out using a chip incorporating Au and Pt stripes with contact pads, but with no CYTOP upper cladding, with the metallic pads probed directly using tungsten needles. A Pt stripe was used as a counter electrode and a Au stripe as a working electrode.

The measurements were carried out using 70 ml of 1 mM potassium ferricyanide (obtained from Sigma-Aldrich) dissolved in 100 mM potassium nitrate (obtained from Sigma-Aldrich) as the supporting electrolyte. The supporting electrolyte has a low resistance and high ionic strength to ensure that the electric field in the cell is not perturbed by redox reactions in the system. An Ag/AgCl reference electrode establishes a known and stable reference potential for the system. Two tungsten needles attached to the flexible arms of two positioners were used to probe the contact pads. The chip was placed in a petri dish and immersed in electrolyte. The potential was set between the reference electrode and the working electrode, and the current was measured between the counter electrode and the working electrode using the potentiostat following the arrangement suggested in Fig. 6.

Cyclic voltammograms were obtained for different scan rates, ranging from 1 mV/sec to 100 mV/sec as shown in Fig. 10. The cathodic and anodic currents have clear peaks as expected from a typical CV measurement. As can be seen in this figure, the maximum (minimum) current increases (decreases) with increasing scan rate. These results show that the device is capable of electrochemical sensing.

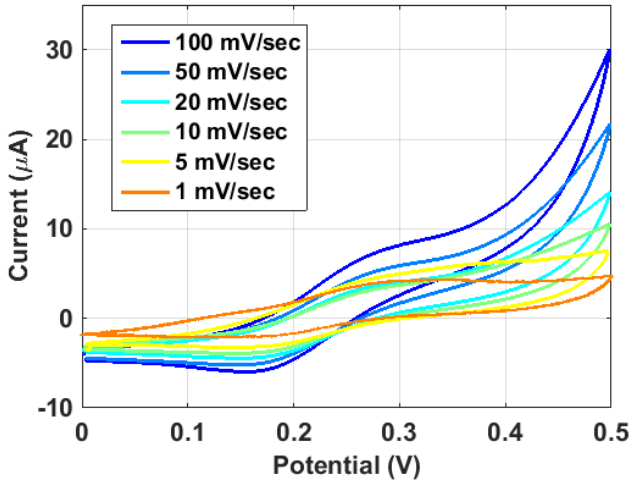

Fig. 10. Cyclic voltammetry measurements on a chip bearing Au and Pt stripes as working and counter electrodes, respectively, as well as and contact pads. Potassium ferricyanide was used as the redox species in a potassium nitrate solution as the electrolyte.

IV. Conclusion

An integrated sensing platform capable of optical and electrochemical sensing was proposed. The device was fabricated on a truncated 1D stack incorporating 15 periods of alternating layers of SiO_2 and Ta_2O_5 to support Bloch LRSPPs over the wavelength range of interest. Au waveguides, Pt

stripes and contact pads were fabricated using UV lithography, and grating couplers were fabricated using overlaid e-beam lithography. The structure was covered with CYTOP as the upper cladding, into which the microfluidic channels were etched. The wafer was bonded to Borofloat silica to seal the channels and enable side fluidic interfacing. The wavelength response of pairs of grating couplers in cascade with a length of waveguide was obtained. Different grating designs were fabricated and tested. A red shift was consistently observed by increasing the width of the grating ridges and the grating pitch, in agreement with trends predicted by numerical modelling [25]. The bulk sensing measurement was performed using solutions with different refractive indices ranging from n = 1.3340 to n = 1.3360 and a limit of detection of 4×10^{-6} RIU was obtained. Surface sensing measurement was conducted using BSA dissolved in buffer solution. An Au waveguide in conjunction with a Pt electrode were used to perform cyclic voltammetry measurements at different scan rates as a proof of concept confirming that the device is also capable of electrochemical sensing.

REFERENCES

[1] P. Berini, "Long-range surface plasmon polaritons," Adv. Opt. Phot. **1**, 484−588 (2009).

[2] P. Berini, "Bulk and surface sensitivities of surface plasmon waveguides," New J. Phys. **10**, 105010 (2008).

[3] R. Slavik, J. Homola, "Ultrahigh resolution long range surface plasmon-based sensor," Sens. Act. B **123**, 10-12 (2007).

[4] J. Dostálek, A. Kasry, and W. Knoll, "Long Range Surface Plasmons for Observation of Biomolecular Binding Events at Metallic Surfaces," Plasmonics **2**, 97–106 (2007).

[5] O. Krupin *et al*., "Biosensing using straight long-range surface plasmon waveguides," Opt. Exp. **21**, 698-709 (2013).

[6] M. Khodami, P. Berini, "Biomolecular kinetics analysis using long-range surface plasmon waveguides," Sens. Act. B **243** 114-120 (2017).

[7] M. Khodami, P. Berini, "Low detection limits using sandwich and inhibition assays on long-range surface plasmon waveguide biosensors," Sens. Act. B **273**, 1156-1161 (2018).

[8] W. R. Wong, P. Berini, "Integrated multichannel Young's interferometer sensor based on long-range surface plasmon waveguides," Opt. Exp. **27**, 25470-25484 (2019).

[9] J. Homola, "Surface plasmon resonance sensors for detection of chemical and biological species," Chem. Rev. **108**, 462–493 (2008).

[10] D. Duval, *et al*., "Grating couplers integrated on Mach-Zehnder interferometric biosensors operating in the visible range," IEEE Photon. J., **5** (2013).

[11] J. Lu, C. Petre, E. Yablonovitch, and J. Conway, "Numerical optimization of a grating coupler for the efficient excitation of surface plasmons at an Ag-SiO_2 interface," J. Opt. Soc. Am. B **24**, 2268–2272 (2007).

[12] I. P. Radko, S. I. Bozhevolnyi, G. Brucoli, L. Martín-Moreno, F. J. García-Vidal, and A. Boltasseva, "Efficiency of local surface plasmon polariton excitation on ridges," Phys. Rev. B **78**, 115115 (2008).

[13] I. P. Radko, S. I. Bozhevolnyi, G. Brucoli, L. Martín-Moreno, F. J. García-Vidal, and A. Boltasseva, "Efficient unidirectional ridge excitation of surface plasmons," Opt. Exp. **17**, 7228–7232 (2009).

[14] J. Andkjear, S. Nishiwaki, T. Nomura, O. Sigmund, "Topology optimization of grating couplers for the efficient excitation of surface plasmons," J. Opt. Soc. Am. B **27**, 1828-1832 (2010).

[15] Y. Bao *et al*., "Efficient unidirectional launching of surface plasmons by multi groove structure," Plasmonics **12**, 1425-1430 (2017).

[16] C. Chen, P. Berini, "Grating couplers for broadside input and output coupling of long range surface plasmons," Opt. Exp. **18,** 8006-8018 (2010).

[17] N. R. Fong, P. Berini, "Characterization of grating-coupled long range surface plasmon polariton membrane waveguides," Opt. Exp. **23**, 17421-17430 (2015).

[18] Z. Hirbodvash *et al*., "Grating couplers fabricated by e-beam lithography for long-range surface plasmon waveguides embedded in a fluoropolymer," Appl. Opt. **58**, 2994-3002 (2019).

[19] Asahi Glass Company. CYTOP Technical Brochure [Online]; http://www.agc.com

[20] Chemours company, Teflon Technical Brochure [online]; www.chemours.com

[21] V. N. Konopsky, E. V. Alieva, "Long-Range Propagation of Plasmon Polaritons in a Thin Metal Film on a One-Dimensional photonic crystal surface," Phys. Rev. Lett. **97**, 253904-253907 (2006).

[22] E. V. Alieva, V. N. Konopsky, "Photonic crystal surface waves for optical biosensors," Anal. Chem. **79**, 4729−4735 (2007).

[23] A. Delfan, I. Degli-Eredi, J. E. Sipe, "Long-range surface plasmons in multilayer structures," J. Opt. Soc. Am. B **32**, 1615−1623 (2015).

[24] N. R. Fong *et al*., "Bloch Long-Range Surface Plasmon Polaritons on Metal Stripe Waveguides on a Multilayer Substrate," ACS Photon. **4**, 593-599 (2017).

[25] M. Khodami, P. Berini, "Grating couplers for (Bloch) long-range surface plasmons on metal stripe waveguides," J. Opt. Soc. Am. B **36**, 1921-1930 (2019).

[26] J. G. Gordon, S. Ernest, "Surface plasmons as a probe of the electrochemical interface," Surf. Sci. **101**, 499-506 (1980).
[27] X. Huang, *et al*., "Flow-through electrochemical surface plasmon resonance: detection of intermediate reaction products," J. Electroanal. Chem. **649**, 37-41 (2010).
[28] S. Patskovsky, A.-M. Dallaire, M. Meunier, "Electrochemical surface plasmon resonance sensing with absorptive redox mediator film," Sens. Act. B **222**, 71-77 (2016).
[29] C. Piraud, *et al.*, "Optoelectrochemical thin film chlorine sensor employing evanescent fields on planar optical waveguides," Anal. Chem. **64**, 651-655 (1992).
[30] A. Baba, *et al.*, "Electrochemical surface plasmon resonance and waveguide enhanced glucose biosensing with N-Alkylaminated polypyrrole/Glucose oxidase multilayers," Appl. Mater. Int. **2**, 2347-2354 (2010).
[31] J. C. Abanulo, R. D. Harris, A. K. Sheridan, J. S. Wilkinson, P. N. Bartlett, "Waveguide surface plasmon studies of surface reactions on gold electrodes," Faraday Discuss. **121**, 129-152 (2002).
[32] T. Sannomia, H. Dermutz, C. Hafner, J. Voros, A. B. Dahilin, "Electrochemistry on a localized surface plasmon sensor," Langmuir **26**, 7619-7626, (2010).
[33] H. H. Shin, *et al.*, "Chemical reactions driven by plasmon induced hot carriers," Appl. Mater. Today **16**, 112-119 (2019).
[34] Y. H. Jang, Y. J. Jang, S. Kim, L. N. Quan, K. Chung, D. H. Kim, "Plasmonic solar cells: from rational design to mechanism overview," Chem. Rev. **116**, 14982–15034 (2016).
[35] H. A. Atwater, A. Polman, "Plasmonics for improved photovoltaic devices," Nat. Mater. **9** 205 (2010).
[36] S. Linic, U. Aslam, C. Boerigter, M. Morabito, "Photochemical transformations on plasmonic metal nanoparticles," Nat. Mater. **14**, 567 (2015).
[37] N. Wu, "Plasmonic metal–semiconductor photocatalysts and photoelectrochemical cells: a review," Nanoscale **10**, 2679–2696 (2018).
[38] Y. J. Jang, K. Chung, J. S. Lee, C. H. Choi, J. W. Lim, D. H. Kim, "Plasmonic hot carriers imaging: promise and outlook," ACS Photonics **5** 4711–4723 (2018).
[39] H. Robatjazi, S. M. Bahauddin, C. Doiron, I. Thomann, "Direct plasmon-driven photo-electrocatalysis," Nano Lett. **15**, 6155–6161 (2015).
[40] Z. Liu, W. Hou, P. Pavaskar, M. Aykol, S. B. Cronin, "Plasmon resonant enhancement of photocatalytic water splitting under visible illumination," Nano Lett. **11**, 1111–1116 (2011).
[41] S. Yu, A. J. Wilson, J. Heo, P. K. Jain, "Plasmonic control of multi-electron transfer and C–C coupling in visible-light-driven CO_2 reduction on Au nanoparticles," Nano Lett. **18,** 2189–2194 (2018).
[42] G. Kumari, X. Zhang, D. Devasia, J. Heo, P. K. Jain, "Watching visible light-driven CO_2 reduction on a plasmonic nanoparticle catalyst," ACS Nano **12**, 8330–8340 (2018).
[43] P. Yeh, "Optical waves in layered media," Wiley (1988).
[44] M. Khodami *et al*., "Reactive Ion Etching of Cytop and Investigation of Residual Microstructure," J. Microelectromech. Sys. **29**, 228-235 (2020).
[45] M. Asif *et al*., "Wafer-Bonded Surface Plasmon Waveguide Sensors with In-Plane Microfluidic Interfaces," J. Micromech. Microeng., doi.org/10.1088/1361-6439/ab92e9 (2020).

Supplementary material

Edge metallisation

A process to metallise the edges (end-facets) of diced chips was developed and attempted to stablish contact to pads buried under the Borofloat wafer bonded lid. Chips were mounted in a metallic holder designed to hold the chips at an angle, then covered by a metal shadow mask incorporating 100 μm wide rectangular slits. The angled alignment provides partial access to the top of the glass as well as to the side of the chips. The chips were then mounted in the evaporator, where 5 nm of Ti (adhesion), followed by 800 nm of Cu (contact) and 50 nm of Au (cap) were evaporated, forming a contact pad on top of the glass lid, connected along the chip edge to the planar contact pads connected to the Au and Pt stripes buried under the glass lid. These contact pads provide electrical access to the Au and Pt stripes on chip. The contact pads also cover part of the supporting Si wafer, so cuts were made using a focussed ion beam (FIB) system (Zeiss Orion FIB system) to partially remove the metal (and avoid shorting by the Si substrate). The chip was exposed to a 5.57 nC/μm^2 Ga beam, using 300 μm aperture, 7 nA beam current, 10 nm step size and 10 μs dwell time to create a 5 μm × 10 μm cuts.

Figs. 11(a) and 11(b) show He FIB images and Figs. 11(c) and 11(d) show optical microscope images of the cross-section and top of a chip with metal stripes produced in this manner. As is evident from these images, the Cytop upper cladding is etched down to the contact pads, allowing electrical access from the side opening. Several trials of this process have been completed, but good contacts have yet to be achieved, possibly due to the excessive roughness of the facets post dicing.

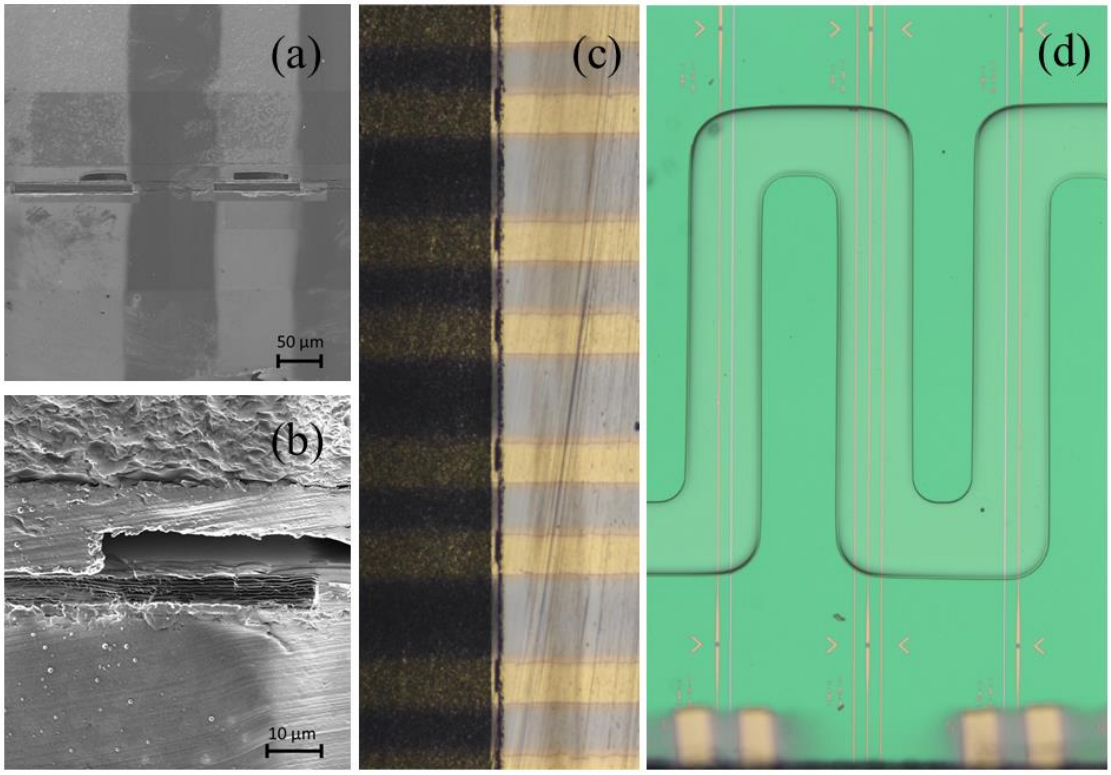

Fig. 11. (a) He FIB image of the cross-section of a chip with metal stripes evaporated partially on top of the glass cover and on the sidewall of the chip, using a shadow mask. The image also shows the openings that are etched through the Cytop upper cladding. A cut is made to isolate the metal stripes from the supporting (conductive) Si wafer. (b) zoomed in He FIB image showing the opening of the contact pad and the FIB cut with the exposed multilayer underneath. (c) Optical microscope image of the side of the chip showing a series of evaporated stripes and contact pads openings. (d) Optical microscope image in top view of the chip showing Au and Pt stripes and microfluidic channels, as well as the evaporated metal pads.

Chapter 7

Reactive ion etching of Cytop and investigation of residual microstructures

7.1 Summary

Reactive ion etching of Cytop as the host material for microfluidic channels is presented in this chapter. Cytop was patterned and used as the upper cladding as well as the bonding material between the two wafers in optical biosensors based on Bloch long range surface plasmon waveguides, as described in Chapter 6. Different grades of Cytop are examined and compared in terms of post etching substrate roughness, using different mask materials and different RIE parameters. Fur-like structure was observed post Cytop etching which was investigated using atomic force microscopy (AFM) and scanning electron microscopy (SEM). The SEM tool employed to obtain the images is equipped with an X-ray detector, which can be used for energy dispersive X-ray spectroscopy. Energy dispersive X-ray spectroscopy (EDX or sometimes EDS) is an analytical technique used for elemental analysis of features being observed under SEM. The sample is subjected to a focused beam of electrons which excites the inner shell electrons of the sample. This creates an electron hole which will be subsequently filled by an outer shell electron. The difference in energy between the higher energy shell and the lower energy shell is released in the form of an X-ray. EDX allows the elemental analysis of the samples since the X-ray characteristics depends on the atomic structure of the elements which is specific to each. The nature

of the residual micro-structure was consequently determined using EDX and a comprehensive acid clean procedure was proposed to remove the residue post Cytop etching.

7.2 Contribution

The results provided in this chapter are published in ***IEEE Journal of Microelectromechanical Systems***, Volume 29, Issue 2, 2020. Maryam Khodami initiated the study by performing AFM, SEM and EDX analysis on the fabricated samples. Maryam Khodami, Howard Northfield and Pierre Berini designed the experiments. Maryam Khodami and Howard Northfiled contributed to sample preparation, etching and analysis of different Cytop test samples, different mask materials and different RIE recipes. Maryam Khodami and Ewa Lisicka-Skrek contributed to the acid clean process development. Maryam Khodami interpreted the results and wrote the manuscript. Pierre Berini and Niall Tait contributed to the interpretation of the results and revised the manuscript.

7.3 Article

The article follows here verbatim.

Reactive Ion Etching of Cytop and Investigation of Residual Microstructures

Maryam Khodami, Howard Northfield, Ewa Lisicka-Skrzek, R. Niall Tait, and Pierre Berini, *Fellow, IEEE*

***Abstract*— Reactive Ion Etching (RIE) of Cytop as the cladding material for optical waveguides and microfluidic channels is investigated. Different grades of Cytop (M, A and S), different mask materials including photoresist and metals, different RIE parameters, along with different substrate materials were investigated. Grass-like structure was observed at the bottom of etched channels, of height that depends on the etching process parameters. A comprehensive post-etch acid cleaning procedure was devised to effectively remove the grass structure. [2019-0232]**

***Index Terms*— CYTOP, reactive ion etching, SEM, EDX, AFM, microfluidic channels, MEMS, optical waveguides.**

I. Introduction

KNOWLEDGE of etch rates of different materials is crucial in micro-fabrication processes to achieve a good etch selectivity. This is especially important for the selection of the mask material, where a high ratio of the etch rate of the target material to the etch rate of the mask material is desirable. Etch rates for many polymers and metals are reported in the literature, with some studies being focused on specific materials, and others addressing a variety of target materials and etchants [1]. Among all, only a few reports are dedicated to perfluorinated polymers, *e.g.*, Cytop™ or PTFE [2]. Cytop™ is a fluoropolymer commercialized by AGC chemicals [3]. It is a highly transparent polymer with a refractive index close to water and a glass transition temperature of $T_g = 108$ °C. It is resistant to most acids and bases, but can be dissolved with a special fluorinated solvent (CT-solve) [3]. Compared to other common fluorocarbon polymers such as poly-tetra-fluoro- ethylen "PTFE" (or Teflon) [4], Cytop has a non-crystalline structure with extremely high optical transmission.

Manuscript received October 11, 2019; revised November 22, 2019; accepted December 6, 2019. Date of publication January 9, 2020; date of current version April 2, 2020. Subject Editor N. Quack. *(Corresponding author: Maryam Khodami.)*

M. Khodami is with the Center for Research in Photonics, University of Ottawa, Ottawa, ON K1N 6N5, Canada, and also with the School of Electrical Engineering and Computer Science, University of Ottawa, Ottawa, ON K1N 6N5, Canada (e-mail: [redacted]).

H. Northfield and E. Lisicka-Skrzek are with the Center for Research in Photonics, University of Ottawa, Ottawa, ON K1N 6N5, Canada.

R. N. Tait is with the Department of Electronics, Carleton University, Ottawa, ON K1S 5B6, Canada.

P. Berini is with the Center for Research in Photonics, University of Ottawa, Ottawa, ON K1N 6N5, Canada, also with the School of Electrical Engineering and Computer Science, University of Ottawa, Ottawa, ON K1N 6N5, Canada, and also with the Department of Physics, University of Ottawa, Ottawa, ON K1N 6N5, Canada.

Color versions of one or more of the figures in this article are available online at http://ieeexplore.ieee.org.

Digital Object Identifier 10.1109/JMEMS.2019.2959262

Three types of Cytop are available for microfabrication via spin-coating processes: "A-grade" (*e.g.*, CTX-809A), "S-grade" (*e.g.*, CTX-809S) and "M-grade" (*e.g.*, CTL-809M), based on the additives incorporated therein [3]. Cytop M-grade provides adhesion to metal and glass surfaces through an amino-silane coupling agent, and can be used as an adhesion promoter for other Cytop grades. Cytop A-grade has a carboxyl additive that is reactive with other coupling agents and is highly transparent in the visible region of the spectrum, while Cytop S-grade has no additives, is referred to as optical grade, and is highly transparent from the deep ultraviolet (DUV) to the near infrared (IR) range.

Cytop has a broad range of applications due to its unique properties, including its water repellency, chemical resilience, optical transparency and low dielectric constant. It has been used as gate insulator for organic field effect transistors [5]–[11], and as a low-k dielectric layer integrated with power GaAs-based enhancement mode pseudomorphic high electron mobility transistors (pHEMTs) to improve the gain and output power [12]. Cytop is also used as Deep UV LED encapsulant to improve the stability of the device [13], and also to improve light extraction [14], [15]. Cytop has been incorporated as a soft pellicle polymer in photo-masks and other photolithography applications to optimize production yield in semiconductor manufacturing [16]–[18]. Cytop has wide application as the cladding material for plasmonic waveguide biosensors, and as the host material into which microfluidic channels are etched [19]–[24]. Cytop is a MEMS-friendly charge electret in energy harvesting materials [2], [25], and was also used in MEMS packaging as an intermediate layer to bond substrates of different materials in adhesive wafer bonding processes - Cytop adhesive bonding requires a low bonding temperature (150 – 200 °C) which decreases the risk of damage to thermally-sensitive devices during the bonding process [26]–[28]. Cytop was used as a guiding layer in a refractive index sensor with Teflon as the cladding material [29], and in THz waveguide applications [30]. An inorganic film (such as SiO_2 or Si_3N_4) was embedded in Cytop as the cladding for waveguide-based evanescent field microscopy [31]. The use of Cytop as a resist for damage-free electron-beam patterning of organic semiconductors was reported in [32].

In this study we propose and systematically assess different Cytop reactive ion etching (RIE) processes for use with different mask materials (including metal and photoresist), and different grades of Cytop. Substrate roughness caused by grass-like residue was generally observed post-etching via

AFM and SEM scans, and the composition of the residue determined using EDX analysis. Etch residue may be nefarious to many applications, so a comprehensive acid / UV ozone cleaning process was developed to remove the residue.

II. Experimental Results

A. Sample Preparation

Si and multilayer dielectric wafers (composed of alternating layers of SiO_2 and Ta_2O_5 on Si), un-patterned or bearing thin metallic features (~35 nm Au), were covered with Cytop as the host material into which microfluidic channels were etched. Cytop has a refractive index close to water, which makes it suitable for optical biosensing applications, because fluidic channels become optically non-invasive once filled with an index-matched aqueous sensing solution. The multilayer substrate bearing Au features is of interest to support Bloch long-range surface plasmon-polaritons within the bandgap of the structure [24], but its relevance here is to present different surfaces (Au, SiO_2) on which to assess the proposed etch processes. The roughness of the starting wafer surfaces was determined to be around 1 nm (RMS) in all cases. Cytop M grade (CTL-809M), Cytop S grade (CTX-809 SP2) and Cytop A grade (CTX-809A) were used specifically – Cytop A and S are known to adhere poorly to Si and SiO_2.

Amino-Propyl-Tri-Ethoxy-Silane (APTES) was used as an adhesion promoter for the application of Cytop A to a substrate, by coupling to the carboxyl additive of Cytop A [3], [33]. Specifically, 50 ml of a 0.05% solution of APTES in ethanol was prepared in a N_2 purged glove box chamber to avoid O_2 exposure. Wafers were submerged for 10 min in the 0.05% APTES solution, followed by 5 min in ethanol, followed by an ethanol spray rinse and an N_2 blow dry. The wafers were then removed from the glove box and immediately baked for 20 min at 115 °C. Throughout this work, all baking (including APTES, Cytop and resist layers), was performed using a contact hot plate. Immediately after baking, Cytop A was applied at a spin rate of 1500 rpm, and then baked at 50 °C for 30 min.

Alternatively, Cytop M was used in some cases as the first layer given its adhesive additive. Cytop M was spin coated at 3000 rpm to obtain a thickness of ~0.6 μm, then baked at 50 °C for 30 min. When fabricating multilayer Cytop stacks, several layers of bulk cladding, Cytop A or S, were applied at a spin rate of 1500 rpm. The thickness of each Cytop S or A layer was 2.0 μm or 2.4 μm per spin, respectively. Accordingly, a single layer of Cytop M and 4 layers of Cytop S gave a total thickness of 8.6 μm and a single layer of Cytop A and 4 layers of Cytop S gave a total thickness of 10.4 μm. Each layer post application was baked for 30 min at 50 °C to remove solvent. All single-layer and multilayer Cytop stacks were then ramp baked to 200 °C and held overnight to ensure the complete removal of solvent [3], [21], [22]. The integrity of the Cytop stack was not affected by heating above the glass transition temperature of Cytop. All Cytop A, S and M layers were spin-coated and cured following the details given in the Appendix. Direct application of Cytop S to a wafer does not adhere well, but was also examined to determine the effect of adhesion promoters post etch.

Etching was performed using a polymeric mask (photoresist, Megaposit SPR 220–7.0) or a metal mask (Al or Cr). The first step in the application of SPR 220 as an etch mask involved subjecting the Cytop to ashing in an isotropic O_2 plasma environment. The ashing was performed for 30 s at 50 W using an O_2 plasma etcher (Plasma Etch, model PE-50). Ashing roughens the Cytop surface to improve adhesion. The wafer was then primed with an adhesion layer of Hexa-methyl-disilazane (HMDS) in a YES-310TA HMDS vapor oven at 100 °C. SPR 220 was spin coated at 2300 rpm and post spin baked at 100 °C for 15 min. Exposure of SPR 220 to define the etch pattern was performed using a dark-field mask with an OAI 200IR contact mask aligner at 1000 mJ/cm^2 exposure energy. The exposed samples were left at room temperature overnight to allow the resist to evenly moisturize. The wafers were then subjected to a pre-development bake process including a ramp bake from room temperature to 100 °C, followed by baking at 115 °C for 90 s, and then cooling from 100 °C to room temperature. Photoresist development consisted of submersion in Megaposit MF-24A, a TMAH-based solution, for 5 min, followed by a DI water bath and rinse and a N_2 blow dry. The thickness of the SPR 220 mask was determined using a profilometer to be ~10 μm. The wafer was then cleaved into several pieces to be used as individual etch test samples.

Finally, Al and Cr metal masks were used to rule out the possibility of mask material (SPR 220) re-deposition in the RIE chamber. Following the procedure described above, Si or multilayer wafers were covered with 10 μm of Cytop. A lithography step using LOR 1A and Megaposit SPR 955-CM, was used to define the channels using a bright-field mask. LOR 1A was spin coated at 3000 rpm, then baked at 185 °C for 5 min. SPR 955 was spin coated at 6000 rpm and baked at 100 °C for 3 min. The wafers were exposed to 85 mJ/cm^2 UV light (i-line filtered) and developed for 1 min in a MF-CD 26 bath, followed by a DI water bath and rinse and a N_2 blow dry. A 30 nm thick layer of Al (or Cr) was evaporated using an e-beam process, and lifted-off using PG remover. The metal mask thus covered the entire wafer area except for the channel openings. In all cases the exposed Cytop was etched using the process described in the next section.

B. Etching Procedure

Anisotropic reactive ion etching was performed in a Samco 10-NR RIE system using different etch gases and parameters.

The Cytop and SPR 220 etch rates were determined during the same etch trials. First, the pre-etch thickness of the SPR 220 etch mask was required and determined through profilometry across lithographic features directly after mask development. Then, the amount of Cytop and mask material removed for a given etch time was determined through the procedure of timed etching, channel profilometry, mask removal using acetone, followed again by channel profilometry. Since, initially, all etch rates were unknown, a preliminary series of short 2 min etches was performed, with optical inspections carried out between etches to ensure that etch-to-substrate had not occurred. Once an approximate etch rate was determined,

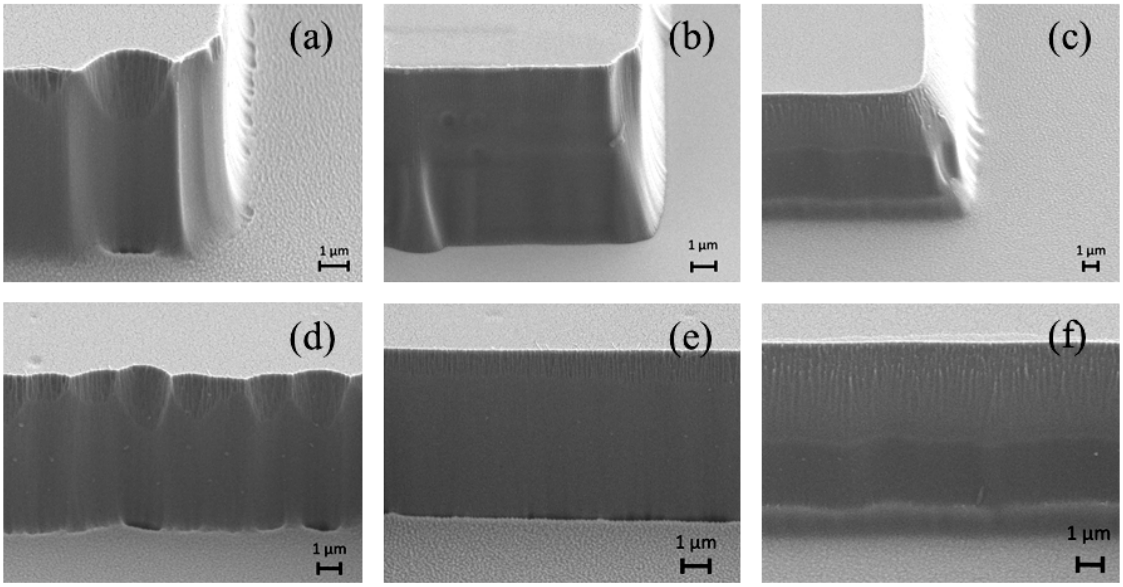

Fig. 1. SEM images of Cytop sidewalls etched using different RF powers: (a) and (d) 25 W, (b) and (e) 50 W, (c) and (f) 100 W. Cytop stack composed of 1 layer of of Cytop M and 4 layers of Cytop S was used in this case. SPR-220 was used as the mask material in this case.

longer continuous etches of the order of tens of minutes, were applied to give a more accurate etch rate. The total etch time was estimated such that $\sim$2 μm of the 8 μm initial Cytop thickness remained to avoid etching to substrate, as this would render the mask and Cytop etch rates invalid. Cracks occasionally formed in the SPR 220 mask, and would sometimes propagate through the Cytop stack. Cracks in the Cytop stack are undesirable as they compromise its integrity. The conditions leading to the formation of cracks are presently not well understood.

C. Analysis

Samples were analyzed with a Dektak profilometer, a Park NX-10 atomic force microscopy (AFM) system and a Zeiss Gemini 500 scanning electron microscope (SEM) equipped with an X-ray detector (Bruker Quantax EDS Xflash 6|60) which can be used for energy dispersive X-ray spectroscopy (EDX). A UV-Ozone system (Novascan, PDS series) was used to assist with post-etch cleaning. Profilometry was performed to determine the etch rates of the Cytop and SPR 220 mask. AFM was used to determine the post etch RMS roughness. SEM imaging was performed post etch to provide details of the Cytop surface, sidewalls and substrate, as well as elemental analysis using X-ray detection.

Etch rates of Cytop and SPR 220 using a preliminary etch process consisting of O_2 at a flow of 10 sccm, a pressure of 4 Pa, and different RF powers are provided in Table I, showing a slightly non-linear increase in etch rate with RF power. The Cytop stack in this case was composed of 1 layer of Cytop M and 4 layers of Cytop S and was partially etched (not down to substrate), for etch rate calculations. Etching with the SPR 220 masks resulted in sloped Cytop sidewalls (Fig. 1) as observed under SEM, due to a slope of $\sim 45°$ in the edge of the SPR 220 mask as determined by profilometry. Alternatively, etching with an Al or Cr mask resulted in vertical Cytop sidewalls (Fig. 2 c).

TABLE I

CYTOP AND SPR 220 RIE ETCH RATES (nm/min) FOR AN O_2 FLOW OF 10 SCCM, A PRESSURE OF 4 PA AND VARYING RIE POWER

RF POWER	25 W	50 W	100 W
CYTOP ETCH RATE	139	309	682
SPR 220 ETCH RATE	55	90	150

SEM analysis post etching indicates an inclined slope profile of the side walls, as shown in Fig. 1, observed to increase with increasing etching power. At 25 W, the surface roughness of the etched Cytop was 16 nm RMS as determined by AFM, and continued etching at 25 W to the substrate gave a roughness of 21 nm RMS, indicating the presence of etch residue at the bottom of the channel. Curtaining and rough channel edges are apparent in the 25 W etch. A pedestal-like feature is also apparent near the bottom of the sidewalls in the case of the 100 W etch. The 50 W etch seems to produce the smoothest sidewalls with the sharpest edges and no evidence of pedestal-like features near the bottom.

The same etch tests were repeated using an Al mask and the same Cytop stack was etched down to the substrate using the same etch recipe. Much larger roughness values of up to 200 nm RMS or more were observed along the substrate surface, and along the top surface of thin Au features located on this substrate, which indicates that the Al mask has no advantage over the photoresist mask from the standpoint of etch residue. The wafer was then inspected under SEM to visualize the residue, as shown in Fig. 2. Such inspections indicate that the substrate and Au features are covered with hair- or grass-like residue. The density of the residue varies over the etched surface of the substrate, which suggests an inhomogeneous plasma distribution in the RIE chamber. A metal mask can potentially affect the distribution of the plasma cloud (composed of charged ions) in the RIE chamber, which might subsequently affect the formation of

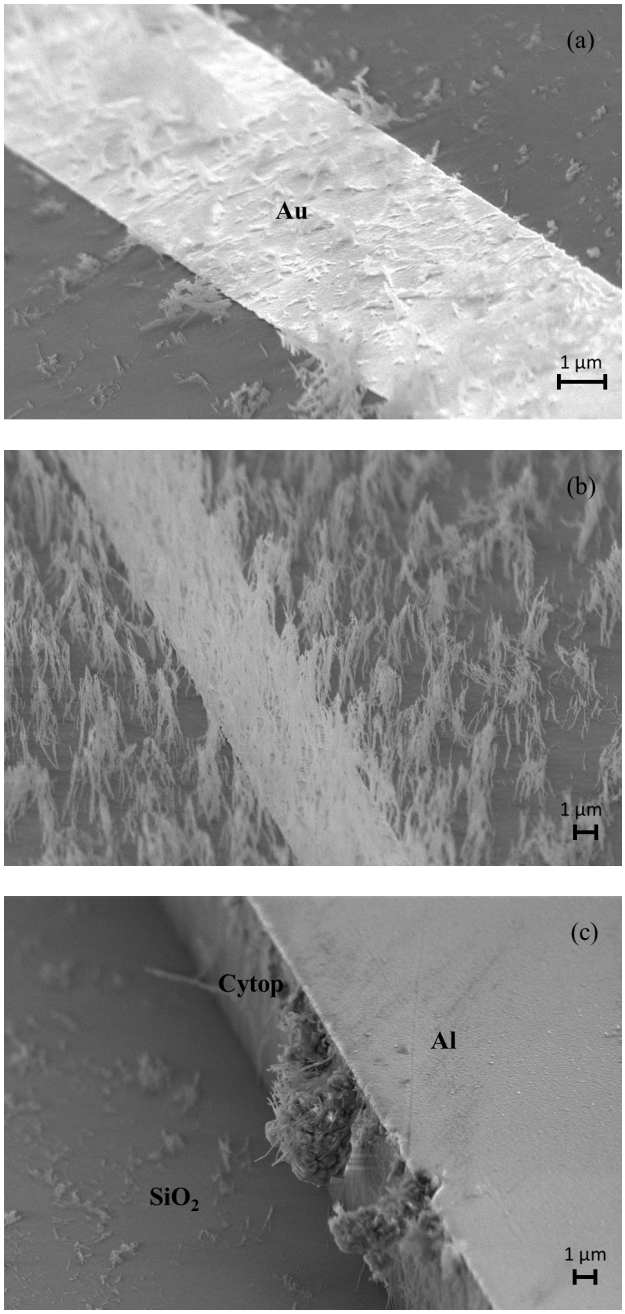

Fig. 2. SEM images of a substrate bearing thin (35 nm) Au features post Cytop etch, showing exposed Au features (a and b) as well as a sidewall (c). The wafer was masked with Al. Grass-like structure is observed on the Au features and inside the channel. The density of the grass-like structure varies across the wafer. Cytop stack consisting of 1 layer of Cytop M and 4 layers of Cytop S, as described in section A, was used in this case.

grass-like residue. Observation of grass-like structure post RIE etching was previously reported in the literature, especially when using an Al mask [2], [34], [35]. Conversely, using a Cr mask produced a much lower post-etch roughness (up to 13 nm RMS) compared to the Al mask (as high as 200 nm RMS), after etching the same material under the same RIE parameters; we attribute the lower roughness to less post-etch residue on the wafer.

EDX analysis was performed, post mask removal, to determine the chemical composition of the

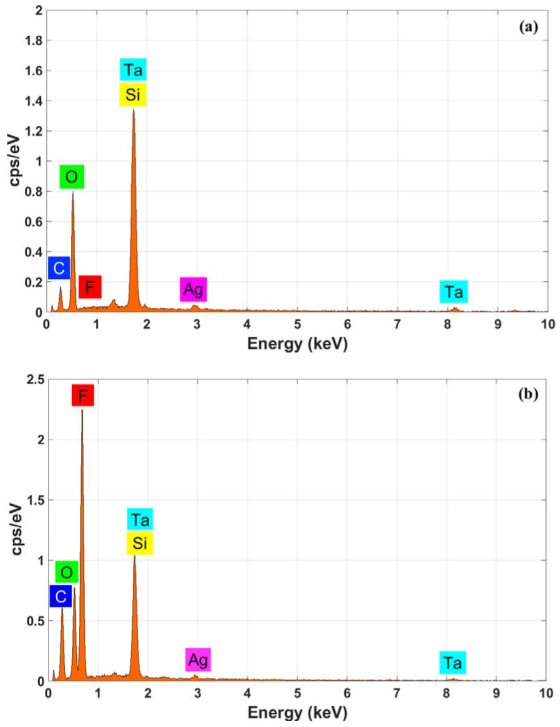

Fig. 3. EDX analysis of (a) the substrate, and (b) the Cytop stack, post etching and post mask removal. A Cytop stack composed of 1 layer of Cytop M and 4 layers of Cytop S was used in this case.

TABLE II
ETCH RECIPES AND MEASURED CYTOP AND SPR 220 ETCH RATES

RIE parameters \ Material	Cytop (nm/min)	SPR220 (nm/min)
Etch A: 10 sccm O_2, 4 Pa, 25 W	125	60
Etch B: 150 sccm O_2, 42.7 Pa, 100 W	230	155
Etch C: 5 sccm O_2, 20 sccm Ar, 4 Pa, 100 W	440	160

grass-like residue, as shown in Fig. 3. Elemental Oxygen (O), Fluorine (F), Carbon (C), Tantalum (Ta) and Si (Silicon), as well as silver (Ag), were observed inside and outside of the etched channel. The multilayer stack is likely the source of Ta and Si, as it is formed of alternating layers of Ta_2O_5 and SiO_2. Elemental oxygen, carbon and fluorine likely originate from Cytop as they are its constitutive elements. The source of silver is unknown and deemed to be a contaminant. The elemental map is shown in Fig. 4, from which the mass percentage of each element inside the etched channel is deduced as follows: Ta 29.34 %, C 9.56 %, Si 23.47%, O 33.24%, F 0.29%, Ag 3.18%. The mass percentage of each constitutive element outside of the channel is as follows: Ta 13.18 %, C 6.6 %, Si 11.9%, O 14.21%, F 47.04%, and Ag 1.45%, from which the distribution of the elements can be deduced.

Following observations of post-etch residue, different Cytop grades, stack compositions and adhesion methods were investigated, along with different mask materials and

TABLE III
MEASURED RESIDUAL ROUGHNESS (RMS) POST-ETCH

Cytop Grade / RIE recipe	APTES + 1×A (SPR 220 mask)	APTES + 1×A+4×S (SPR 220 mask)	1×M+4×S (SPR 220 mask)	5×S (SPR 220 mask)	1×S (Cr mask)	1×M+1×S (Cr mask)	1×S (SPR 220 mask)	1×M+1×S (SPR 220 mask)
Etch A	1 nm	36 nm	11.6 nm	1.6 nm	1.1 nm	11.8 nm	1.3 nm	6.8 nm
Etch B	1 nm	1.9 nm	5 nm	1.6 nm	1.9 nm	2.6 nm	1.1 nm	8.5 nm
Etch C	0.7 nm	0.9 nm	1.8 nm	1.8 nm	2.3 nm	13.2 nm	1.1 nm	4.4 nm

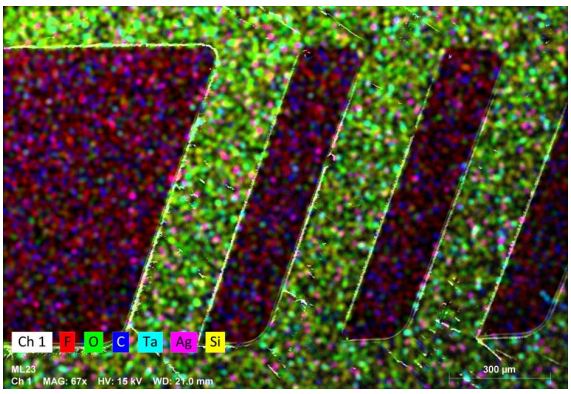

Fig. 4. Elemental map inside and outside of the etched microfluidic channel. Image obtained at a 45° tilt. A Cytop stack composed of 1 layer of Cytop M and 4 layers of Cytop S was used in this case.

RIE parameters, aiming to minimize post-etch residue as determined via substrate roughness. In some cases, APTES was used as the adhesion promoter with Cytop A, in other cases Cytop M was applied to the wafer directly given that it incorporates an adhesion promoter, and other cases applied Cytop S directly to the substrate as a control. We also compared Cr and SPR 220 mask materials. In all experimental trials, 3 different RIE processes were applied (gas flow rate, chamber pressure, RF power): Etch A consisted of 10 sccm O_2, 4 Pa, 25 W. Etch B consisted of 150 sccm O_2, 42 Pa, 100 W, to examine the effect of increasing gas flow rate, chamber pressure and RF power. Etch C consisted of 5 sccm O_2 with 20 sccm Ar, 4 Pa and 100 W, to examine the effects of a physically aggressive etch. The three RIE recipes are summarized in Table II along with the measured Cytop and SPR 220 etch rates. A Cytop stack consisting of 1 layer of Cytop M along with 4 layers of Cytop S was used in this case.

Table III summarizes the post-etch substrate roughness obtained after application of etches A, B and C to different stacks of Cytop and for different mask materials. The roughness of the starting wafer surfaces was < 1 nm RMS, so roughness values post-etch greater than 1 nm RMS generally indicate the presence of post-etch residue (assuming no etch damage to the substrate).

As can be seen from the first column of this table, the combination of Cytop A and APTES as an adhesion promoter, subjected to our three etch processes, results in roughness values that are comparable to those of the starting wafer surfaces. Very little post-etch residue evidently remains in these cases. Etch C has a physical character which produces a higher etch rate but harms delicate features that may be located on the substrate, such as the thin Au stripe shown in Fig. 2. From the second column, we note that a stack of Cytop S on Cytop A on APTES results in high roughness for Etch A, whereas Etches B and C produce essentially no residue.

Cytop stacks consisting of only Cytop S produce slight post-etch residue, as deduced from roughness values that range from 1 to 2 nm RMS, as listed in columns 4, 5 and 7. However, it should be noted that Cytop S applied directly to a Si or SiO_2 substrate will easily peel off. Much higher roughness values are observed when a layer of Cytop M is used as the first layer in a Cytop stack, as noted from the third, sixth and eight columns. Cytop M has an adhesion additive which may contribute to the creation of residue forming in the O_2 plasma within the chamber. The roughness values do not seem to depend on the mask material used (SPR 220 or Cr) for any of the cases investigated.

D. Cleaning Procedure

As our etch trials indicate, residue may form in etched channels to varying degrees depending on the Cytop stack being etched. Post etching residue and surface roughness are particularly important in applications where the surface plays an essential role, for instance as part of an optical waveguide or in biosensing applications where recognition chemistries are applied to the surface to detect target analyte molecules via chemisorption [19], [20], [23]. Cytop M seems more prone at producing residue when used as the first layer. A comprehensive post etch cleaning process, involving the use of Piranha solution (Peroxymonosulfuric acid) in combination with UV ozone cleaning was therefore developed to ensure the complete removal of residue from etched channels. Acid cleaning and UV ozone cleaning are effective cleaning methods in semiconductor wafer fabrication [36]. AFM scans of a 35 nm thick Au stripe, defined lithographically on a multilayer substrate, were used to monitor progress after application of each cleaning step.

A Cytop stack consisting of 1 layer of Cytop M and 4 layers of Cytop S, fabricated as described in Section A, was used as the material into which the microfluidic channels were etched. Etching was performed using Etch A and SPR-220 mask, and the remnants of the etch mask were removed using acetone. An AFM scan of a Au stripe and the substrate post RIE etch

TABLE IV
CYTOP UPPER CLADDING SPIN PROCEDURE

Step	Description	Details
1	Adhesive layer (CYTOP M grade coating and bake)	Spin coat CYTOP M-grade at 300 rpm/sec for 7 sec followed by 3000 rpm/sec for 30 sec. Bake at 50 C for 30 mins
2	Bulk layer (CYTOP S-grade or A grade coating and bake)	Spin coat CYTOP S-grade (or Cytop A-grade) at 200 rpm/sec for 3 sec followed by 1500 rpm/sec for 30 sec. Bake at 50 C for 30 mins. Repeat multiple times to achieve the desired cladding thickness
3	Hard bake	Ramp at 25 °C/hour to 200 °C and hold for 12 hours.

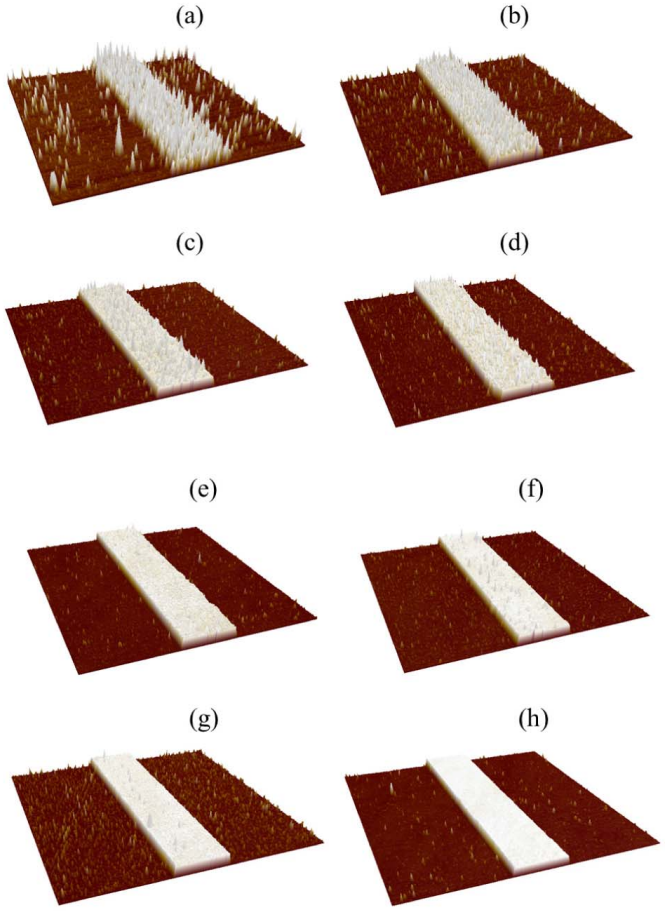

Fig. 5. AFM scans taken over a 25 × 25 μm^2 area (vertical scale of 400 nm) of a 35 nm thick Au stripe as the cleaning process evolves: (a) Post RIE etch; (b) post CD 26 clean; (c) post 1 min Piranha clean; (d) post 30 min UV ozone exposure; (e) post 1 min Piranha clean; (f) post 30 min UV ozone exposure; (g) post 1 min piranha clean; (h) post 2 min O_2 RIE etch.

of a channel and post mask removal is shown in Fig. 5(a). The roughness is very high, greater than 30 nm depending on the location on wafer, so significant residue is evidently present. Following this step, the wafer was subjected to a 10 min CD-26 bath, which reduced the amount of residue on the Au stripe and substrate, as noted in Fig. 5(b) - the roughness in this case was $R_q = 11$ nm RMS. This was followed by a 1 min Piranha cleaning step (H_2SO_4 and H_2O_2(4:1) at 90 °C), which removed more residue and reduced the roughness to $R_q = 7$ nm RMS (Fig. 5(c)). Subsequently, a 30 min UV ozone exposure was performed, which reduced the roughness to $R_q = 6$ nm RMS (Fig. 5(d)). The cleaning steps were repeated as follows: 1 min Piranha ($R_q = 4.5$ nm, Fig. 5(e)), 30 min UV ozone ($R_q = 5$ nm, Fig. 5(f)), 1 min Piranha ($R_q = 4$ nm, Fig. 5(g)). A 2 min O_2 reactive ion etch (10 sccm, 4 Pa, 100 W) was applied as the last step to remove any loose debris. The final roughness values on the Au stripe and substrate reduced to $R_q = 1.7$ nm and $R_q = 2$ nm, respectively (Fig. 5(h)).

It is surmised that exposure to UV breaks molecular bonds in the residue, and that ozone reacts with the remnant material potentially creating volatile species that are vented. The remnant residue then appears more susceptible to subsequent Piranha and O_2 cleans.

III. CONCLUSION

Reactive ion etching of Cytop as the cladding material for optical waveguides and as the host material for microfluidic channels was studied using different mask materials (Al, Cr, SPR 220), different RIE parameters and different grades of Cytop. Substrate roughness was investigated post Cytop etching, and residue and grass-like structures were observed under SEM. EDX analysis was performed to determine the source of the residue. A comprehensive acid and UV ozone cleaning procedure was developed to remove the residue.

Al masks are known to produce shadowing and micro-masking, leading to the formation of grass-like structure. A comparison between Al and Cr masks in this study showed that Cr produces much less residue compared to Al, suggesting less micro-masking effects. It was determined that physically aggressive etching using Argon is suitable for deep RIE applications, where the substrate or patterns thereon are not affected by physical characteristics of Argon etching.

APPENDIX

See Table 4.

ACKNOWLEDGMENT

The authors would like to thank M. Asif and A. Olivieri for their assistance.

REFERENCES

[1] K. R. Williams and R. S. Muller, "Etch rates for micromachining processing," *J. Microelectromech. Syst.*, vol. 5, no. 4, pp. 256–269, Dec. 1996.

[2] F. Wang *et al.*, "Reactive ion etching of polymer materials for an energy harvesting device," *Microelectron. Eng.*, vol. 97, pp. 227–230, Sep. 2012.

[3] Asahi Glass Company. *Cytop Technical Brochure*. [Online]. Available: http://www.agc.com

[4] Chemours Company. *Teflon Technical Brochure*. [Online]. Available: http://www.chemours.com

[5] X. Cheng *et al.*, "Air stable cross-linked cytop ultrathin gate dielectric for high yield low-voltage top gate organic filed-effect transistors," *Chem. Mater.*, vol. 22, no. 4, pp. 1559–1566, 2010.

[6] M. P. Walser, W. L. Kalb, T. Mathis, T. J. Brenner, and B. Batlogg, "Stable complementary inverters with organic field-effect transistors on cytop fluoropolymer gate dielectric," *Appl. Phys. Lett.*, vol. 94, no. 5, 2009, Art. no. 053303.

[7] J. Roh *et al.*, "Fluorinated CYTOP passivation effects on the electrical reliability of multilayer MoS_2 field-effect transistors," *Nanotechnology*, vol. 26, no. 45, 2015, Art. no. 455201.

[8] W. L. Kalb, T. Mathis, S. Haas, A. F. Stassen, and B. Batlogg, "Organic small molecule field-effect transistors with cytop gate dielectric: Eliminating gate-bias stress effect," *Appl. Phys. Lett.*, vol. 90, no. 9, 2007, Art. no. 092104.

[9] T. Umeda, D. Kumaki, and S. Tokito, "High air stability of threshold voltage on gate bias-stress on pentacene TFTs with a hydrogel-free and amorphous fluoropolymer as gate insulators," *Organic Electron.*, vol. 9, no. 4, pp. 545–549, 2008.

[10] S. Sun *et al.*, "Stable ambipolar organic-inorganic heterojunction field-effect transistors and inverters with cytop interlayer," *RSC Adv.*, vol. 7, no. 10, pp. 5966–5969, 2017.

[11] S.-H. Choi, J.-H. Jang, J.-J. Kim, and M.-K. Han, "Low-temperature organic (CYTOP) Passivation for improvement of electric characteristics and reliability in IGZO TFTs," *IEEE Electron Device Lett.*, vol. 33, no. 3, pp. 381–383, Mar. 2012.

[12] C. H. Lin *et al.*, "Performances of CYTOP low-*k* dielectric layer bridged GaAs-based enhancement mode pHEMT for wireless power application," *Solid-State Electron.*, vol. 49, no. 10, pp. 1708–1712, 2005.

[13] R. Liang *et al.*, "Interface anchored effect on improving working stability of deep ultraviolet light-emitting diode using graphene oxide-based fluoropolymer encapsulant," *ACS Appl. Mater. Interfaces*, vol. 10, no. 9, pp. 8238–8244, 2018.

[14] R. Liang *et al.*, "Bioinspired flexible fluoropolymer film for all mode light extraction enhancement," *ACS Appl. Mater. Interfaces*, vol. 11, no. 21, pp. 19623–19630, 2019.

[15] Y. Peng, "Fabrication of microlens arrays with controlled curvature by micromolding water condensing based porous films for deep ultraviolet LEDs," *ACS Photon.*, vol. 4, no. 10, pp. 2479–2485, 2017.

[16] A. Tregub, F. Eschbach, F. C. Lo, and S. Hull, "Process to optimize properties of polymer pellicles and resist for lithography applications," U.S. Patent Appl. 1 079 943, Jan. 2008.

[17] R. H. French *et al.*, "Materials design and development of fluoropolymers for use as pellicles in 157-nm photolithography," *Proc. SPIE*, vol. 4346, Sep. 2001, Art. no. 435710.

[18] F. Schabach *et al.*, "Photomask lifetime issues in ArF lithography," *Proc. SPIE*, vol. 5853, Jun. 2005, Art. no. 617078.

[19] M. Khodami and P. Berini, "Biomolecular kinetics analysis using long-range surface plasmon waveguides," *Sens. Actuators B, Chem.*, vol. 243, pp. 114–120, May 2017.

[20] M. Khodami and P. Berini, "Low detection limits using sandwich and inhibition assays on long-range surface plasmon waveguide biosensors," *Sens. Actuators B, Chem.*, vol. 273, pp. 1156–1161, Nov. 2018.

[21] S. Hassan, M. Khodami, R. N. Tait, and P. Berini, "Fabrication of long-range surface plasmon-polariton Bragg gratings with microfluidic channels in cytop claddings," *Microelectron. Eng.*, vol. 135, pp. 38–44, Mar. 2015.

[22] Z. Hirbodvash *et al.*, "Grating couplers fabricated by e-beam lithography for long-range surface plasmon waveguides embedded in a fluoropolymer," *Appl. Opt.*, vol. 58, no. 11, pp. 2994–3002, 2019.

[23] M. Khodami and P. Berini, "Grating couplers for (Bloch) long-range surface plasmons on metal stripe waveguides," *J. Opt. Soc. Amer. B, Opt. Phys.*, vol. 36, no. 7, pp. 1921–1930, 2019.

[24] W. R. Wong and P. Berini, "Integrated multichannel Young's interferometer sensor based on long-range surface plasmon waveguides," *Opt. Express*, vol. 27, no. 18, pp. 25470–25484, 2019.

[25] T. Tsutsumino, Y. Suzuki, N. Kasagi, and Y. Sakane, "Seismic power generator using high-performance polymer electret," in *Proc. 19th IEEE Int. Conf. Micro Electro Mech. Syst.*, Jan. 2006, pp. 98–101.

[26] K. W. Oh, A. Han, S. Bhansali, and C. H. Ahn, "A low-temperature bonding technique using spin-on fluorocarbon polymers to assemble microsystems," *J. Micromech. Microeng.*, vol. 12, no. 2, pp. 187–192, 2002.

[27] V. Patil and C. B. O'Neal, "Adhesive strength characterization of cytop: Low temperature wafer level packaging," in *Proc. IMEC*, vol. 14791, 2006, pp. 335–339.

[28] C.-W. Tsao and D. L. DeVoe, "Bonding of thermoplastic polymer microfluidics," *Microfluidics Nanofluidics*, vol. 6, no. 1, pp. 1–16, 2009.

[29] B. Hooda and V. Rastogi, "Low cost highly sensitive miniaturized refractive index sensor based on planar waveguide," *Optik*, vol. 143, pp. 158–166, Aug. 2017.

[30] A. Quema *et. al*, "Low loss single mode terahertz waveguiding using cytop," *Appl. Phys. Lett.*, vol. 89, no. 1, 2006, Art. no. 211119.

[31] B. Agnarsson, M. Mapar, M. Sjöberg, M. Alizadehheidari, and F. Höök, "Low-temperature fabrication and characterization of a symmetric hybrid organic–inorganic slab waveguide for evanescent light microscopy," *Nano Futures*, vol. 2, no. 2, 2018, Art. no. 0025007.

[32] J. Park *et al.*, "Direct top–down fabrication of nanoscale electrodes for organic semiconductors using fluoropolymer resists," *Appl. Phys. A, Solids Surf.*, vol. 111, no. 4, pp. 1051–1056, 2012.

[33] P. Ren, O. Krupin, P. Berini, and R. N. Tait, "Fabrication of long range surface plasmon waveguide biosensors in a low-index fluoropolymer," *J. Vac. Sci. Technol. B, Microelectron.*, vol. 36, no. 4, 2018, Art. no. 042601.

[34] S. Joshi, A. Savov, S. Shafqat, and R. Dekker, "Investigation of 'fur-like' residues post dry etching of polyimide using aluminum hard etch mask," *Mater. Sci. Semicond. Process.*, vol. 75, pp. 130–135, Mar. 2018.

[35] T. L. Tsang, C. Miller, and T. Lii, "Investigation of polyimide residue due to reactive ion etching in O_2," *J. Electrochem. Soc.*, vol. 143, no. 4, pp. 1464–1469, 1996.

[36] W. Kern, *Handbook of Semiconductor Wafer Cleaning Technology*. Park Ridge, NJ, USA: Noyes, 1993.

Maryam Khodami received the B.Sc. degree in electrical engineering from the Isfahan University of Technology, Isfahan, Iran, and the M.Sc. degree in electrical and computer engineering from the University of Ottawa, Ottawa, ON, Canada, where she is currently pursuing the Ph.D. degree in electrical and computer engineering with the Center for Research in Photonics. Her research interests include theoretical and experimental optics and photonics, plasmonics, micro/nano fabrication, and biosensing. She was a recipient of Ontario Graduate Scholarship (OGS) and Excellence Scholarship in 2016 and 2017, respectively.

Howard Northfield received the B.Sc. degree in physics/geology from Queen's University, Kingston, Ontario, Canada, and the B.Eng. degree in electrical engineering and the M.A.Sc. degree in computer and electrical from Carleton University, Ottawa, Canada. He is currently a Research Engineer with the Center for Research in Photonics, University of Ottawa.

Ewa Lisicka-Skrzek worked for four years at MetroPhotonics as the Director of Post Processing and Assembly and for ten years at Communication Research Centre, and agency of Industry Canada as an Optoelectronics Technologist. She is currently a Lab Manager and an Optical Technologist with the Center for Research in Photonics, University of Ottawa. She assisted with the development of many processes for the fabrication of new optoelectronic components and circuitry (GaAs/AlGaAs HBT, MSM photodetector, and quantum well) and novel waveguide devices, including plasmon-polariton optical waveguides.

R. Niall Tait received the Ph.D. degree in electrical engineering from the University of Alberta, Edmonton, AB, Canada. Following completion of his Ph.D., he joined the Alberta Microelectronic Centre (now Micralyne) as a Research Scientist working on silicon micro-electro-mechanical systems (MEMS) and thin-film technology. He worked with domestic and international clients on projects including modeling IC metallization, design and fabrication of MEMS microphones, and fabrication of lab-on-chip microfluidic devices. Since moving to Carleton University, Ottawa, ON, Canada. He is currently a Professor with the Department of Electronics, Carleton University. His research program has included MEMS and microfabrication of semiconductor sensors, RF and microwave components, and integrated optical devices including micro-bolometers and infrared devices.

Pierre Berini (F'11) received the B.E.Sc. and B.Sc. degrees in electrical engineering and computer science from the University of Western Ontario, Canada, and the M.Sc.A. and Ph.D. degrees in electrical engineering from the École Polytechnique de Montréal, Canada.

He is currently a Distinguished University Professor of electrical engineering and of physics, a University Research Chair in Surface Plasmon photonics, and the Director of the Centre for Research in Photonics, University of Ottawa. He was the Founder and the Chief Technology Officer of a venture capital financed company. He collaborates on an ongoing basis with industry. He has published 12 book chapters, approximately 500 scientific and technical articles in peer-reviewed periodicals and conference proceedings. He is an Inventor or a Co-Inventor on 23 patents. He contributes on an ongoing basis to the organization of several international conferences in photonics. His research interests span many areas of optics and photonics, with surface plasmons and their applications being of particular current interest.

Dr. Berini is a Fellow of the OSA, the Canadian Academy of Engineering, and the Royal Society of Canada. He has received an NSERC Steacie Fellowship, an NSERC Discovery Accelerator, a Premier of Ontario Research Excellence Award (PREA), the University of Ottawa Young Researcher of the Year Award, an URSI Young Scientist Award, and a George S. Glinski Award for Excellence in Research. He is a Canada Foundation for Innovation Researcher. He was an Associate Editor of *Optics Express* and a Managing Editor of *Nanophotonics*.

Chapter 8

Conclusions and perspectives

8.1 Conclusions

In the present work, a novel, cost effective and label free optical biosensor based on (Bloch) long range surface plasmon waveguides was presented. Straight Au waveguides on a Cytop lower cladding, supporting LRSPPs with an etched microfluidic channel were employed for the extraction of binding kinetics of biomolecular interactions. The device was also used for the demonstration of enhanced assay formats to achieve a limit of detection as low as 10 pg/ml in solution. Employing Cytop as the lower cladding material for waveguide biosensors involves fabrication complexities due to its low glass transition temperature (T_g = 108 ^oC).

A one-dimensional photonic crystal (1DPC) can replace the Cytop lower cladding to support Bloch LRSPPs over a limited range of wavenumber and wavelength. Motivated by quality issues with the end facet of such structure, we used grating couplers as the input/output excitation means, where a Gaussian beam emerging from an aligned polarisation-maintaining single mode fibre excites Bloch LRSPPs on a Au waveguide on a 1DPC. The design space of such a grating coupler structure was explored theoretically using 2D FEM and 3D FDTD electromagnetic modeling and the best performance was achieved for 10 μm long grating on an adiabatic flared stripe that can accommodate larger beam sizes. The device was fabricated using standard photolithography and

electron-beam lithography techniques and was characterized to obtain the wavelength response of the structure. The design space of such a structure was also investigated experimentally using a grating test wafer. Different grating designs were investigated to study the effect of changing the pitch and duty cycle of the structure. Finally, Bloch LRSPP waveguides incorporating grating couplers were integrated with Pt electrodes to form an electrochemical sensor. Planar waveguides were integrated into arrays capable of multichannel multimodal biosensing. The device was fabricated using photolithography and overlaid electron-beam lithography and was covered with Cytop as the upper cladding to create etched microfluidic channels and the sensing window over a portion of the waveguide. The wafer was capped with borofloat silica through wafer bonding to encapsulate the fluidic channels and enable side fluidic interfaces. Measured optical and electrochemical responses were obtained as a proof of concept.

Grass-like structure was observed post etching of the fluidic channels which motivated the use of different grades of Cytop along with different mask materials and different RIE parameters to address the issue. EDX analysis was performed to determine the nature of the grass structure and a comprehensive acid clean procedure was proposed to remove the residual microstructures.

8.2 Future work

Present work opens up new possibilities to address disease detection problems. Using an opto electrochemical joint biosensing platform, the detection of Human noroviruses, as the leading cause of viral gastroenteritis, could be addressed using LRSPP optical biosensors as well as electrochemical sensors. A decrease in redox current, as a result of virus binding to the immobilized surface, can be measured via voltammetry, while reporter molecules ($[Ru(NH_3)_6]^{3+}$

and $[Fe(CN)_6]^{3-/2}$) are used to monitor processes on the surface [103]. Hypocalcaemia which is caused by increasing parathyroid gland function could be detected using the optical biosensor portion to detect the Parathyroid hormone (PTH), and the electrochemical portion to detect Ca^{2+}. Hepatitis B and C detection could also be addressed using a multimodal strategy, with the LRSPP waveguide detecting Anti-HBV (Hepatites B) / Anti-HCV (Hepatite C) and the electrochemical sensors detecting enzymes aspartate transaminase/Alanine transaminase (ALT/AST). Our multimodal strategy combines immuno-sensing techniques with electrochemical detection enabling a disease to be detected by targeting different markers or by using distinct protocols for the same marker, thereby increasing the reliability of the measurement.

The LRSPP waveguide biosensor can also be used to detect Human thyroid stimulating hormone (hTSH) in blood. hTSH is a pituitary hormone that stimulates the thyroid gland to produce the thyroid hormones (thyroxin and triiodothyronine). The human body metabolism is stimulated by these hormones. Imbalance in the production of these hormones will result in thyroid diseases, including Hypothyroidism and Hyperthyroidism. According to the Thyroid Foundation of Canada, “200 million people, worldwide have some form of thyroid disease”. The causes of thyroid disease are mostly unknown but early diagnosis and treatment is crucial since undiagnosed disease may result in other serious conditions such as cardiovascular disease and infertility.

Since physiological concentrations of hTSH are low in blood, its detection requires high sensitivity, motivating the use of enhanced assays as discussed in Chapter 4. Alternatively, LRSPP Bragg gratings, consisting of a step-in-width Au stripe embedded in CYTOP, hold the promise of greater sensitivity by exploiting phase-based detection. Such a device has already been fabricated and tested in terms of its Bragg wavelength performance [57]. Future work aims at determining the bulk and surface sensitivities of the structure by flowing solutions of different refractive index

and by carrying out surface sensing experiments with a biospecific pair (i.e. hTSH and anti-hTSh). In such experiments the Bragg response will be shifted and the sensitivity of the system to bulk and surface refractive index changes can be measured. The narrow-measured bandwidth of the response and the predicted high sensitivity of gratings are promising for biosensing applications.

The integrated optics platform presented in this work can be further improved by optimizing the coupling conditions. Optimal coupling between the incident beam and the LRSPP mode of the waveguide can be achieved using a weak conformal grating and a non-normal incident beam as briefly discussed in Chapter 5. According to that, the design of the grating couplers could be optimized to achieve a coupling efficiency up to 90 %. [104] The reflectance *vs.* wavelength for this structure can be computed using rigorous coupled wave (RCW) approach. The fabrication procedure for such structure involves using interferometric lithography (IL) where the interference of two coherent light sources creates a sinusoidal pattern that can subsequently be transferred to the substrate. The Pt electrode geometry and dimensions could also be modeled and optimized by solving the Nernst-Planck equation using electrochemical module in COMSOL.

The grass structure which was observed during the microfluidic etch process could be eliminated by introducing a sacrificial etch-stop layer. An etch-stop layer was employed in previous LRSPP waveguide biosensors to prevent the O_2 plasma from etching into the lower cladding [105]. In such a device, a bilayer lift-off process followed by SiO_2 evaporation and lift-off was used to form the etch stop layer. The etch stop layer protects the waveguide from being in direct contact with the upper cladding Cytop and could be removed post channel etching. In the case of Bloch LRSPP waveguides, SiO_2 can't be used as the etch stop since the multilayer stack is composed of alternating layers of SiO_2 and Ta_2O_5. The etch stop layer could be replaced with, *e.g.*, a polymeric layer in this case.

To further improve the probing condition of electrochemical sensors, the contact pads that are evaporated through the shadow mask, can be connected to a carrier as shown in the figure below.

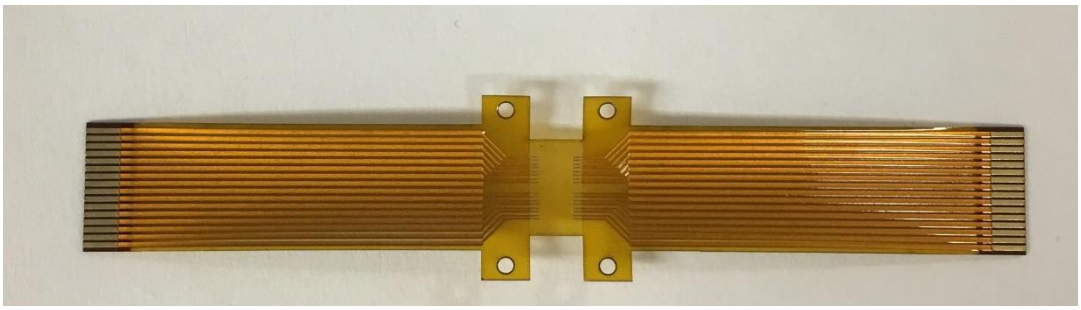

Bibliography

[1] R. M. Lequin, "Enzyme immunoassay (EIA)/enzyme-linked immunosorbent assay (ELISA)," Clinical Chemistry, **51** (12), 2415-2418, (2005).

[2] T. Chard, "Introduction to radioimmunoassay and related techniques, 4th Edition (Laboratory techniques in biochemistry and molecular biology), Elsevier Science (1990).

[3] T. Endo, "Fluorescence based assay with enzyme amplification on a microflow immunosensor chip for monitoring for monitoring coplanar polychlorinated biphenyls", Analytica Chimica Acta, **531** (1), 7-13 (2005).

[4] M. A. Cooper, "Optical biosensors in drug discovery," Nature reviews Drug discovery **1** (7), 515 (2002).

[5] N. Miura, H. Higobashi, G. Sakai, A. Takeyasu, T. Uda, N. Yamazoe, "Piezoelectric crystal immunosensor for sensitive detection of methamphetamine (stimulant drug) in human urine," Sensors and Actuators B **13** (1-3), 188–191 (1993).

[6] B. Zhang, Q. Mao, X. Zhang, T. Jiang, M. Chen, F. Yu, W. Fu, "A novel piezoelectric quartz micro-array immunosensor based on self-assembled monolayer for determination of human chorionic gonadotropin," Biosensors and Bioelectronics, **19** (7), 711–720 (2004).

[7] D. Tang, R. Yuan, Y. Chai, Y. Liu, J. Dai, X. Zhong, "Novel potentiometric immunosensor for determination of diphtheria antigen based on compound nanoparticles and bilayer two-dimensional sol–gel as matrices," Analytical and Bioanalytical Chemistry, **381** (3), 674–680 (2005).

[8] F. Darain, S.U. Park, Y.B. Shim, "Disposable amperometric immunosensor system for rabbit IgG using a conducting polymer modified screen-printed electrode," Biosensors and Bioelectronics, **18** (5), 773–780 (2003).

[9] S. Kumbhat, K. Sharma, R. Gehlot, A. Solanki, V. Joshi, J. Pharm, "Surface plasmon resonance based immunosensor for serological diagnosis of dengue virus infection," Journal of Pharmaceutical and Biomedical Analysis, **52**(2), 255−259 (2010).

[10] J. Homola, "Surface plasmon resonance sensors for detection of chemical and biological species," Chemical Reviews, **108** (2), 462-493 (2008).

[11] N. V. Zaytseva, R. A. Montagna, E. M. Lee, A. J. Baeumner, "Multi-analyte single-membrane biosensor for the serotype-specific detection of Dengue virus," Analytical and Bioanalytical Chemistry **380** (1), 46−53 (2004).

[12] N. V. Zaytseva, R. A. Montagna, A. J. Baeumner, "Microfluidic biosensor for the serotype-specific detection of dengue virus RNA," Analytical Chemistry **77** (23), 7520−7527 (2005).

[13] J. Wang, "Towards genoelectronics: electrochemical biosensing of DNA hybridization," Chemistry-A European Journal, **5** (6), 1681–1685 (1999).

[14] W. H. King, Jr, “Piezoelectric sorption detector”, Analytical Chemistry, **36** (9), 1735-1739 (1964).
[15] C. Yao, et al., “Aptamer-based piezoelectric quartz crystal microbalance biosensor array for the quantification of Ig-E.” Biosensors and Bioelectronics **24** (8), 2499-2503 (2009).
[16] N. J. De Mol, M. J. E. Fischer. "Surface plasmon resonance: methods and protocols," Springer (2010).
[17] NanoOptics [Online]: https://www.photonics.ethz.ch/fileadmin/user_upload/Courses/NanoOptics/
[18] P. Berini, “Plasmon polariton waves guided by thin lossy metal films of finite width: Bound modes of symmetric structures.” Physical Review B, **61** (15), 10484-10503 (2000).
[19] P. B. Johnson, R. W. Christy, “Optical constant of the noble metals,” Physical Review B, **6** 4370-4379 (1972)
[20] A. Otto, “Excitation of nonradiative surface plasma waves in silver by the method of frustrated total reflection,” Z. Phys. **216**, 398–410 (1968).
[21] A. Otto, “Excitation by light of + and − surface plasma waves in thin metal layers,” Z. Phys. **219**, 227–233 (1969)
[22] E. Kretschmann, “The determination of the optical constants of metals by excitation of surface plasmons,” Z. Phys. **241**, 313–324 (1971).
[23] W. Lee, D. B. Lee, B. K. Oh, W. H. Lee, and J. W. Choi, “Nanoscale fabrication of protein A on self-assembled monolayer and its application to surface plasmon resonance immunosensor,” Enzyme and Microbial Technology, **35**(6) 678–682 (2004).
[24] J. Homola, *et al*., “Spectral surface plasmon resonance biosensor for detection of staphylococcal enterotoxin B in milk” International Journal of Food Microbiology, **75** (1) 61-69 (2002).
[25] J. Wei, Y. Mu, D. Song, X. Fang, X. Liu, L. Bu, H. Zhang, G. Zhang, J. Ding, W. Wang, Q. Jin, G. Luo, “A novel sandwich immunosensing method for measuring cardiac troponin I in sera,” Analytical Biochemistry, **321** (2) 209-216 (2003).
[26] Q. Yu, S. Chen, A. D. Taylor, J. Homola, B. Hock, S. Jiang, “Detection of low molecular weight domoic acid using surface plasmon sensor,” Sensors and Actuators B **107** (1) 93–201 (2005).
[27] K. V. Gobi, C. Kataoka, N. Miura, “Surface plasmon resonance detection of endocrine disruptors using immunoprobes based on self-assembled monolayers” Sensors and Actuators B **108** (1) 784–790 (2005).
[28] J. Treviño, *et al*., “Surface plasmon resonance immunoassay analysis of pituitary hormones in urine and serum samples,” Clinica Chimica Acta **403** (1) 56-62 (2009).
[29] H. E. Indyk, B. D. Gill, D. C. Woollard, “An optical biosensor based immunoassay for the detection of bovine serum albumin in milk and milk products,” International Dairy Journal **47** 72-78 (2015).

[30] E. Mauriz, *et al*., "Multi-analyte SPR immunoassay for environmental sensing of pesticides," Analytical Bioanalytical Chemistry **387** (4) 1449-1458 (2007).
[31] G. Sakai, *et al*., "Highly selective and sensitive SPR immunosensor for detection of methamphetamine," Electrochimica Acta **44** (21-22) 3849-3854 (1999).
[32] M. Pan, K. L. Lee, L. Wang, P. K. Wei, "Chip based digital surface plasmon resonance sensing platform for ultra sensitive biomolecular detection," Biosensors Bioelectronics **91** 580-587 (2017).
[33] D. J. O'Shannessy, M. Brigham-Burke, K. Soneston, P. Hensley, I. Brooks, "Determination of Rate and Equilibrium Binding Constants for Macromolecular Interactions Using Surface Plasmon Resonance: Use of Nonlinear Least Squares Analysis Methods," Analytical Biochemistry **212**, 457-468 (1993).
[34] R. Karlsson, A. Michaelsson, L. Mattsson, J. Immunol. "Kinetic analysis of monoclonal antibody-antigen interactions with a new biosensor based analytical system," Methods **145**, 229-240 (1991).
[35] C.R. Lavers, J.S. Wilkinson, "A waveguide coupled surface plasmon sensor for an aqueous environment," Sensors and Actuators B: Chemical **22** (1), 75-81 (1994).
[36] R. C. Jorgenson and S. S. Yee, "A fiber optic chemical sensor based on surface plasmon resonance", Sensors and Actuators B: Chemical, **12** (3) 213-220 (1993).
[37] C. Moweta et al. "Determination of simazine in water samples by waveguide surface plasmon resonance", Analytica Chimica Acta, **238** (1-2), 109-117, (1996).
[38] R. Slavík, *et al*., "Novel spectral fiber optic sensor based on surface plasmon resonance." Sensors and Actuators B: Chemical **74** (1-3) 106-111 (2001).
[39] J. Homola, I. Kudela, S. S. Yee, "Surface plasmon resonance sensors based on diffraction gratings and prism couplers: sensitivity comparison," Sensors and Actuators B **54**, 16-24 (1999).
[40] D. C. Cullen, R. G. W. Brown, C. R. Lowe, "Detection of immunocomplex formation via surface plasmon resonance on gold coated diffraction gratings" Biosensors **3**, 211-255 (1987).
[41] M. J. Jory, P. S .Vukusic, J. R. Sambles, "Development of a prototype gas sensor using surface plasmon resonance on grating," Sensors and Actuators B **17** (3) 203-209 (1994).
[42] J. Dostálek, A. Kasry, W. Knoll, "Long range surface plasmons for observation of biomolecular binding events at metallic surfaces", Plasmonics **2** (3) 97-106, (2007)
[43] A. Degiron, et al, "Directional coupling between dielectric and long range plasmon waveguides," New Journal of Physics **11** (1), 0015002 (2009).
[44] P. Berini, "Long-range surface plasmon polaritons," Advances in Optics and Photonics, **1** (3), 484−588 (2009).
[45] M. Vala, S. Etheridge, J. Roach and J. Homola, Sens. Act. B 139 (1) (2009) 59–63.
[46] V. Chabot, Y. Miron, M. Grandbois and P. G. Charette, Sensors and Actuators B **174** 94-101 (2012).

[47] R. Charbonneau, N. Lahoud, G. Mattiussi, P. Berini "Characterization of long-range surface-plasmon-polariton waveguides," Journal of Applied Physics. **98** (4) 043109 (2005)

[48] C. Chiu, E. Lisicka-Skrzek, R. N. Tait and P. Berini, "Fabrication of surface plasmon waveguides and devices in Cytop with integrated microfluidic channels," Journal of Vacume Science and Technology B, **28** (4), 729–735 (2010).

[49] O. Krupin, *et al.*, "Biosensing using LRSPP waveguides", Proceedings of SPIE, vol 10242.

[50] W. R. Wong, S. D. Sekaran, F. R. M. Adikan, P. Berini, "Detection of dengue NS1 antigen using long range surface plasmon waveguide," Biosensors Bioelectronics **78** 132-139 (2016).

[51] W. R. Wong, O. Krupin, S. D. Sekaran, F. R. M. Adikan, P. Berini, "Serological diagnosis of dengue infection in blood plasma using long range surface plasmon waveguides," Analytical Chemistry **86** (3) 1735–1743 (2014).

[52] P. Béland, O. Krupin and P. Berini, "Selective detection of bacteria in urine with a long range surface plasmon waveguide biosensor," Biomedical Optics Express **6** (8), 2908–2922 (2015).

[53] O. Krupin, P. Berini, "Detection of leukemia markers using long range surface plasmon waveguides functionalized with protein G," Lab on a Chip **15** (21) 4156–4165 (2015).

[54] M. Khodami, P. Berini, "Biomolecular kinetics analysis using long range surface plasmon waveguides" Sensors and Actuators B 243 (2017) 114-120.

[55] M. Khodami, P. Berini, "Low detection limits using sandwich and inhibition assays on long range surface plasmon waveguide biosensors," Sensors and Actuators B **273**, 1156-1161 (2018).

[56] W. R. Wong, H. Fan, F. R. M. Adikan, P. Berini, "Multichannel Long-range Surface Plasmon Waveguides for Parallel Biosensing," Journal of Light Wave Technology **36**, 5536-5546 (2018).

[57] S. Hassan, M. Khodami, R. N. Tait, P. Berini, "Fabrication of surface plasmon-polariton Bragg gratings with microfluidic channels in CYTOP cladding," Microelectronics engineering, **135,** 38-44 (2015).

[58] M. Khodami, P.Berini, "Characterization of long range surface plasmon Bragg gratings with microfluidic channels" Photonics North (2015)

[59] Fan, Hui, Robert Charbonneau, and Pierre Berini. "Long-range surface plasmon triple-output Mach-Zehnder interferometers," Optics Express **22** (4) 4006-4020 (2014).

[60] O. Krupin, H. Asiri, C. Wang, R. N. Tait, P. Berini, "Biosensing using straight long range surface plasmon waveguide", Optics Express **21** (1), 698-709 (2013)

[61] N. R. Fong *et. al.*; "Bloch long range surface plasmon polaritons on metal stripe waveguides on a multilayer substrate," ACS Photonics **4**, 593-599 (2017)

[62] Z. Hirbodvash *et. al.*, "Grating couplers fabricated by e-beam lithography for long range surface plasmon waveguides embedded in a fluoropolymer," Applied Optics **58** (11), 2994-3002 (2019).

[63] M. Khodami, P. Berini, "Grating couplers for Bloch long range surface plasmon on metal stripe waveguides," Journal of Optical Society of America B **26** (7) 1921-1930 (2019).

[64] M. Khodami, Z. Hirbodvash, O. Krupin, P. Berini, "Bloch long range surface plasmons on waveguides arrays as multichannel biosensors" Plasmonics in Biology and Medicine XVII 11257 (2020).

[65] M. Khodami, et al., "Fabrication of multichannel Bloch long range surface plasmon biosensors" Integrated Optics: Devices, Materials, and Technologies XXIV 11283, (2020).

[66] V. N. Konopsky, E. V. Alieva, "Long-Range Propagation of Plasmon Polaritons in a Thin Metal Film on a One-Dimensional photonic crystal surface," Physical Review Letters **97**, 253904-253907 (2006).

[67] E. V. Alieva, V. N. Konopsky, "Photonic crystal surface waves for optical biosensors," Analytical Chemistry **79**, 4729−4735 (2007).

[68] A. Delfan, I. Degli-Eredi, J. E. Sipe, "Long-range surface plasmons in multilayer structures," Journal of Optical Society of America B **32**, 1615−1623 (2015).

[69] P. Adam, et al., "Surface plasmons for biodetection" Photonic sensing: Principles and applications for safety and security monitoring, 1-58, John Wiley & Sons (2012).

[70] J. E. Butler *et al.*, "The physical and functional behavior of capture antibodies adsorbed on polystyrene," Journal of Immunological Methods **150** (1-2) 77-90 (1992).

[71] R. E. Holmlin, X. Chen, R. G. Chapman, S. Takayama, G. M. Whitesides "Zwitterionic SAMs that resist nonspecific adsorption of protein from aqueous buffer," Langmuir, ***17*** (9), 2841-2850 (2001).

[72] P. Fenter, *et al*., "Structure of octadecyl thiol self-assembled on the silver (111) surface: an incommensurate monolayer," Langmuir **7** (10) 2013-2016 (1991)

[73] R. G. Nuzzo, D. L. Allara, "Adsorption of bifunctional organic disulfides on gold surfaces," Journal of the American Chemical Society **105** (13) 4481-4483 (1983).

[74] M. D. Porter, *et al*. "Spontaneously organized molecular assemblies. 4. Structural characterization of n-alkyl thiol monolayers on gold by optical ellipsometry, infrared spectroscopy, and electrochemistry." Journal of the American Chemical Society **109** (12) 3559-3568 (1987).

[75] C. D. Bain, *et al.,* "Formation of monolayer films by the spontaneous assembly of organic thiols from solution onto gold," Journal of the American Chemical Society **111**(1) 321-335 (1989).

[76] M. Milan, and G. M. Whitesides, "Patterning self-assembled monolayers using microcontact printing: a new technology for biosensors." Trends in biotechnology **13** (6) 228-235 (1995).

[77] G. M. Whitesides, *et al.*, "Controlling cell attachments on contoured surfaces with self-assembled monolayer of alkanethiolates on gold," proceedings of the national academy of science, **93** (20), 10775-10778 (1996).
[78] L. H. Dubois, G. N. Ralph, "Synthesis, structure, and properties of model organic surfaces." Annual review of physical chemistry **43** (1) 437-463 (1992).
[79] G. M. Whitesides, *et al.*, "Noncovalent synthesis: using physical-organic chemistry to make aggregates" Accounts of Chemical Research **28** (1) 37-44 (1995).
[80] K. Motesharei, D. C. Myles. "Molecular recognition on functionalized self-assembled monolayers of alkanethiols on gold," Journal of the American Chemical Society **120** (29) 7328-7336 (1998).
[81] Love, J. Christopher, *et al.*, "Self-assembled monolayers of thiolates on metals as a form of nanotechnology." Chemical reviews **105** (4) 1103-1170 (2005).
[82] G. T. Hermanson, "Bioconjugate techniques, Chapter 4," Academic Press (2013).
[83] Y. M. Bae, B.-K. Oh, W. Lee, W. H. Lee, and J.-W. Choi, "Study on orientation of immunoglobulin G on protein G layer," Biosensors and Bioelectronics, **21**, 103–110 (2005).
[84] S. A. Campbell, "Fabrication engineering at the micro and nanoscale," Oxford university press (2008).
[85] Asahi Glass Company. Cytop Technical Brochure [Online]; http://www.agc.com
[86] Chemours company, Teflon technical brochure [Online], www.chemours.com
[87] M. Khodami, H. Northfield, E. Lisicka-Skrzek, R. N. Tiat, P. Berini, "Reactive ion etching of Cytop and investigation of residual microstructure," IEEE Journal of Microelectromechanical Systems, **29** (2), 228-235 (2020).
[88] C. Mack, "Fundamental principles of optical lithography: The science of microfabrication," John Wiley & Sons (2008).
[89] A. Durandet *et al.* "Silica buried channel waveguides fabricated at low temperature using PECVD". Electronics Letters, **32**(4) 326-327 (1996).
[90] R. G. Hunsperger, "Integrated optics*: Theory and technology*," Springer (1984).
[91] C. Vieu, *et al*, "Electron beam lithography: resolution limits and applications," Applied surface science, **164** 111-117 (2000).
[92] T. H. P. Chang, "Proximity effect in electron beam lithography", Journal of Vacuum Science and Technology **12**, 1271-1275 (1975).
[93] Micro and Nanostructuring [Online]: https://mpl.mpg.de/research-at-mpl/technology-development-service-units/tdsu-1-micro-nanostructuring/
[94] Park, J. S., *et al.* "Dry etching of ZnO films and plasma-induced damage to optical properties," Journal of Vacuum Science & Technology B: Microelectronics and Nanometer Structures Processing, Measurement, and Phenomena **21** (2) 800-803 (2003).
[95] P. Mao, J. Han, "Fabrication and characterization of 20 nm planar nanofluidic channels by glass–glass and glass–silicon bonding" Lab on a Chip **5** (8), 837-844 (2005).

[96] H. Takagi, K. Kikuchi, R. Maeda, “Surface activated bonding of silicon wafers at room temperature,” Applied Physics Letters **68**, 2222-2224 (1996)

[97] T. Suni, K. Henttinen, I. Sunni, J. Makinen, “Effects of plasma activation on hydrophilic bonding of Si and SiO_2”, Journal of electrochemical society **109** 348-351 (2002).

[98] M. M. R. Howlader, T. Soga, H. Itoh, M. J. Kim, “Sequential plasma activated process for silicon direct bonding”, ECS transactions **3** 191-201 (2006).

[99] A. Berthold, L. Nicola, P. M. Sarro, M. J. Vellekoop, “Glass to glass anodic bonding with standard IC technology thin films as intermediate layers,” Sensors and Actuators A **82** (1-3) 224-228 (2000).

[100] K. W. Oh, A. Han, S. Bhansali, C. H. Ahn, “A low temperature bonding technique using spin on fluorocarbon polymers to assemble microsystems,” Journal of Micromechanics and Microengineering **12** 187-192 (2002).

[101] V. Patil, C. B. O’Neal, “Adhesive strength characterization of Cytop: Low temperature wafer level packaging,” Proceedings of IMEC (2006).

[102] C. Tsao, D. L. Devoe, “Bonding of thermoplastic polymer microfluidics,” Microfluid Nanofluid **6** 1-16 (2009).

[103] A. Giamberardino, *et. al.*, “Ultrasensitive norovirus detection using DNA aptasensor technology,” PloS one **8** (11) (2013).

[104] J. Homola, I. Koudela, S. S. Yee “Surface plasmon resonance based on diffraction gratings and prism coupler: sensitivity comparison,” Sensors and Actuators B **54**, 16-24 (1999).

[105] P. Ren, O. Krupin, P. Berini, R. N. Tait, “Fabrication of long range surface plasmon waveguide biosensors in a low-index fluoropolymer,” Journal of Vacuum Science Technology B, **36** (4) 042601 (2018).